Chem Soc Rev

Chemical Society Reviews

www.rsc.org/chemsocrev

Volume 42 | Number 1 | 7 January 2013 | Pages 1–412

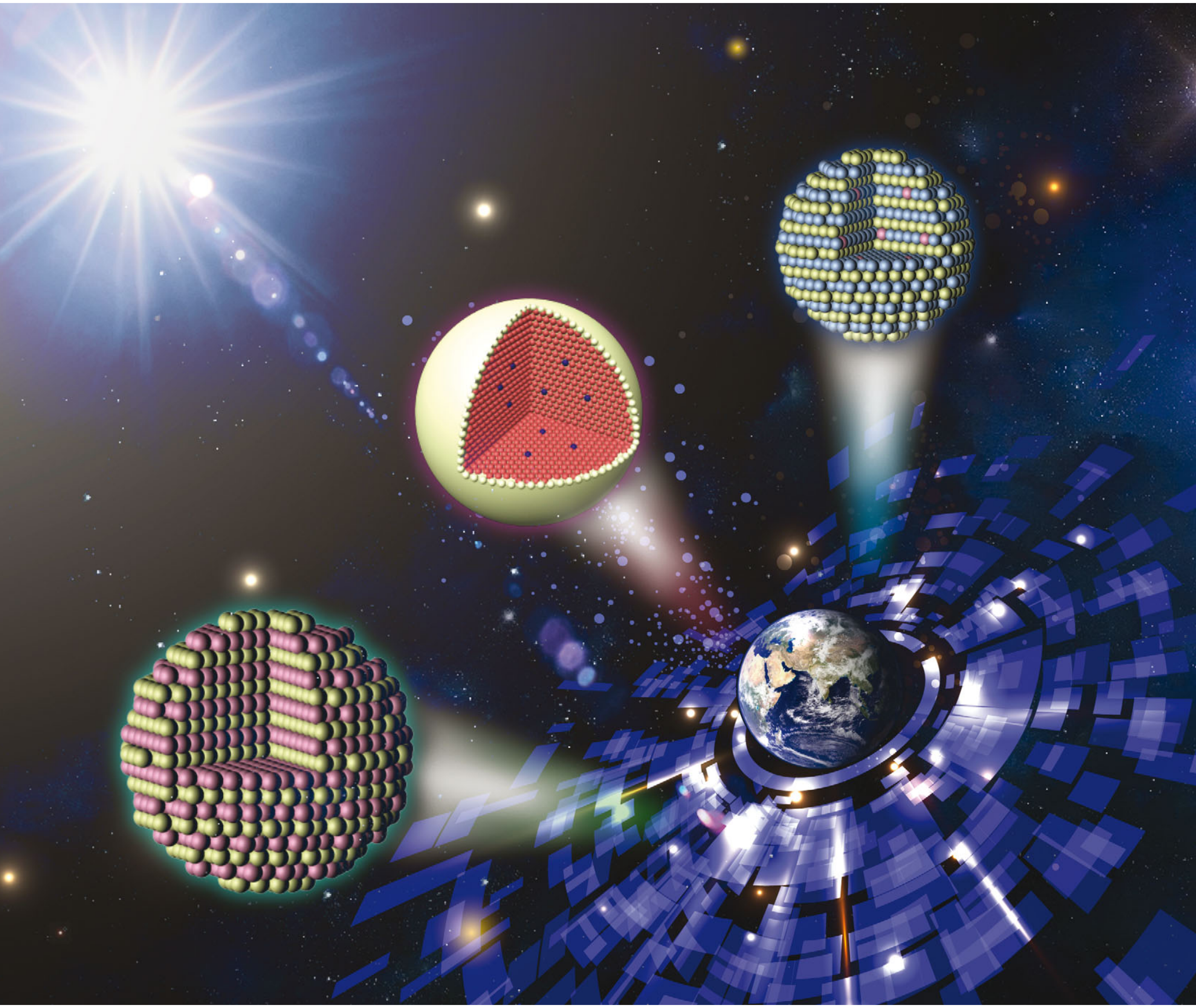

ISSN 0306-0012

RSC Publishing

**REVIEW ARTICLE**

Xiaoyong Huang, Sanyang Han, Wei Huang and Xiaogang Liu

Enhancing solar cell efficiency: the search for luminescent materials as spectral converters

Chem Soc Rev

RSC Publishing

REVIEW ARTICLE

View Article Online
View Journal | View Issue

Published on 16 October 2012. Downloaded on 11/09/2014 14:42:06.

**Cite this:** *Chem. Soc. Rev.*, 2013, **42**, 173

Received 27th July 2012

DOI: 10.1039/c2cs35288e

**www.rsc.org/csr**

# Enhancing solar cell efficiency: the search for luminescent materials as spectral converters

Xiaoyong Huang,[a] Sanyang Han,[a] Wei Huang*[bc] and Xiaogang Liu*[ad]

Photovoltaic (PV) technologies for solar energy conversion represent promising routes to green and renewable energy generation. Despite relevant PV technologies being available for more than half a century, the production of solar energy remains costly, largely owing to low power conversion efficiencies of solar cells. The main difficulty in improving the efficiency of PV energy conversion lies in the spectral mismatch between the energy distribution of photons in the incident solar spectrum and the bandgap of a semiconductor material. In recent years, luminescent materials, which are capable of converting a broad spectrum of light into photons of a particular wavelength, have been synthesized and used to minimize the losses in the solar-cell-based energy conversion process. In this review, we will survey recent progress in the development of spectral converters, with a particular emphasis on lanthanide-based upconversion, quantum-cutting and down-shifting materials, for PV applications. In addition, we will also present technical challenges that arise in developing cost-effective high-performance solar cells based on these luminescent materials.

## 1. Introduction

Sunlight is a free and, in many parts of the world, abundant source of energy that can be captured by new technologies and transformed into electricity.[1,2] It has been reported that sunlight that reaches the Earth's surface delivers 10 000 times more energy than what we consume.[3] As a result, the use of solar energy is expected to have the potential to meet a large portion

---

[a] *Department of Chemistry, Faculty of Science, National University of Singapore, 3 Science Drive 3, 117543, Singapore. E-mail: chmlx@nus.edu.sg*

[b] *Singapore-Jiangsu Joint Research Center for Organic/Bio-electronics and Information Displays and Institute of Advanced Materials, Nanjing University of Technology, Nanjing 211816, China. E-mail: wei-huang@njut.edu.cn*

[c] *Key Laboratory for Organic Electronics and Information Displays and Institute of Advanced Materials, Nanjing University of Posts and Telecommunications, Nanjing 210046, China. E-mail: iamwhuang@njupt.edu.cn*

[d] *Institute of Materials Research and Engineering, Agency for Science, Technology and Research, 3 Research Link, 117602, Singapore*

**Xiaoyong Huang**

*Xiaoyong Huang was born in Jiangxi, China. He obtained his BE degree from China University of Geosciences (Beijing) in 2004 and his MS degree from Institute of Geochemistry, Chinese Academy of Sciences in 2007. Subsequently, he completed his PhD (2011) in the field of lanthanide-ion-doped quantum cutting and upconversion phosphors for photovoltaic applications under the supervision of Prof. Qinyuan Zhang at South China University of Technology. He is currently working as a postdoctoral research fellow in the group of Prof. Xiaogang Liu at the National University of Singapore. His present research focuses on optical spectroscopy and application of luminescent nanomaterials.*

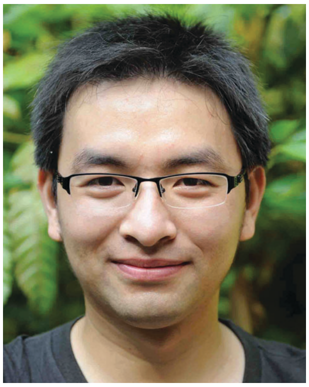

**Sanyang Han**

*Sanyang Han was born in Hubei, China. He received his BS (2007) and MS (2010) degrees in chemistry from Soochow University. He is currently pursuing a PhD degree under the supervision of Prof. Xiaogang Liu in the Department of Chemistry at the National University of Singapore. His research interest focuses on development of novel lanthanide-doped luminescent nanomaterials.*

Published on 16 October 2012. Downloaded on 11/09/2014 14:42:06.

of future energy consumption requirements. Despite significant development of the photovoltaic (PV) industry over the past decades, the efficient and cost-effective conversion of solar energy into electricity through PV cells remains a daunting task.[4–6] Current annual solar energy usage is well below 1% of total energy consumption, while fossil fuels account for over 90% of the energy consumption. Before the large-scale use of solar energy, more efficient PV systems at reduced costs must be developed.[7–20]

A major problem limiting the conversion efficiency of PV cells is their insensitivity to a full solar spectrum. The spectral distribution of sunlight at Air Mass 1.5 global (AM 1.5G) consists of photons with wide wavelengths ranging from ultraviolet to infrared (280–2500 nm, 0.5–4.4 eV), but current PV cells only utilize a relatively small fraction of the solar photons (Fig. 1).[21] This is attributed to the fact that each PV material responds to a narrow range of solar photons with energy matching the characteristic bandgap of the material. In principle, only photons with energy higher than the bandgap are absorbed, but the excess energy is not effectively used and released as heat. The thermalization of photon energies exceeding the bandgap and non-absorption of photons with energy less than the bandgap amount to the loss of approximately 50% of the incident solar energy in silicon-based solar cell conversion to electricity. Notably, the theoretical maximum level of efficiency for crystalline silicon (c-Si) with a bandgap energy ($E_g$) of 1.1 eV is approximately 31% or 41%, depending on the concentration ratio, as defined by the Shockley–Queisser limit.[22]

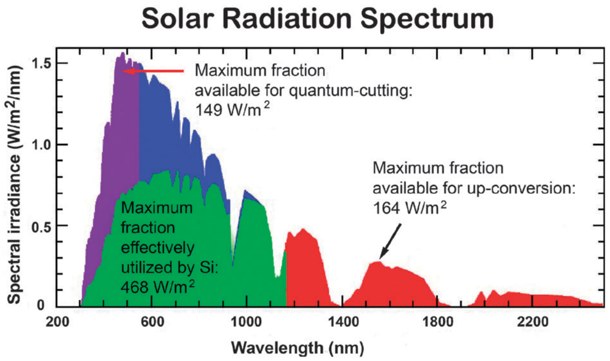

**Fig. 1** AM 1.5G spectrum showing the fraction (highlighted in green) absorbed by a typical silicon-based PV cell and the spectral regions that can be utilized through quantum-cutting and upconversion processes (highlighted in purple and red, respectively). (Adapted with permission from ref. 21. Copyright 2007, Elsevier B.V.)

The inherent thermalization and non-absorption losses can be minimized using luminescent materials as spectral converters. The approach, termed the third-generation solar photon conversion, involves the incorporation of a passive luminescent layer into PV cells.[23–28] An important aspect of using this technology is that spectral converters are readily applicable to existing solar cells with few changes as the spectral converters and solar cells can be optimized independently.

To increase the efficiency of single-junction solar cells, three luminescence processes including upconversion, quantum-cutting, and down-shifting are currently explored for developing efficient PV devices. Trivalent lanthanide ions are the prime candidates to achieve efficient spectral conversion because of

**Wei Huang**

*Wei Huang received his BSc, MSc, and PhD degrees in chemistry from Peking University in* 1983, 1988, *and* 1992, *respectively. In* 1993, *he began his postdoctoral research with the Chemistry Department at National University of Singapore, where he participated in the founding of the Institute of Materials Research and Engineering. In* 2001, *he became a chair professor at Fudan University, where he founded and chaired the Institute of Advanced Materials. In June* 2006, *he was appointed as the Deputy President of Nanjing University of Posts and Telecommunications, where he initiated the Institute of Advanced Materials and the Key Laboratory for Organic Electronics and Information Displays. In July* 2012, *he was appointed as the President of Nanjing University of Technology. He is an academician of the Chinese Academy of Sciences. His research interests include organic opto-electronics, nanomaterials, polymer chemistry, plastic electronics, and bioelectronics.*

**Xiaogang Liu**

*Xiaogang Liu was born in Jiangxi, China. He earned his BE degree* (1996) *in Chemical Engineering from Beijing Technology and Business University. He received his MS degree* (1999) *in chemistry from East Carolina University under the direction of Prof. John Sibert and completed his PhD* (2004) *at Northwestern University under the supervision of Prof. Chad Mirkin. He then became a postdoctoral fellow in the group of Prof. Francesco Stellacci at MIT. He joined the faculty of the National University of Singapore in* 2006. *He holds a joint appointment with the Institute of Materials Research and Engineering, Agency for Science, Technology and Research. His interests include lanthanide-doped optical nanomaterials, supramolecular chemistry, and surface science for catalysis, sensors and biomedical applications.*

This journal is © The Royal Society of Chemistry 2013

Published on 16 October 2012. Downloaded on 11/09/2014 14:42:06.

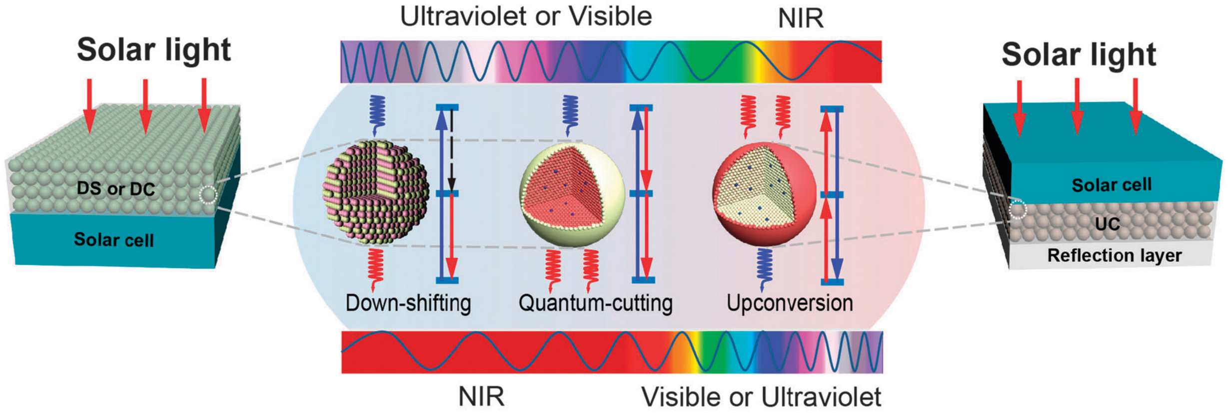

**Fig. 2** Spectral conversion design for PV applications involving down-shifting (DS), quantum-cutting (QC), and upconversion (UC) luminescent materials. In a typical down-shifting process, upon excitation with a high-energy photon, nonradiative relaxation takes place followed by radiative relaxation, thereby resulting in the emission of a lower-energy photon. In contrast, two-step radiative relaxation occurs in the quantum-cutting process upon excitation with a high-energy photon, leading to the emission of two (or more) lower-energy photons. The upconversion process can convert two (or more) incident low-energy photons into a single higher-energy photon. Both down-shifting and quantum-cutting processes are able to make effective use of the high-energy portion of the solar spectrum, but with dramatically different quantum efficiency. The theoretical quantum efficiency for down-shifting is always less than 100%, whereas it exceeds 100% for quantum-cutting. Note that the down-shifting and quantum-cutting materials are generally placed on the front surface of a monofacial solar cell, allowing the downconverted photons to be absorbed by the solar cell. The upconversion material is typically placed in between a bifacial solar cell and a light-reflection layer to harvest the sub-bandgap spectrum of sunlight.

their rich energy-level structure (known as the Dieke diagram) that allows for facile photon management.[29–31]

Upconversion of sub-bandgap light is exploited to reduce non-absorption energy losses. The limiting efficiency of a solar cell, equipped with an upconverter, has recently been discussed by Trupke *et al.*[32] using a detailed balance model. The system under investigation consists of a bifacial single-junction solar cell with an upconverting layer located at the rear of the solar panel (Fig. 2). The upconverter transforms two (or more) transmitted sub-bandgap photons into one usable above-bandgap photon, which is subsequently absorbed by the solar cell to generate electron–hole pairs. The maximum efficiency was calculated to be 47.6% for non-concentrated light.

Quantum-cutting through downconversion is able to split one incident high-energy photon into two (or more) lower-energy photons with a conversion efficiency higher than 100%.[33] This process could minimize the energy loss caused by thermalization of hot charge carriers after the absorption of high-energy photons, if the downconverted photons can be absorbed by solar cells. As a result, the photocurrent of the device can be doubled. A recent quantum-cutting model proposed by Trupke *et al.*[34] showed that a solar cell ($E_g$ = 1.1 eV), modified with a downconverting layer on the front surface, can achieve a conversion efficiency of up to 38.6% (Fig. 2).

Down-shifting is a single photon process that involves transformation of one absorbed high-energy photon into one lower-energy photon. This process obeys the Stokes Law with wavelength change known as the Stokes shift. Down-shifting is similar to quantum-cutting, but its conversion efficiency does not exceed 100%. Despite this disadvantage, down-shifting can still be useful for improving PV efficiency by shifting short-wavelength sunlight (usually ultraviolet and blue) to the longer-wavelength region where the spectral response of the solar cell is more sensitive (Fig. 2). Until now, two main classes of down-shifting-based PV devices have been investigated: a luminescent solar concentrator and a planar down-shifting layer. Lanthanide-doped phosphors and glasses, semiconductor quantum dots (QDs) and organolanthanide complexes have been thoroughly explored as potential wavelength-shifting materials.

This review focuses on the importance, development, and implementation of lanthanide-doped luminescent materials for modern PV applications. We begin by describing fundamental aspects central to rational design of solar cells followed by discussing the operating principles of lanthanide-doped upconversion materials as spectral converters to reduce the transmission loss of sub-bandgap light. Furthermore, an overview of the state-of-art near-infrared (NIR) quantum-cutting using a single $Ho^{3+}$ ion and $Ln^{3+}$–$Yb^{3+}$ (Ln = Tb, Tm, Pr, Er, Nd, Ho, and Dy) pairs for c-Si solar cells is presented. The underlying energy transfer (ET) mechanisms are then discussed. The attempts to sensitize $Ln^{3+}$–$Yb^{3+}$ couples using ion species ($Ce^{3+}$, $Eu^{2+}$, $Yb^{2+}$, and $Bi^{3+}$) in different host lattices are subsequently described. We also highlight the topic of multiple exciton generation (MEG) in QDs to reflect an important parallel development promising for solar energy conversion. Finally, we discuss the advances toward realizing spectral conversion by utilizing planar down-shifting layers composed of phosphors, QDs and organolanthanide complexes as fluorophores. Selected examples of recent experimental results will be presented.

## 2. Fundamental aspects of solar cell design

### 2.1 Solar cells

Solar cells are typically composed of special light-absorbing semiconducting materials.[35] When sunlight falls on a solar cell, the photons activate the electrons in the cell and promote them into a higher energy conduction band. Those electrons can then be harnessed to create electric current. To produce a solar

Published on 16 October 2012. Downloaded on 11/09/2014 14:42:06.

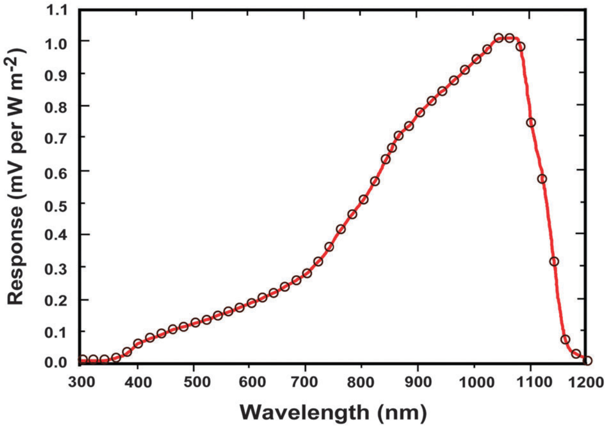

**Fig. 3** Normalized spectral response of a typical c-Si solar cell pyranometer (courtesy of Apogee Instruments, Inc., 2008). The c-Si is an indirect bandgap semiconductor so there is not a sharp cut off at the wavelength corresponding to the bandgap ($E_g$ = 1.12 eV).

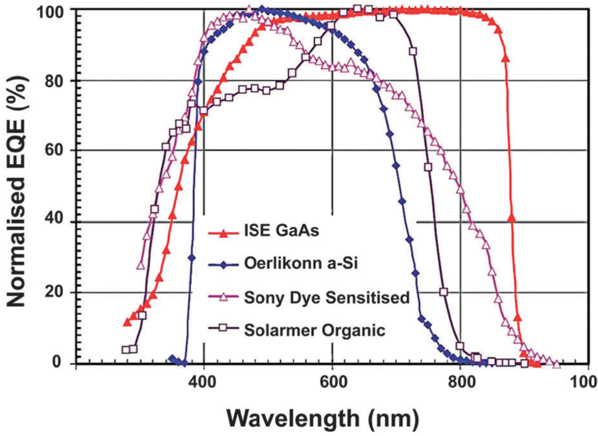

**Fig. 4** Normalized external quantum efficiency (EQE) spectra for several wide bandgap PV cells. (Reprinted with permission from ref. 38. Copyright 2010, John Wiley & Sons, Ltd.)

cell, the semiconductor is doped with either positive charge carriers (p-type) or negative charge carriers (n-type). If two differently doped semiconductor layers are combined, then a so-called p–n junction results on the boundary of the layers. The conversion efficiency of solar energy is perhaps the most significant parameter that determines the performance of a PV device. For any traditional single p–n junction solar cell, the bandgap energy of the semiconductor from which the solar cell is fabricated places a fundamental upper limit on its conversion efficiency. Currently, solar cells based on crystalline, polycrystalline and amorphous silicon represent more than 90% of the world production.[36] The use of c-Si enables PV devices to achieve a maximum conversion efficiency of 25%.[37]

The c-Si solar cells work most efficiently in the 950–1100 nm spectral region, but they show very low spectral response to the short-wavelength sunlight (Fig. 3). Therefore, ideal quantum-cutting and down-shifting luminescent materials for c-Si solar cells should convert the high-energy (usually ultraviolet–blue) light into the NIR emission around 1000 nm, while the most desirable upconverters for c-Si solar cells are able to absorb light above 1100 nm and convert it into emission around 1000 nm. In principle, an upconverter for c-Si solar cells should satisfy the following requirements: (i) the excitation range longer than 1100 nm ($E < 1.12$ eV); (ii) the emission range shorter than 1100 nm; (iii) good response under low-intensity excitation (in the range of 10–100 W m$^{-2}$); and (iv) high conversion efficiency and high transparency toward the upconverted light. Compared to conventional c-Si solar cells, wide bandgap solar cells would benefit much more from incorporation of an upconverting layer due to the dominant transmission losses. The wide bandgap solar cells, including GaAs, amorphous Si, dye-sensitized and organic solar cells, can work well in the visible region, but their absorption is generally limited to a maximum wavelength of ~900 nm (Fig. 4).[38] For example, in an ideal single-junction solar cell with a bandgap of 1.7 eV, approximately 49% of the incoming solar energy is lost because it cannot be absorbed by the solar cell. An ideal upconverter for PV applications would convert incident sub-bandgap sunlight into monochromatic above-bandgap light where solar cells have their optimum spectral response.

## 2.2 Luminescence

Luminescence generally refers to the emission of light by a material after it has absorbed energy.[39] The term 'luminescence' was introduced in 1888 by Wiedemann.[40] Luminescence can be generated from different types of energetic sources, including electromagnetic radiations, electric fields, X-rays, and charged particles from radioactive decay. Depending upon the nature of the excitation source, luminescence can be subdivided into several categories that are generally indicated by a prefix. In the case of photo-excitation, this luminescence is called photoluminescence. In this review, we will focus on photoluminescence-based spectral conversion approaches for PV applications. Fluorescence and phosphorescence are two major forms of photoluminescence extensively investigated in modern research. They are distinguishable from the decay time ($\tau$). Fluorescence has a short time lapse ($\tau < 10$ ms) after the excitation source is removed, while phosphorescence has a much longer decay time ($\tau > 0.1$ s).[40] Inorganic solids that give rise to luminescence are called phosphors or, lately, luminescent materials.[41,42] Luminescent materials generally require a host crystalline structure that constitutes the bulk of the phosphors. The characteristic luminescence properties are obtained by doping the host material with relatively small amounts of foreign ions. The luminescence of inorganic solids can be roughly classified into two mechanisms: luminescence of localized centers or activators (Fig. 5a and b) and luminescence of semiconductors through band-to-band excitation (Fig. 5c). To induce luminescence from an activator without efficient absorption for the available excitation energy, a sensitizer ion is often incorporated into the host material to transfer its excitation energy to the activator. The emission color can be readily adjusted by varying the dopant concentration or composition without changing the host lattice. Notably, a number of lanthanide

Published on 16 October 2012. Downloaded on 11/09/2014 14:42:06.

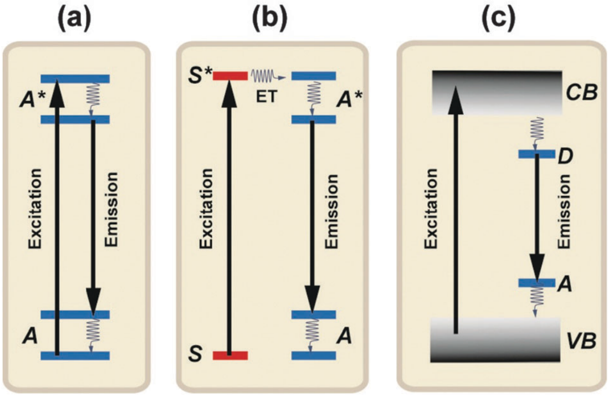

**Fig. 5** Luminescence in inorganic solids. (a) Emission from a luminescence activator upon excitation. (b) Sensitized emission from an activator through energy transfer from a sensitizer to the activator upon excitation of the sensitizer. (c) Emission from a semiconductor after band-to-band excitation. A and A* represent the ground and excited states of the activator, respectively. S and S* represent the ground and excited states of the sensitizer, respectively. VB and CB represent the valence and conduction bands of the semiconductor, while D and A represent the donor and acceptor energy levels, respectively.

activators show emission spectra with spectral positions that are hardly influenced by their chemical environment.

The conversion efficiency of a phosphor, usually expressed as either a quantum efficiency or an energy efficiency, is an important consideration in practical applications. The quantum efficiency (or quantum yield) is defined as the fraction of the input photons contributing to the desired optical process.[43,44] In contrast, the energy efficiency is the ratio of the output power to the input power. In a luminescence process, the excited state decays by a combination of radiative and nonradiative processes, and the relative rate of these processes determines the quantum efficiency. Radiative decay describes molecular deexcitation processes accompanied by photon emission. Molecules in the excited states can also relax by nonradiative processes where excitation energy is not converted into photons but is dissipated by thermal processes such as vibrational relaxation and collisional quenching. Let $k_r$ and $k_{nr}$ be the radiative and nonradiative decay rates, respectively, and $N$ be the population density of luminescence activators in the excited state. The temporal evolution of the excited state can be described by:

$$\frac{\mathrm{d}N}{\mathrm{d}t} = -(k_r + k_{nr})N \tag{1}$$

The luminescence therefore decays exponentially with a time constant $\tau$ where

$$\tau = \frac{1}{k_r + k_{nr}} \tag{2}$$

Note that the observed luminescence lifetime, $\tau$, measures the combined rate of the radiative and nonradiative pathways. The fraction of the excitation contributing to radiative decay processes is $k_r/(k_r + k_{nr})$. Thus the quantum efficiency ($\eta_{PL}$) can be calculated using the following formula,[45]

$$\eta_{PL} = \frac{k_r}{k_r + k_{nr}} = \frac{\tau}{\tau_R} \tag{3}$$

Here, $\tau_R = 1/k_r$ is the radiative lifetime, namely, the lifetime of the excited state in the absence of nonradiative decay processes. The observed lifetime, $\tau$, can be calculated from intensity decay curves. However, the radiative lifetime, $\tau_R$, is usually estimated by the use of Judd–Ofelt theory as it is not easily experimentally determined.[46]

## 2.3 Lanthanide ions

The lanthanide elements, characterized by the progressive filling of the 4f orbitals, are a family of 15 chemically similar elements from lanthanum (La) to lutetium (Lu). The term 'rare earth' is applied to lanthanide elements and also to yttrium (Y), which is found in nature always along with the lanthanides. The lanthanides, essentially existing in their most stable oxidation state as trivalent ions ($Ln^{3+}$), are extensively investigated for their optical properties.[47–55] The lanthanide ions feature an electron configuration of $4f^n$ ($0 < n < 14$) and the arrangements of electrons within this configuration are substantially diverse. This results in a fairly large number of energy levels.[56] Most of the fascinating optical properties, such as photon upconversion emission, of lanthanide ions can be ascribed to the electron transitions within the $4f^n$ configuration (Table 1). Most lanthanide ions generally show sharp line spectra, much narrower and more distinct than those for transition metal ions. The spectra are associated with weak f–f electronic transitions. The narrow spectral bands indicate that the f-orbitals have a smaller radial extension than the outer 5s and 5p orbitals, thus leading to smaller electron–phonon coupling strengths and a lower susceptibility to crystal-field and exchange perturbations.

When a 4f electron is excited into a 5d orbital that extends beyond the 5s and 5p orbitals, the spectroscopic properties of lanthanide ions in the $4f^n5d$ electronic configuration are influenced more strongly by the host lattice. Therefore, the electronic transitions between the $4f^n$ and $4f^n5d$ states, through absorption or emission of photons, are expected to be significantly different from those transitions within the $4f^n$ configuration. As the inter-configuration $4f^n$–$4f^n5d$ transitions of the lanthanide ions are parity-allowed, they have intensities up to 10 000 times stronger than the strongest $4f^n$–$4f^n$ transitions.[57]

The choice of host materials is of great importance in designing lanthanide-based luminescent materials for efficient PV applications. As a general rule, the host materials require close lattice matches to the dopant ions and have low phonon energies. Despite the fact that the energy level structure of most lanthanide ions is independent of the host materials, the phonon energy plays an important role in nonradiative transitions due to multiphonon relaxation between closely spaced energy levels. The nonradiative relaxation rate can be estimated with the exponential energy gap law developed by van Dijk and Schuurmans:[58,59]

$$k_{nr} = \beta_{el}\exp(-\alpha(\Delta E - 2\hbar\omega_{max})) \tag{4}$$

where $\beta_{el}$ and $\alpha$ are constants for a given host lattice, $\Delta E$ is the energy difference between the energy levels considered, and $\hbar\omega_{max}$ is the maximum phonon energy. Hosts with low phonon energy may decrease the probability of nonradiative transitions, subsequently leading to high luminescence efficiency. The maximum

Published on 16 October 2012. Downloaded on 11/09/2014 14:42:06.

**Table 1** Principle transitions in the emission spectra of common lanthanide ions utilized in upconversion (UC), quantum-cutting (QC), and down-shifting (DS) luminescence processes for PV applications

| Ln | Ground state | Excited state | Final state | Emission wavelength (nm) | Energy ($cm^{-1}$) | Intensity | Remarks |
|---|---|---|---|---|---|---|---|
| Pr | $^3H_4$ | $^3P_2 \rightarrow$ | $^3H_4$ | 440 | 22 727 | Weak | QC |
| | | $^3P_1 \rightarrow$ | $^3H_4$ | 470 | 21 277 | Weak | QC |
| | | | $^1G_4$ | 872 | 11 468 | Medium | QC |
| | | $^3P_0 \rightarrow$ | $^3H_4$ | 480 | 20 833 | Strong | UC and QC |
| | | | $^3H_5$ | 545 | 18 349 | Weak | UC and QC |
| | | | $^3H_6$ | 606 | 16 502 | Medium | UC and QC |
| | | | $^3F_2$ | 640 | 15 625 | Weak | UC and QC |
| | | $^1D_2 \rightarrow$ | $^3F_4$ | 1037 | 9643 | Medium | QC |
| Nd | $^4I_{9/2}$ | $^4D_{3/2} \rightarrow$ | $^4I_{9/2}$ | 355 | 28 169 | Weak | UC and QC |
| | | $^2P_{3/2} \rightarrow$ | $^4I_{9/2}$ | 380 | 26 316 | Weak | UC and QC |
| | | | $^4I_{11/2}$ | 410 | 24 390 | Strong | UC and QC |
| | | | $^4I_{13/2}$ | 452 | 22 124 | Strong | UC and QC |
| | | $^4G_{7/2} \rightarrow$ | $^4I_{9/2}$ | 545 | 18 349 | Weak to strong | UC and QC |
| | | | $^4I_{11/2}$ | 587 | 17 036 | Weak to strong | UC and QC |
| | | | $^4I_{13/2}$ | 655 | 15 267 | Weak to strong | UC and QC |
| | | $^4F_{3/2} \rightarrow$ | $^4I_{9/2}$ | 886 | 11 287 | Weak to strong | QC and DS |
| | | | $^4I_{11/2}$ | 1064 | 9399 | Strong | QC and DS |
| | | | $^4I_{13/2}$ | 1340 | 7463 | Weak | QC and DS |
| Sm | $^6H_{5/2}$ | $^4G_{5/2} \rightarrow$ | $^6H_{5/2}$ | 564 | 17 730 | Medium | DS |
| | | | $^6H_{7/2}$ | 601 | 16 639 | Strong | DS |
| | | | $^6H_{9/2}$ | 644 | 15 528 | Medium | DS |
| Eu | $^7F_0$ | $^5D_0 \rightarrow$ | $^7F_{0,1,2,3,4}$ | 570–720 | 13 889–17 544 | Strong | UC and DS |
| Tb | $^7F_6$ | $^5D_4 \rightarrow$ | $^7F_{6,5,4,3}$ | 480–650 | 15 385–20 833 | Strong | UC, QC and DS |
| Dy | $^6H_{15/2}$ | $^4F_{9/2} \rightarrow$ | $^6H_{15/2}$ | 486 | 20 576 | Medium | QC and DS |
| | | | $^6H_{13/2}$ | 575 | 17 391 | Strong | QC and DS |
| | | | $^6H_{11/2}$ | 664 | 15 060 | Weak | QC and DS |
| Ho | $^5I_8$ | $^5S_2$, $^5F_4 \rightarrow$ | $^5I_8$ | 540 | 18 519 | Strong | UC and QC |
| | | | $^5I_7$ | 749 | 13 351 | Weak | UC and QC |
| | | | $^5I_6$ | 1012 | 9881 | Weak | QC |
| | | $^5F_5 \rightarrow$ | $^5I_8$ | 644 | 15 528 | Medium | UC and QC |
| | | | $^5I_7$ | 966 | 10 352 | Weak | QC |
| | | $^5I_6 \rightarrow$ | $^5I_8$ | 1180 | 8475 | Strong | QC |
| Er | $^4I_{15/2}$ | $^4G_{11/2} \rightarrow$ | $^4I_{15/2}$ | 380 | 26 316 | Weak | UC and QC |
| | | $^2P_{3/2} \rightarrow$ | $^4I_{13/2}$ | 408 | 24 510 | Weak | UC |
| | | | $^4I_{11/2}$ | 480 | 20 833 | Weak | UC |
| | | $^2H_{11/2} \rightarrow$ | $^4I_{15/2}$ | 525 | 19 048 | Weak | UC and QC |
| | | $^4S_{3/2} \rightarrow$ | $^4I_{15/2}$ | 545 | 18 349 | Strong | UC and QC |
| | | | $^4I_{13/2}$ | 850 | 11 765 | Weak | UC and QC |
| | | $^4F_{9/2} \rightarrow$ | $^4I_{15/2}$ | 665 | 15 038 | Strong | UC and QC |
| | | $^4I_{9/2} \rightarrow$ | $^4I_{15/2}$ | 800 | 12 500 | Strong | UC and QC |
| | | $^4I_{11/2} \rightarrow$ | $^4I_{15/2}$ | 980 | 10 204 | Strong | UC and QC |
| | | $^4I_{13/2} \rightarrow$ | $^4I_{15/2}$ | 1540 | 6494 | Strong | QC |
| Tm | $^3H_6$ | $^1D_2 \rightarrow$ | $^3H_6$ | 360 | 27 778 | Medium | UC and QC |
| | | | $^3F_4$ | 450 | 22 222 | Medium | UC and QC |
| | | $^1G_4 \rightarrow$ | $^3H_6$ | 475 | 21 053 | Strong | UC and QC |
| | | | $^3F_4$ | 650 | 15 385 | Strong | UC and QC |
| | | | $^3H_5$ | 786 | 12 723 | Weak | UC and QC |
| | | $^3H_4 \rightarrow$ | $^3H_6$ | 800 | 12 500 | Strong | UC and QC |
| | | $^3F_4 \rightarrow$ | $^3H_6$ | 1800 | 5556 | Weak | QC |
| Yb | $^2F_{7/2}$ | $^2F_{5/2} \rightarrow$ | $^2F_{7/2}$ | 980 | 10 204 | Strong | UC, QC and DS |

phonon energies of different inorganic host materials are summarized in the following: iodide (160 $cm^{-1}$) < bromide (175–190 $cm^{-1}$) < chalcogenide (200–300 $cm^{-1}$) < fluoride (500–600 $cm^{-1}$) < tellurite (600–850 $cm^{-1}$) < germanate (800–975 $cm^{-1}$) < silicate (1000–1100 $cm^{-1}$) < phosphate (1100 $cm^{-1}$) < borate (1400 $cm^{-1}$).[24]

The most promising phosphors for upconversion and quantum-cutting luminescence are found in fluoride hosts owing to their low phonon energy, high refractive index, and good thermal stability.[33,60,61] For example, $LiGdF_4$:$Eu^{3+}$ shows a quantum efficiency of 1.90,[62,63] and the quantum efficiency of $YF_3$:$Pr^{3+}$ approaches 1.4.[64–66] In contrast, the quantum efficiencies of $Pr^{3+}$-activated oxides are far lower than unity.[67] However, the fluoride phosphors are believed to be unstable under sub-bandgap excitation.

### 2.4 Energy transfer

ET is an important optical process that dominates the luminescence of a material. Spectral conversion by luminescent materials for PV applications mostly relies on the ET between lanthanide ions. Four basic ET mechanisms have been proposed and observed in lanthanide-doped materials: (i) resonant radiative transfer through emission of a sensitizer and re-absorption by an activator; (ii) non-radiative transfer associated with resonance between an absorber (sensitizer) and an emitter (activator); (iii) multiphonon-assisted ET; and (iv) cross-relaxation between two identical ions

This journal is © The Royal Society of Chemistry 2013

Published on 16 October 2012. Downloaded on 11/09/2014 14:42:06.

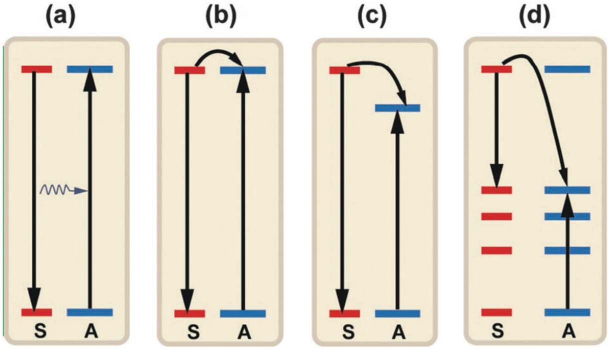

**Fig. 6** A schematic diagram to illuminate the different ET processes between two ions: (a) resonant radiative transfer through emission of a sensitizer and re-absorption by an activator; (b) nonradiative transfer associated with resonance between a sensitizer and an activator; (c) multiphonon assisted ET; and (d) cross-relaxation between two identical ions. S and A denote the sensitizer and activator, respectively.

(Fig. 6).[68] The efficiency of radiative transfer depends on how efficiently the activator fluorescence is excited by the sensitizer emission (Fig. 6a). An efficient ET process requires a significant spectral overlap between the sensitized emission and the absorption of an activator. If a radiative ET takes place predominantly, the decay time of the sensitized luminescence does not vary with the activator concentration. In contrast to the radiative ET, the nonradiative ET (Fig. 6b) is often accompanied by a significant decrease in the decay time of sensitized luminescence *versus* activator concentration. Two other lines of evidence for the occurrence of nonradiative ET are: (i) the presence of an excitation band of the sensitizer in the excitation spectrum of the activator, and (ii) the presence of activator emission found in the emission spectrum when the sensitizer is selectively excited. ET can occur if the energy differences between the ground and excited states of the donor (sensitizer) and the acceptor (activator) are equal and if there exists a suitable interaction, either an exchange interaction or a multipolar interaction, between both systems. Exchange interaction (Dexter ET) depends on the wave function overlap and thus only operates over very short distances ($<0.5$ nm). While multipolar interaction (Förster ET) primarily depends on the strength of the optical transitions involved and can occur for separations as large as 2 nm. Non-resonant ET can also occur with the assistance of phonons unless the differences between the ground and excited states of the donor and acceptor are large.

The Dexter ET probability from a sensitizer (S) to an activator (A) is generally approximated as in eqn (5):[69]

$$P_{\mathrm{SA}} = \frac{2\pi}{\hbar}|\langle \mathrm{S}, \mathrm{A}^{*}|H_{\mathrm{SA}}|\mathrm{S}^{*}, \mathrm{A}\rangle|^{2}\int g_{\mathrm{S}}(E)g_{\mathrm{A}}(E)\mathrm{d}E \tag{5}$$

where $H_{\mathrm{SA}}$ is the interaction Hamiltonian and $\hbar$ is the Planck constant; $\langle$S,A* and $\langle$S*,A represent the initial state and the final state, respectively; the $\int g_{\mathrm{S}}(E)g_{\mathrm{A}}(E)\mathrm{d}E$ integral stands for the spectral overlap; the factors, $g_{\mathrm{S}}(E)$ and $g_{\mathrm{A}}(E)$, denote the normalized spectral feature for the sensitizer emission and activator absorption, respectively; $E$ is the energy involved in the transfer. Eqn (5) shows that the ET probability $P_{\mathrm{SA}}$ vanishes for vanishing spectral overlap. The square of the matrix element in eqn (5) is expressed in terms of the distance-dependent ET probability between the donor and acceptor. The distance dependence of the transfer rate varies with the type of interaction. For exchange interaction the distance dependence is exponential, while for electric multipolar interaction the distance dependence is given by $R^{-n}$ ($n$ = 6, 8,... for electric–dipole electric–dipole interaction, electric–dipole electric–quadrupole interaction,... respectively).

Phonon-assisted ET occurs when the resonance condition is not well met between the sensitizer and the activator, resulting in a small spectral overlap (Fig. 6c). In this case, the mismatch between the transition energies of the sensitizer and the activator is compensated by phonon emission or absorption. According to Miyakawa–Dexter theory,[70] the probability of phonon-assisted transfer is expressed by,

$$P_{\mathrm{PAT}}(\Delta E) = P_{\mathrm{PAT}}(0)\mathrm{e}^{-\beta\Delta E} \tag{6}$$

where $\Delta E$ is the energy gap between the electronic levels of sensitizer and activator ions; $\beta$ is a parameter that depends on the energy and occupation number of participating phonons; and $P_{\mathrm{PAT}}(0)$ is equal to the resonant transfer probability given by eqn (5). Non-resonant phonon-assisted ET between various trivalent lanthanide ions in $\mathrm{Y_2O_3}$ crystals was thoroughly studied by Yamada *et al.*[71] In their experiments, the energy gap between the sensitizer and activator system varied in a wide range of energies up to 4000 cm$^{-1}$. The probability of phonon-assisted ET was measured to have an exponential dependence on the energy gap, in excellent agreement with the Miyakawa–Dexter theory. It was revealed that the phonons of about 400 cm$^{-1}$ in the $\mathrm{Y_2O_3}$ host contribute dominantly to the phonon-assisted process.

Cross-relaxation terminology usually refers to all types of resonant ET between identical ions, acting as both sensitizers and activators. As shown in Fig. 6d, cross-relaxation may give rise to the diffusion process between sensitizers when the levels involved are identical (known as energy migration) or to self-quenching when their levels are different. In the first case there is no loss of energy, whereas in the second there is a loss or change in the energy of the emitted photons.[68] Concentration quenching of luminescence often takes place as a result of cross-relaxation among the activators when the concentration of the activator is above a critical value.

## 3. Upconversion materials for PV applications

### 3.1 Concepts of upconversion

The term upconversion describes nonlinear anti-Stokes optical processes that convert two (or more) low-energy pump photons to a higher-energy output photon.[72,73] This phenomenon was first discovered by Auzel in the 1960s.[74] Since then, there has been a surge of research interest in upconversion due to its applications in a number of diverse fields, such as infrared quantum

Published on 16 October 2012. Downloaded on 11/09/2014 14:42:06.

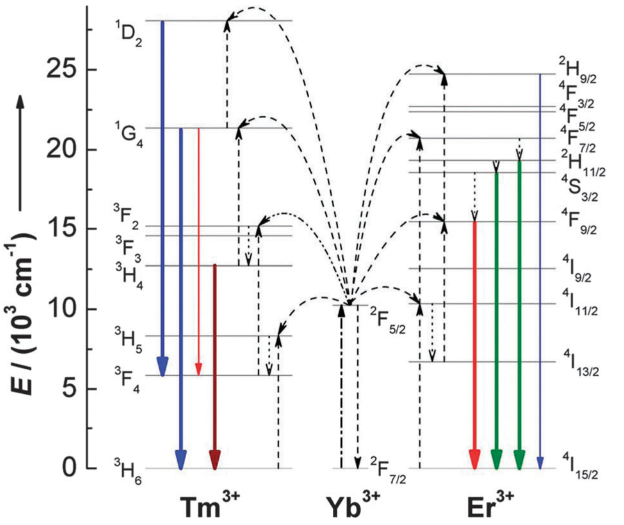

**Fig. 7** Proposed upconversion mechanisms for $Er^{3+}$–$Yb^{3+}$ and $Tm^{3+}$–$Yb^{3+}$ couples under 980 nm diode laser excitation. The dash-dotted, dashed, dotted, and full arrows represent photon excitation, energy transfer, multiphonon relaxation, and emission processes, respectively. Only visible and NIR emissions are shown here. (Reprinted with permission from ref. 77. Copyright 2008, American Chemical Society.)

counter detectors, compact solid-state lasers, temperature sensors, lightings and displays, as well as biomedical imaging.[75–137]

As was already discussed above, only the absorption of photons with energy higher than the bandgap can generate electron–hole pairs contributing to electric current. Indeed, the transmission of sub-bandgap photons is one of the major energy loss mechanisms in conventional solar cells. In the case of c-Si solar cells, the transmission loss amounts to about 20% of the incident solar energy, which is not substantially reducible by conventional approaches. To this end, the use of upconversion materials may provide a solution to the transmission loss by converting two sub-bandgap photons into one above-bandgap photon. Indeed, Trupke *et al.*[32] in 2002 showed that the theoretical efficiency limit of a solar cell, modified with an up-converter, can reach 63.2% for concentrated sunlight and 47.6% for non-concentrated sunlight, respectively.

Although the idea of using upconversion for improving the performance of solar cell devices is implicit, relatively little work has been done until recently. A considerable limitation lies in the fact that upconversion processes are only possible in trivalent lanthanide ions with metastable and long-lived intermediate levels acting as storage reservoirs for the pump energy. In this sense, $Er^{3+}$, $Tm^{3+}$, and $Ho^{3+}$ ions, featuring ladder-like energy levels for facilitating photon absorption and subsequent ET steps, were generally chosen as activators to give rise to efficient visible emissions under low pump power densities. In order to enhance upconversion luminescence efficiency, the $Yb^{3+}$ ion is usually co-doped as an excellent upconversion sensitizer due to its large absorption cross-section in the 900–1100 nm NIR region, corresponding to the $^2F_{5/2} \rightarrow {}^2F_{7/2}$ ($Yb^{3+}$) transition. In fact, the $Er^{3+}$–$Yb^{3+}$ couple is by far the most studied upconversion system (Fig. 7).

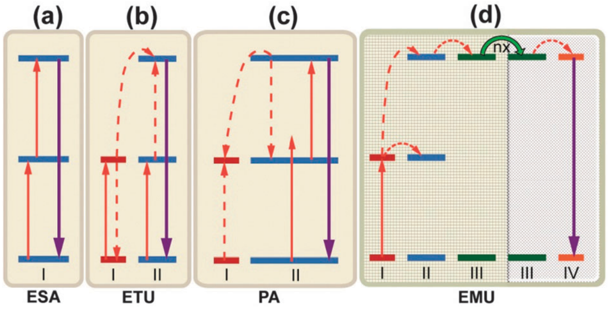

**Fig. 8** Proposed typical upconversion processes. (a) Excited state absorption (ESA); (b) energy transfer upconversion (ETU); (c) photon avalanche (PA). PA is an unconventional mechanism as it could lead to strong upconverted emission without any resonant ground-state absorption when the pump power is above a certain threshold value. The pump wavelength is only resonant between a metastable state and a higher energy level; (d) energy migration-mediated upconversion (EMU) involving the use of four types of lanthanide ions and a core–shell design. Note that core and shell regions are highlighted with different background colors. The 'nx' denotes the occurrence of random hopping through many type-III ions.

A wide variety of upconversion mechanisms have been identified (Fig. 8). For PV applications, the majority of these mechanisms are based on some combination of excited state absorption (ESA) and energy transfer upconversion (ETU) processes. In contrast to common nonlinear processes including two photon absorption and second harmonic generation, these upconversion processes combine the benefit of high quantum efficiency without the need for intense coherent excitation sources, with the inherent advantages of large anti-Stokes shift. ESA is a single-ion process that involves sequential absorption of two (or more) photons by an excited ion using a real intermediary energy level, and results in promotion of that ion to a higher excited state. In ETU, two pump photons excite two neighboring ions to a metastable energy level through ground-state absorption (GSA). The excited ions then exchange energy nonradiatively, promoting one excited ion to an upper emitting state and demoting the other ion to the ground state. Photon avalanche (PA) is an unconventional mechanism as it could lead to strong upconverted emission without any resonant GSA when the pump power is above a certain threshold value.[138] The pump wavelength is only resonant between a metastable state and a higher energy level. The phenomenon of PA upconversion was first reported in $Pr^{3+}$-doped $LaCl_3$ and $LaBr_3$ crystals.[139] Recently, Wang *et al.*[75] proposed the energy migration-mediated upconversion (EMU) involving the use of four types of lanthanide ions and a core–shell structure. Through gadolinium sublattice-mediated energy migration, efficient tunable upconversion emissions in $NaGdF_4$:$Tm^{3+}$/$Yb^{3+}$@$NaGdF_4$:$Ln^{3+}$ core–shell nanoparticles were realized for various lanthanide activators ($Ln^{3+}$ = $Eu^{3+}$, $Tb^{3+}$, $Dy^{3+}$, and $Sm^{3+}$) without long-lived intermediary energy states.

The use of upconversion materials for improving PV system performance was first reported by Gibart's group[140] in 1996 using the $Er^{3+}$-$Yb^{3+}$ couple in bifacial GaAs solar cells. Since then, many groups have pursued the development of various upconversion-based PV devices to enhance the conversion

Published on 16 October 2012. Downloaded on 11/09/2014 14:42:06.

**Table 2** Selected lanthanide-doped upconversion materials used for PV applications

| Dopant ion | Host lattice | Preparation method | Excitation (nm) | Emission (nm) | Solar cell type | Ref. |
|---|---|---|---|---|---|---|
| $Er^{3+}$ | $NaYF_4$ | Solid-state reaction | 1523 | 550, 660, 800, 980 | c-Si | 141 |
| $Er^{3+}$ | $NaYF_4$ | — | 1523 | 545, 670, 800, 980 | c-Si | 142 |
| $Er^{3+}$ | $CaF_2$ | — | 1550 | 660, 980 | c-Si | 143 |
| $Er^{3+}$ | $Gd_2(MoO_4)_3$ | Combustion synthesis | 1530 | 545, 665, 800, 980 | c-Si | 144 |
| $Er^{3+}$ | $Y_2O_3$ | Template technology | 1538 | 562, 659, 801, 987 | c-Si | 145 |
| $Er^{3+}$ | Fluoride glasses | Glass melting | 1532 | 550, 660, 820, 980 | c-Si | 146 |
| $Ho^{3+}$ | Glass ceramics containing $PbF_2$ nanocrystals | Glass melting | 1170 | 650, 910 | c-Si | 147 |
| $Ho^{3+}$–$Yb^{3+}$ | Fluoroindate glass | Glass melting | 1155 | 550, 650, 750, 905, 980 | c-Si | 148 |
| $Er^{3+}$–$Yb^{3+}$ | $Y_6W_2O_{15}$ | Solid-state reaction | 973 | 516–570 | GaAs | 149 |
| $Er^{3+}$–$Yb^{3+}$ | $NaYF_4$ | Hydrothermal method | 980 | 525, 540, 655 | Amorphous Si | 150,151 |
| $Er^{3+}$–$Yb^{3+}$ | $NaYF_4$ | Solid-state reaction | 980 | 522, 540, 653 | Amorphous Si | 152 |
| $Er^{3+}$–$Yb^{3+}$ | $NaYF_4$ | Hydrothermal method | 980 | 524, 540, 660 | Amorphous Si | 153 |
| $Er^{3+}$–$Yb^{3+}$ | Glass ceramic containing $NaYF_4$ nanocrystals | Glass melting | 980 | 520, 538, 656 | Amorphous Si | 154 |
| $Er^{3+}$ | $Y_2O_3$ | Hydrothermal method | 980 | 525, 550, 660 | Dye-sensitized | 155 |
| $Er^{3+}$–$Yb^{3+}$ | $LaF_3$ | Solvothermal synthesis | 980 | 543, 655 | Dye-sensitized | 156 |
| $Er^{3+}$–$Yb^{3+}$ | $NaYF_4$ | Hydrothermal method | 980 | 510–570, 640–680 | Dye-sensitized | 157 |
| $Er^{3+}$–$Yb^{3+}$ | $NaYF_4$ : Er,Yb@$NaYF_4$ | Thermal decomposition | 976 | 510–570, 635–700 | Dye-sensitized | 158 |
| $Er^{3+}$–$Yb^{3+}$ | $YF_3$ | Thermal decomposition | 980 | 525, 545, 656 | Dye-sensitized | 159 |
| $Er^{3+}$–$Yb^{3+}$ | YAG transparent ceramics | Solid-state reaction | 980 | 520, 563, 677 | Dye-sensitized | 160 |
| $Tm^{3+}$–$Yb^{3+}$ | $Lu_2O_3$ | Co-precipitation | 980 | 476, 653 | Dye-sensitized | 161 |
| $Tm^{3+}$–$Yb^{3+}$ | Glass ceramics containing $PbF_2$ nanocrystals | Glass melting | 980 | 475, 650, 800 | Dye-sensitized | 162 |
| $Er^{3+}$–$Yb^{3+}$ | $YF_3$ | — | 975 | 510–560 | Organic | 163 |
| $Ho^{3+}$–$Yb^{3+}$ | $Y_2BaZnO_5$ | Solid-state reaction | 986 | 545 | Organic | 164 |

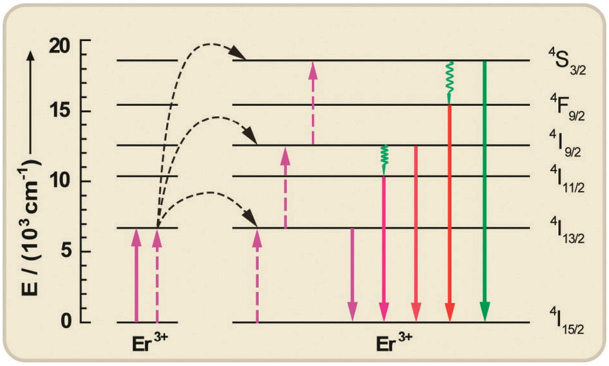

**Fig. 9** Upconversion processes *via* the ETU mechanism between two $Er^{3+}$ ions, resulting in c-Si above-bandgap emissions under c-Si sub-bandgap pump excitation (1520 nm). Solid, dotted, and wavy arrows represent photon absorption/emission, energy transfer, and multiphonon relaxation, respectively.

efficiency (Table 2).[141–164] Upconversion materials singly-doped with $Er^{3+}$ or $Ho^{3+}$, capable of converting long-wavelength NIR light into short-wavelength NIR and visible emissions, can be combined with narrow bandgap c-Si solar cells ($E_g$ = 1.12 eV; 1100 nm). For PV devices using wide bandgap semiconductors, such as GaAs ($E_g$ = 1.43 eV; 867 nm)[165] and amorphous Si ($E_g$ = 1.75 eV; 708 nm),[166] the utilization of upconversion materials co-doped with $Ln^{3+}$–$Yb^{3+}$ couples is very convenient due to the efficient ETU from the $Yb^{3+}$ sensitizer to various $Ln^{3+}$ activators.

### 3.2 Upconversion for c-Si solar cells

$Er^{3+}$ ION. $Er^{3+}$-doped upconversion materials are the most promising upconverters for c-Si solar cells due to the GSA of $Er^{3+}$ in the range of 1480–1580 nm ($^4I_{15/2} \rightarrow {}^4I_{13/2}$ transition). The GSA centered at about 1540 nm results in upconversion *via* an ETU mechanism, giving rise to four emission bands: $^4I_{11/2} \rightarrow {}^4I_{15/2}$, 980 nm; $^4I_{9/2} \rightarrow {}^4I_{15/2}$, 810 nm; $^4F_{9/2} \rightarrow {}^4I_{15/2}$, 660 nm; and $^4S_{3/2} \rightarrow {}^4I_{15/2}$, 550 nm (Fig. 9). These emission bands match well with the absorption of c-Si. Note that the exact emission wavelength can vary by ±10 nm, depending on the host material (Table 2).

Shalav *et al.*[141] in 2005 reported the application of $NaYF_4$:$Er^{3+}$ (20 mol%) phosphors as the upconverters in a bifacial c-Si solar cell. These phosphors were mixed into an optically transparent acrylic adhesive medium at a concentration of 40 wt% and then placed on the rear of a bifacial c-Si solar cell. Reflective white paint was used as a reflector on the rear of the system. An external quantum efficiency of 2.5% was obtained for the solar cell under excitation at 1523 nm with a 5.1 mW laser. More recently, Fischer and co-workers[142] also investigated the potential of $NaYF_4$:$Er^{3+}$ to significantly reduce the sub-bandgap losses of c-Si solar cells. The optical upconversion efficiency of $NaYF_4$:$Er^{3+}$ (20 mol%) was determined to be about 5.1% upon excitation at 1523 nm with a power density of 1880 W $m^{-2}$. The c-Si solar cell device combined with an upconverter showed an external quantum efficiency of 0.34% upon irradiation at 1522 nm with a power density of 1090 W $m^{-2}$.

$Ho^{3+}$ ION. The $Ho^{3+}$ ion has a relatively wide absorption band in the 1150–1225 nm spectral range due to $^5I_8 \rightarrow {}^5I_6$ transition. The irradiation power density of sunlight in this spectral range is about 40 W $m^{-2}$, which is approximately twice more intense than that in the 1480–1580 nm range. Lahoz[147] in 2008 reported the use of $Ho^{3+}$ singly-doped oxyfluoride glass ceramics as promising upconverters for efficiency enhancement in c-Si solar cells. Under sub-bandgap excitation at 1170 nm, upconversion emissions in the visible (~650 nm, $^5F_5 \rightarrow {}^5I_8$ transition) and NIR

Published on 16 October 2012. Downloaded on 11/09/2014 14:42:06.

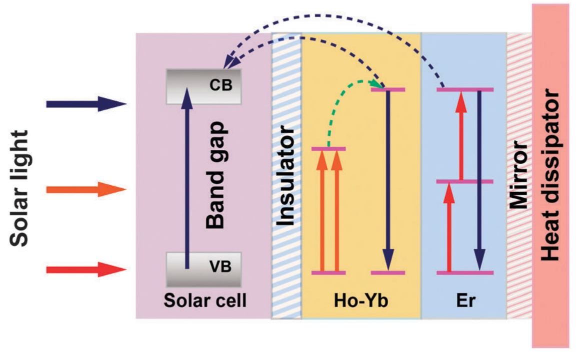

**Fig. 10** A proposed operating mechanism for a c-Si solar cell with $Ho^{3+}$–$Yb^{3+}$ and $Er^{3+}$ doped upconverters. Above-bandgap light (highlighted in blue color) is directly absorbed by the solar cell, which is electronically isolated from the upconverter. The sub-bandgap light (highlighted in orange and red colors) transmitted by the solar cell is stepwise upconverted into high-energy photons, which are subsequently absorbed in the solar cell. A mirror reflector is located behind the upconverter. CB and VB are the conduction and valence bands of c-Si, respectively. The energy gap between VB and CB is around 1.12 eV for c-Si.

(~910 nm, $^5I_5 \rightarrow {}^5I_8$ transition) spectral ranges have been obtained *via* the ETU mechanism.

In a following paper, Lahoz *et al.*[148] co-doped $Ho^{3+}$ with $Yb^{3+}$ and found enhanced emission intensity of NIR-to-NIR upconversion as a result of ET from $Ho^{3+}$ to $Yb^{3+}$ ions. Importantly, owing to the high transparency to the excitation wavelength of ~1540 nm, these $Ho^{3+}$-based glass ceramics could be used in combination with $Er^{3+}$-doped upconverters. The authors proposed a double-layer design with the $Ho^{3+}$-doped upconverting layer placed directly at the rear surface of a bifacial c-Si solar cell, followed by the $Er^{3+}$-doped upconverter and a mirror (Fig. 10). The integration of both upconverters would enlarge the absorption of the solar sub-bandgap spectral range exploited for enhancing the c-Si solar cell response.

An alternative design proposed by Chen *et al.* in 2012 is to adopt a core–shell nanostructure, in which $Er^{3+}$ and $Ho^{3+}$ activators are separately incorporated into the core and shell layer of a nanoparticle.[167] The use of a core–shell layout can extend the NIR wavelength range excitable for upconversion emission, and furthermore allow facile modulation of activator concentration while minimizing luminescence quenching induced by the deleterious cross-relaxation ET between the $Er^{3+}$ and $Ho^{3+}$ ions. As a proof-of-concept experiment, the authors fabricated monodisperse $NaGdF_4{:}Er^{3+}@NaGdF_4{:}Ho^{3+}@NaGdF_4$ core–shell–shell nanoparticles. The middle protection shell not only enhances the upconversion luminescence of $Er^{3+}$ in the core, but also acts as the host to realize the upconversion luminescence of $Ho^{3+}$. As a result, intense upconversion emissions for both $Er^{3+}$ and $Ho^{3+}$ dopants were achieved.

### 3.3 Upconversion for wide bandgap solar cells

GaAs solar cells. In 1996, Gibart *et al.*[140] reported the application of a 100 μm thick vitroceramic co-doped with $Er^{3+}$–$Yb^{3+}$ on the rear of a substrate-free GaAs solar cell. Under 891 nm (1.391 eV) excitation, upconverted green ($^4S_{3/2} \rightarrow {}^4I_{15/2}$ transition) and red ($^4F_{9/2} \rightarrow {}^4I_{15/2}$ transition) emissions from $Er^{3+}$ ions were observed. The photoresponse of the GaAs solar cell increased quadratically with the input excitation. The measured efficiency was 2.5% under 25.6 W $cm^{-2}$ illumination at 891 nm. In 2012, Lin *et al.*[149] further validated the concept by adhering a 300 μm thick layer of $Y_6W_2O_{15}{:}Er^{3+}/Yb^{3+}$ upconversion phosphors to the rear of a GaAs solar cell. The authors obtained a maximum output power of 0.339 μW when illuminated with a 973 nm laser at 145.65 W $cm^{-2}$. However, compared to the $Er^{3+}$–$Yb^{3+}$ couple, the $Tm^{3+}$–$Yb^{3+}$ couple with NIR-to-NIR upconversion luminescence (~980 nm excitation, ~800 nm emission)[168–175] is likely to be more suitable for application in GaAs solar cells ($E_g$ = 1.43 eV; 867 nm) due to a larger emission and absorption spectral overlap.

Amorphous silicon solar cells. Amorphous Si solar cells with a bandgap of ~1.75 eV only absorb NIR light shorter than 708 nm. To extend the absorption limit, upconversion of sub-bandgap NIR light ($\lambda$ > 700 nm) to visible emission using $NaYF_4$:Er/Yb phosphors can be combined with the amorphous Si solar cells. These upconversion phosphors have visible emission bands at around 525, 540, and 655 nm located in the spectral region where the solar cells have high internal collection efficiency. To this end, Zhang *et al.*[150] in 2010 reported the fabrication of an amorphous Si solar cell device composed of $NaYF_4$:Er/Yb (2/18 mol%) nanocrystals. These authors reported that the incorporation of an upconverting layer into the solar cell could effectively increase the short circuit current density from 16 to 17 mA $cm^{-2}$.

The same upconversion phosphor was also used by de Wild *et al.*[151,152] to demonstrate enhanced conversion efficiency in amorphous Si solar cells. In their experiments, the upconversion powders were mixed with polymethylmethacrylate and then made into an upconverter layer with thickness of 200–300 μm. A maximum current enhancement of 6.2 mA was measured under 980 nm diode laser illumination at 28 mW. More recently, a 72-fold enhancement in photocurrent under 980 nm illumination was achieved by Li *et al.*[153] using $NaYF_4{:}Yb^{3+}/Er^{3+}/Gd^{3+}$ nanorod-modified electrodes in an amorphous Si solar cell, as compared to the PV cell without an upconverter.

Dye-sensitized solar cells. Dye-sensitized solar cells (DSSCs) are next-generation PV cells that can be used to create low-cost, flexible solar panels.[176–179] Unlike conventional Si-based solar cells, DSSCs primarily consist of photosensitive dyes and other substances such as an electrolyte solution and metal oxide nanoparticles. Despite great efforts, the improvement in the efficiency of state-of-the-art DSSCs remains a daunting task, largely due to the limited absorption spectrum of currently available dyes.[180–182] The most commonly used dyes in current DSSCs are ruthenium-based dyes, including N3 ($[Ru(dcbpyH_2)_2(NCS)_2]$, $dcbpyH_2$ = 2,2′-bipyridyl-4,4′-dicarboxylic acid), N719 ($[(C_4H_9)_4N]_2[Ru(dcbpyH)_2(NCS)_2]$), and N749 ($[(C_4H_9)_4N]_3[Ru(tcterpy)(NCS)_3]{\cdot}3H_2O$, tcterpy = 4,4′,4″-tricarboxy-2,2′:6′,2″-terpyridine). As a result of their large optical bandgap of 1.8 eV, these dyes have an absorption threshold below ~700 nm. To achieve higher efficiencies for DSSCs, light absorption must be extended into the NIR spectral region without sacrificing their performance in the visible region. In 2010, Shan and

This journal is © The Royal Society of Chemistry 2013

Published on 16 October 2012. Downloaded on 11/09/2014 14:42:06.

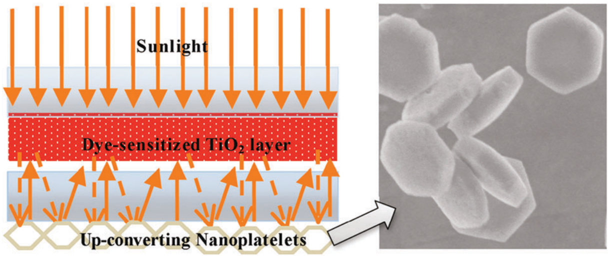

**Fig. 11** Schematic configuration of a DSSC device consisting of one internal $TiO_2$ transparent layer and an external rear layer of $NaYF_4:Er^{3+}/Yb^{3+}$ hexagonal nanoplatelets. The external upconverting layer can simultaneously reflect scattered light and harvest NIR light. (Reprinted with permission from ref. 157. Copyright 2011, American Chemical Society.)

Demopoulos[156] reported, for the first time, the application of lanthanide-doped upconversion materials for enhancing the NIR sunlight harvesting in DSSCs. In their studies, the $Er^{3+}$–$Yb^{3+}$ co-doped $LaF_3$–$TiO_2$ nanocomposite was used as an upconversion layer to fabricate a triple-layer working electrode for DSSCs. The green emission at around 543 nm generated by the upconversion nanocomposite can be efficiently absorbed by the N719 dye, which indeed leads to photocurrent generation upon 980 nm laser excitation. However, this structure configuration was proved to be ineffective in delivering a higher photocurrent output due to apparent charge recombination at the interfaces of the triple-layer electrolyte.

In a following paper by Shan *et al.*,[157] different upconversion materials consisting of $NaYF_4:Er^{3+}/Yb^{3+}$ hexagonal nanoplatelets (particle size ~800 nm) were tested in DSSCs. The upconverting phosphors were directly placed on the rear side of a counter electrode (Fig. 11). This design enables a dual-mode functionality that provides both light reflection and NIR light harvesting. Photocurrent was observed for the DSSC device when illuminated with a 980 nm fiber laser, clearly demonstrating the upconverting function of the $NaYF_4:Er^{3+}/Yb^{3+}$ nanomaterials. Importantly, this novel DSSC configuration greatly overcomes the drawback of charge recombination induced by the conducting upconversion layer when used internally. Moreover, the authors found that under AM 1.5G filtered spectral illumination (100 mW $cm^{-2}$) approximately 10% enhancement in both photocurrent and overall conversion efficiency can be achieved by addition of the upconverting layer, which was predominantly attributable to its light reflecting role. Several other groups also reported the enhanced NIR response of the DSSCs by using upconverting materials doped with $Er^{3+}$,[155] $Er^{3+}$–$Yb^{3+}$,[158–160] and $Tm^{3+}$–$Yb^{3+}$.[161]

ORGANIC SOLAR CELLS. Organic solar cells are light-weight and flexible, leading to inexpensive, large-scale production for solar energy conversion.[183–187] One of the major energy losses in organic solar cells is the sub-bandgap transmission as a result of the mismatch between the absorption properties of polymer materials and the terrestrial solar spectrum. The current organic PV cells with best performance are made of bulk heterojunctions comprising poly(3-hexylthiophene) (P3HT) and the fullerene derivative [6,6]-phenyl-$C_{61}$-butyric acid methyl ester (PCBM).[188–191] Owing to the large bandgap of organic molecules, the bulk heterojunction-based PV cells are only able to harvest the visible sunlight. In an attempt to utilize the NIR part of the solar spectrum, Wang *et al.*[163] in 2011 demonstrated the feasibility of upconversion in P3HT:PCBM organic solar cells. By using commercial $LaF_3:Yb^{3+}/Er^{3+}$ phosphors, the authors obtained an upconversion efficiency of ~0.19% (excitation density: 250 mW $cm^{-2}$) and an upconverted photocurrent density of ~16.5 μA $cm^{-2}$ (excitation density: 25 mW $cm^{-2}$) under 975 nm laser diode illumination. In their following paper published in 2012, a semiconducting nanofilm of $MoO_3:Yb^{3+}/Er^{3+}$ was incorporated into P3HT:PCBM solar cells as a buffer layer that enables both hole extraction and upconversion capabilities.[192] The authors found that less than 1% of the short-circuit current was obtained from the upconversion effect under one-sun AM1.5G illumination. Wu and co-workers in 2012 observed an enhancement of 5 μA in the short-circuit current under 980 nm laser illumination of $NaYF_4:Yb^{3+}/Er^{3+}$ nanocrystals placed on the rear side of P3HT:PCBM solar cells.[193]

In 2012, Adikaari *et al.* applied $Y_2BaZnO_5:Ho^{3+}/Yb^{3+}$ upconversion phosphors to PCDTBT:PCBM (PCDTBT: poly[*N*-9′-heptadecanyl-2,7-carbazole-*alt*-5,5(4′,7′-di-2-thienyl-2′,1′,3′-benzothiadiazole]) organic solar cells in order to utilize the NIR solar spectrum.[164] The authors adopted two different layout designs for the PV device as shown in Fig. 12a and b. The PCDTBT:PCBM active layer showed little absorption for light with wavelengths above 700 nm, while the $Y_2BaZnO_5:Er^{3+}/Yb^{3+}$ phosphors exhibited a broad absorption band in the region of 870–1030 nm due to the $^2F_{7/2} \rightarrow {}^2F_{5/2}$ ($Yb^{3+}$) transition (Fig. 12c). Moreover, the main upconversion emission at 545 nm that corresponds to $^5S_2,{}^5F_4 \rightarrow {}^5I_8$ ($Ho^{3+}$) transition matches well with the absorption of the PCDTBT:PCBM photoactive layer (Fig. 12d). Their PV measurements showed that with the upconversion phosphors placed behind the device, a maximum photocurrent density of 16 μA $cm^{-2}$ and a

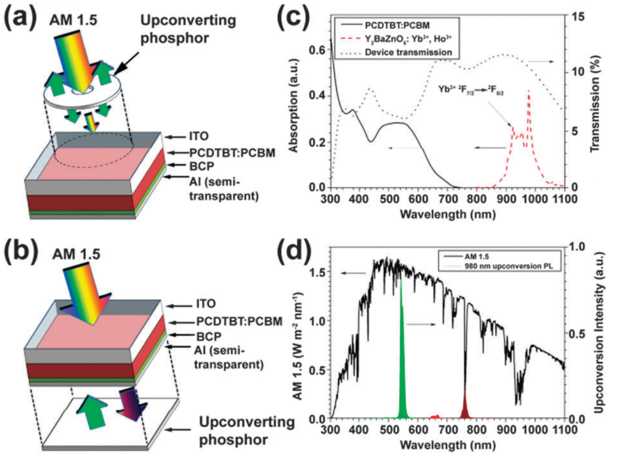

**Fig. 12** Schematic design of an organic PV device with upconversion phosphors placed (a) in front of or (b) behind the device. (c) Absorption spectra of PCDTBT:PCBM and $Ho^{3+}$–$Yb^{3+}$ co-doped $Y_2BaZnO_5$ phosphors and the corresponding transmission spectrum of the PV device. (d) AM1.5G spectrum and upconversion emission spectrum of $Ho^{3+}$–$Yb^{3+}$ co-doped $Y_2BaZnO_5$ phosphors under 986 nm excitation. Note that the separation distance between the phosphor layer and the device is ~0.5 mm. ITO and BCP refer to indium tin oxide and bathocuproine, respectively. (Reprinted with permission from ref. 164. Copyright 2012, American Institute of Physics.)

Published on 16 October 2012. Downloaded on 11/09/2014 14:42:06.

power conversion efficiency of 0.45% were obtained when illuminated with a 986 nm laser (excitation density: $\sim$390 mW cm$^{-2}$).

Before the conversion efficiency of PV devices can be further improved through use of upconversion materials, though, it will be necessary to put some effort into addressing a number of challenges. First, only a small fraction of the solar spectrum can be upconverted by Ln$^{3+}$-doped materials because of their weak and narrowband absorption, so the next step will be to explore methods that enable broadband upconversion. More significantly, new materials or technologies enabling high upconversion efficiency must be developed as upconversion is a nonlinear process with low conversion efficiency (typically less than 3%).[194] A high-density excitation, controlled by a pulsed laser, can enhance upconversion efficiency. But for practical PV applications, the need for concentrated solar power clearly complicates the manufacture of solar cells. In this regard, photon upconversion based on sensitized triplet–triplet annihilation (TTA) involving chromophores could be utilized for wide bandgap solar cells. This emerging technology offers relatively high upconversion efficiency under low excitation power density (a few mW cm$^{-2}$).[195–198] Sunlight is sufficient to excite the chromospheres and sensitize the upconversion process. However, a significant drawback of TTA is that the upconverted spectrum is generally limited in the range of 650–700 nm.[199] Although several groups have recently reported the TTA-based NIR-to-visible upconversion, thus far the attempts to obtain efficient upconverted emissions at wavelengths beyond 800 nm have not been successful.[200–202]

## 4. Quantum-cutting materials for PV applications

### 4.1 Concepts of quantum-cutting

There are certain phosphor materials that can transform the energy of one absorbed photon into two (or more) emitted low-energy photons. This process is known as quantum-cutting with quantum efficiency more than 100%.[33] In general, quantum-cutting can be realized by photon cascade emission from a single lanthanide ion (*e.g.* Pr$^{3+}$[64–66] and Gd$^{3+}$[203]) or by down-conversion *via* ET through different sets of lanthanide ions (*e.g.* Gd$^{3+}$–Eu$^{3+}$[62,63] and Gd$^{3+}$–Tb$^{3+}$–Er$^{3+}$).[204] The first successful demonstration of efficient visible quantum-cutting in a LiGdF$_4$:Eu$^{3+}$ phosphor was reported by Wegh *et al.* in 1999 with a theoretical quantum efficiency of 190%.[62,63] The search for new quantum-cutting materials has gained importance in recent times in view of their promising applications in plasma display panels and mercury-free fluorescent tubes.[33,205–221]

Recently, the potential of using quantum-cutting phosphors in c-Si solar cells has been explored in an effort to maximize their efficiency.[222] Trupke *et al.* have performed theoretical calculations that predict an enhancement up to 38.6% in conversion efficiency for a solar cell modified with a quantum-cutting layer.[34] The NIR quantum-cutting has been demonstrated in various Ln$^{3+}$–Yb$^{3+}$ (Ln = Tb, Tm, Pr, Er, Nd, Ho, and Dy) co-doped systems (Table 3)[223–237] and in phosphors with a single luminescent center (Ho$^{3+}$, Tm$^{3+}$, or Er$^{3+}$).[238–243]

Several mechanisms responsible for the NIR quantum-cutting are illustrated in Fig. 13. The first mechanism is based on one luminescent center with three energy levels (Fig. 13a). It is possible to sequentially produce two NIR photons after transition of the optical center to the highest energy level by absorption of one ultraviolet or visible photon. The intermediate level is shortly populated before the optical center returns to its ground state. Representative examples have been reported for single ions like Ho$^{3+}$, Tm$^{3+}$, or Er$^{3+}$.[238–243] However, one major problem presented by single ion-based quantum-cutting is the unwanted emissions in the ultraviolet–visible spectral range and nonradiative recombination that compete with the desired emission of two NIR photons.

Alternative mechanisms involving two luminescent centers for NIR quantum-cutting are summarized in Fig. 13b–e. A plausible mechanism occurs *via* a two-step ET process through ion pairs of physically interacting lanthanide ions, accompanied by the emission of two NIR photons (Fig. 13b). This quantum-cutting mechanism has been reported in Pr$^{3+}$–Yb$^{3+}$,[230] Er$^{3+}$–Yb$^{3+}$,[232] Nd$^{3+}$–Yb$^{3+}$,[233] Ho$^{3+}$–Yb$^{3+}$,[236] and Dy$^{3+}$–Yb$^{3+}$ co-doped systems.[237] The emission of two NIR photons can also be achieved by quantum-cutting involving one-step ET between two optical centers (Fig. 13c and d). The quantum-cutting mechanism illustrated in Fig. 13c has been experimentally validated for phosphors doped with Tm$^{3+}$–Yb$^{3+}$,[228] Er$^{3+}$–Yb$^{3+}$,[231] and Ho$^{3+}$–Yb$^{3+}$ couples.[234,235] To the authors' knowledge, there is no experimental investigation reported on the mechanism shown in Fig. 13d.

The quantum-cutting mechanisms discussed in Fig. 13b–d require resonance ET between two optical centers in close proximity. The ET can be described as a first-order rate process, governed by the degree of overlap between the donor emission and the acceptor absorption. Energy splitting is plausible by population of an intermediate energy level of the donor. In contrast, if there is no spectral overlap, a second-order cooperative sensitization may dominate the relaxation process, resulting in simultaneous excitation of two acceptors and subsequent emission of two NIR photons (Fig. 13e). For efficient cooperative sensitization to be observed, the sum of the energy of the absorption transitions of the two acceptors must equal the energy of the donor emission.[223] This cooperative quantum-cutting has been extensively investigated in Tb$^{3+}$–Yb$^{3+}$,[223–225] Tm$^{3+}$–Yb$^{3+}$,[226,227] and Pr$^{3+}$–Yb$^{3+}$ co-doped systems.[226,229] While the performance enhancement achieved was encouraging, it should be noted that the possibility of the second-order cooperative ET process is about 1000 times lower than that of the first-order resonant ET process.[230] Thus, a high doping content of Yb$^{3+}$ is typically required for realizing efficient cooperative quantum-cutting.

### 4.2 Narrowband quantum-cutting for c-Si solar cells

TB$^{3+}$–YB$^{3+}$ COUPLE. NIR quantum-cutting for Tb$^{3+}$–Yb$^{3+}$ co-doped systems was first reported by Vergeer *et al.* in 2005 on Yb$_x$Y$_{1-x}$PO$_4$:Tb$^{3+}$ powder phosphors.[223] In their study, a cooperative quantum-cutting mechanism was proposed by

Published on 16 October 2012. Downloaded on 11/09/2014 14:42:06.

**Table 3** Selected narrowband NIR quantum-cutting materials co-doped with $Ln^{3+}$–$Yb^{3+}$ for PV applications

| Dopant ion | Host lattice | Preparation method | Excitation (nm) | ET type | Maximum quantum efficiency (%) | Ref. |
|---|---|---|---|---|---|---|
| $Tb^{3+}$–$Yb^{3+}$ | $YPO_4$ | Solid-state reaction | 489 | Second-order cooperative | 188 | 223 |
| $Tb^{3+}$–$Yb^{3+}$ | $GdBO_3$ | Combustion synthesis | 486 | Second-order cooperative | 182 | 224 |
| $Tb^{3+}$–$Yb^{3+}$ | $Zn_2SiO_4$ thin-films | Sol–gel method | 485 | Second-order cooperative | 162 | 225 |
| $Tm^{3+}$–$Yb^{3+}$ | $GdAl_3(BO_3)_4$ | Combustion synthesis | 475 | Second-order cooperative | 164 | 226 |
| $Tm^{3+}$–$Yb^{3+}$ | Glass ceramics containing $LaF_3$ nanocrystals | Glass melting | 468 | Second-order cooperative | 162 | 227 |
| $Tm^{3+}$–$Yb^{3+}$ | $YPO_4$ | Co-precipitation | 468 | First-order phonon-assisted | 175 | 228 |
| $Pr^{3+}$–$Yb^{3+}$ | $GdAl_3(BO_3)_4$ | Combustion synthesis | 489 | Second-order cooperative | 165 | 226 |
| $Pr^{3+}$–$Yb^{3+}$ | $NaYF_4$ | Hydrothermal method | 443 | Second-order cooperative | 181 | 229 |
| $Pr^{3+}$–$Yb^{3+}$ | $SrF_2$ | Solid-state reaction | 441 | First-order resonant | 140 | 230 |
| $Er^{3+}$–$Yb^{3+}$ | $NaYF_4$ | Solid-state reaction | 380 | First-order resonant | 128 | 231 |
| $Er^{3+}$–$Yb^{3+}$ | $Cs_3Y_2Br_9$ | Vertical Bridgman | 490 | First-order resonant | 195 | 232 |
| $Nd^{3+}$–$Yb^{3+}$ | $YF_3$ | Co-precipitation | 360 | First-order resonant | 140 | 233 |
| $Ho^{3+}$–$Yb^{3+}$ | Glass ceramics containing $YF_3$ nanocrystals | Glass melting | 488 | First-order resonant | 159 | 234 |
| $Ho^{3+}$–$Yb^{3+}$ | $NaYF_4$ | Hydrothermal method | 535 | First-order resonant | 182 | 235 |
| $Ho^{3+}$–$Yb^{3+}$ | $NaYF_4$ | Hydrothermal method | 359 | First-order resonant | 155 | 236 |
| $Dy^{3+}$–$Yb^{3+}$ | Zeolites | Ion-exchange process | 430 | First-order resonant | – | 237 |

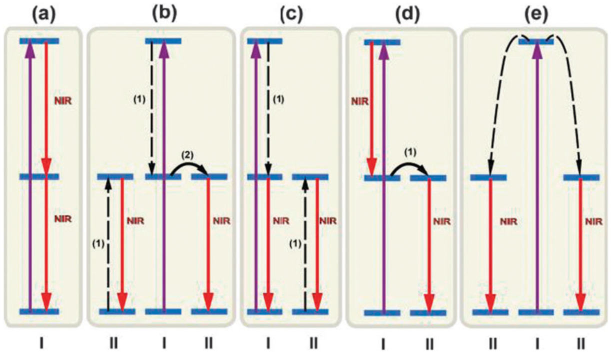

**Fig. 13** Summary of typical mechanisms of NIR quantum-cutting for PV applications. Simplified energy level diagrams for ions (types I and II) are given to illustrate the concept of NIR quantum-cutting. (a) NIR quantum-cutting on a single ion by the sequential emission of two NIR photons. (b–d) NIR quantum-cutting due to resonant ET from ion I to ion II. (e) NIR quantum-cutting due to cooperative ET from ion I to ion II. Note that two type II ions simultaneously emit two photons in the NIR spectral region. The purple solid, red solid, and dashed arrows represent excitation, emission, and ET processes (cross-relaxation for b,c and cooperative ET for e), respectively.

analyzing the luminescence decay curve of $Tb^{3+}$ as a function of $Yb^{3+}$ concentration using Monte Carlo simulations (Fig. 14a). For the $Tb^{3+}$–$Yb^{3+}$ couple, the $^5D_4 \rightarrow {}^7F_6$ transition of $Tb^{3+}$ ($\sim$20 000 $cm^{-1}$) is approximately twice the energy of the $^2F_{7/2} \rightarrow {}^2F_{5/2}$ transition of $Yb^{3+}$ ($\sim$10 000 $cm^{-1}$).

The ET process from $Tb^{3+}$ to $Yb^{3+}$ was investigated by the steady-state and time-resolved luminescence spectroscopy. The ET and quantum efficiencies were calculated from the luminescence decay curves using the following equations,

$$\eta_{ET} = \eta_{x\%Yb} = 1 - \frac{\int I_{x\%Yb}dt}{\int I_{0\%Yb}dt} \tag{7}$$

$$\eta_{QE} = \eta_{Tb}(1 - \eta_{ET}) + 2\eta_{ET} \tag{8}$$

where $I$ denotes intensity, $x$%Yb stands for $Yb^{3+}$ concentration, and $\eta_{Tb}$ represents quantum efficiency for $Tb^{3+}$ and is set to 1.

Although various $Tb^{3+}$–$Yb^{3+}$ co-doped materials have been well studied, the issue of the underlying ET mechanism from $Tb^{3+}$ to $Yb^{3+}$ ions is still debatable.[244–249] Some researchers believed that a nonlinear second-order downconversion process should be responsible for the cooperative quantum-cutting (Fig. 14a).[244,245] The slope of $Yb^{3+}$ luminescence intensity *versus* the excitation power was found to be nearly 0.5, indicating the emission of two lower-energy photons upon the absorption of one photon. On the other hand, two different groups found the slope of luminescence intensity curves to be near 1 instead of 0.5, indicating a one-photon process for the $Yb^{3+}$ NIR emission.[246,247] A similar result was also obtained by Duan and co-workers in $Tb^{3+}$–$Yb^{3+}$ co-doped oxyfluoride glass,[248] but they attributed it to a linear cooperative quantum-cutting mechanism. In this case, a virtual energy level of $Tb^{3+}$ located around 10 000 $cm^{-1}$ could participate in the quantum-cutting process (Fig. 14a), and the downconversion emission intensity would increase linearly with the excitation intensity (Fig. 14b). Interestingly, it was experimentally found that in $NaYF_4$ host materials the slopes of $Yb^{3+}$ luminescence

Published on 16 October 2012. Downloaded on 11/09/2014 14:42:06.

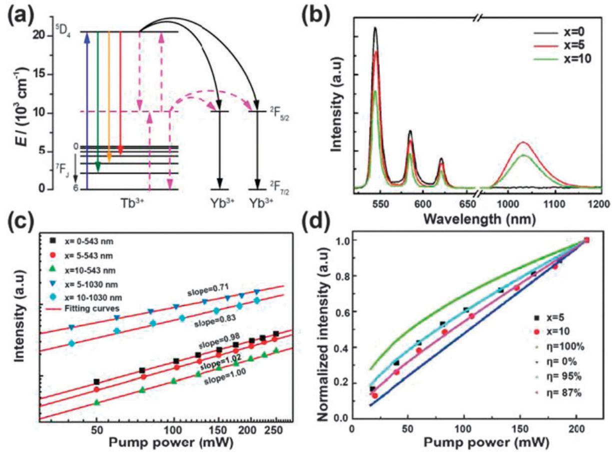

**Fig. 14** (a) Schematic partial energy-level diagram of the $Tb^{3+}$–$Yb^{3+}$ couple, showing the ET mechanism of NIR quantum-cutting under the excitation of the $^7F_6 \rightarrow {}^5D_4$ ($Tb^{3+}$) transition. Black solid lines show the second-order nonlinear quantum-cutting process, whereas the red dotted lines show the linear downconversion process where a virtual energy level located at the middle position (around 10 000 $cm^{-1}$) between the ground state and the $^5D_4$ energy level of $Tb^{3+}$ participates in the quantum-cutting process. (b) Emission spectra of $NaYF_4$:$Tb^{3+}$/$Yb^{3+}$ (1/$x$ mol%, $x$ = 0, 5, and 10) phosphors under 473 nm laser excitation. (c) Double logarithmic plot of $Tb^{3+}$ and $Yb^{3+}$ emission intensity *versus* pump power of the 473 nm laser for $NaYF_4$:$Tb^{3+}$/$Yb^{3+}$ (1/$x$ mol%, $x$ = 0, 5, and 10) phosphors. (d) Experimental and simulated power dependence curves of $Yb^{3+}$ luminescence for $NaYF_4$:$Tb^{3+}$/$Yb^{3+}$ (1/$x$ mol%, $x$ = 0, 5, and 10) phosphors. (Reprinted with permission from ref. 249. Copyright 2012, Optical Society of America.)

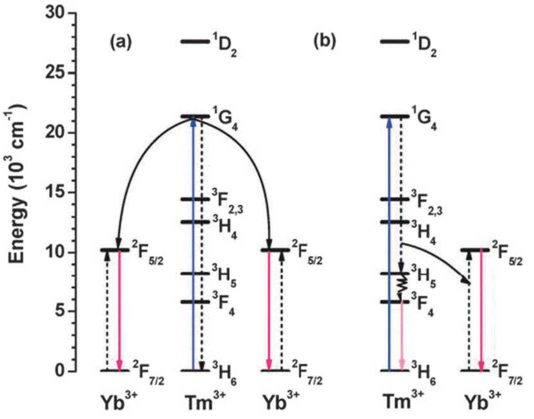

**Fig. 15** Schematic partial energy-level diagrams of $Tm^{3+}$ and $Yb^{3+}$ ions, showing the quantum-cutting mechanisms for the $Tm^{3+}$–$Yb^{3+}$ couple upon blue excitation of $Tm^{3+}$ to the $^1G_4$ state. (a) Quantum-cutting *via* second-order cooperative ET. The excited energy is simultaneously transferred to two $Yb^{3+}$ ions, resulting in two NIR photons of $Yb^{3+}$ ions around 1000 nm. (b) Quantum-cutting *via* first-order phonon-assisted ET. Part of the excited energy is transferred to one $Yb^{3+}$ ion through the phonon-assisted ET process [$Tm^{3+}$ ($^1G_4 \rightarrow {}^3H_5$); $Yb^{3+}$ ($^2F_{7/2} \rightarrow {}^2F_{5/2}$)], which populates the $^3H_5$ ($Tm^{3+}$) state and leads to another mid-IR emission from the $^3F_4$ ($Tm^{3+}$) state at around 1800 nm through fast nonradiative relaxation from $^3H_5$. Note that the energy gap between $^3H_5$ and $^3F_4$ states is about 2250 $cm^{-1}$. Dotted and solid arrows represent nonradiative ET pathways and optical transitions, respectively. (Reprinted with permission from ref. 228. Copyright 2012, Owner Societies.)

power dependence curves were fitted to be between 0.5 and 1 (Fig. 14c and d).[249] This sublinear power dependence phenomenon was attributed to the combination of a linear downconversion process and a dominant second-order nonlinear process.

$Tm^{3+}$–$Yb^{3+}$ COUPLE. The NIR quantum-cutting for the $Tm^{3+}$–$Yb^{3+}$ couple was reported in a variety of host materials, including $GdAl_3(BO_3)_4$,[226] $YPO_4$,[250] glasses,[251–254] glass ceramics,[227,255] and $Y_2O_3$–based transparent ceramics.[256] The mechanism responsible for quantum-cutting in these host materials is generally believed to be a cooperative ET process. In the $Tm^{3+}$–$Yb^{3+}$ couple, NIR quantum-cutting occurs upon excitation at the $^1G_4$ ($Tm^{3+}$) level (~21 000 $cm^{-1}$ or 475 nm). The energy of the $^1G_4 \rightarrow {}^3H_6$ transition of $Tm^{3+}$ is about twice as large as the $^2F_{5/2} \rightarrow {}^2F_{7/2}$ transition of $Yb^{3+}$. Thus, the excited $^1G_4$ (Tm) state can simultaneously transfer its energy to two neighboring $Yb^{3+}$ ions, subsequently resulting in NIR emission in the range of 950–1100 nm (Fig. 15a). Notably, no convincing evidence thus far for the cooperative ET mechanism has been reported. As a result, it is still controversial whether the second-order cooperative or first-order ET dominates the visible-to-NIR quantum-cutting process.

Most recently, Zheng *et al.*[228] in 2012 showed that in $YPO_4$:$Yb^{3+}$/$Tm^{3+}$ phosphors the visible-to-NIR quantum-cutting can be induced by the first-order phonon-assisted ET. In their study, one incident blue photon is cut into one NIR photon of $Yb^{3+}$ ($^2F_{5/2} \rightarrow {}^2F_{7/2}$, ~1000 nm) and one mid-IR photon of $Tm^{3+}$ ($^3F_4 \rightarrow {}^3H_6$, ~1800 nm), rather than two NIR photons from $Yb^{3+}$ (Fig. 15b). Pump power dependence studies on $Yb^{3+}$ emission intensity revealed that only one emitting photon of $Yb^{3+}$ can be achieved per absorbed blue photon. Importantly, such phonon-assisted quantum-cutting luminescence for the $Tm^{3+}$–$Yb^{3+}$ couple can only be realized in those host materials with high phonon energies (such as phosphates, borates, and silicates) because of the large energy mismatch (~2500 $cm^{-1}$) between $^1G_4 \rightarrow {}^3H_5$ ($Tm^{3+}$) and $^2F_{7/2} \rightarrow {}^2F_{5/2}$ ($Yb^{3+}$) transitions. Although $YPO_4$ host material with the maximum phonon energy of about 1070 $cm^{-1}$ meets this requirement, the material is not suitable for c-Si PV application as the mid-IR photon is beyond the absorption edge of the c-Si.

Jaffres *et al.*[257] in 2012 investigated the optical property of $Tm^{3+}$–$Yb^{3+}$ co-doped $La_2BaZnO_5$ phosphors with a maximum phonon energy of ~600 $cm^{-1}$. Upon excitation of $Tm^{3+}$ to the $^1G_4$ level, they found no noticeable ET from $Tm^{3+}$ to $Yb^{3+}$, only cascade emission of three mid-IR photons due to $^3F_4 \rightarrow {}^3H_6$ transition of $Tm^{3+}$. This result is attributed to two successive cross-relaxation steps between $Tm^{3+}$ ions.

$Pr^{3+}$–$Yb^{3+}$ COUPLE. Two ET mechanisms have been proposed for quantum-cutting in the $Pr^{3+}$–$Yb^{3+}$ couple: (i) second-order cooperative ET from one $Pr^{3+}$ ion to two different $Yb^{3+}$ ions because the $^3P_0 \rightarrow {}^3H_4$ transition of $Pr^{3+}$ (~20 700 $cm^{-1}$) is about twice the energy of the $^2F_{5/2} \rightarrow {}^2F_{7/2}$ transition of $Yb^{3+}$;[226,229,258–261] or (ii) first-order resonant ET *via* two sequential steps involving cross-relaxation [$Pr^{3+}$ ($^3P_0 \rightarrow {}^1G_4$); $Yb^{3+}$ ($^2F_{7/2} \rightarrow {}^2F_{5/2}$)] followed by a second ET process [$Pr^{3+}$ ($^1G_4 \rightarrow {}^3H_4$); $Yb^{3+}$ ($^2F_{7/2} \rightarrow {}^2F_{5/2}$)] (Fig. 16a).[230,262–273]

Meijerink and co-workers[263] argued that the dominant quantum-cutting mechanism in the $Pr^{3+}$–$Yb^{3+}$ couple appears to be first-order ET by cross relaxation, because the reduced

Published on 16 October 2012. Downloaded on 11/09/2014 14:42:06.

cross-relaxation rate can be compensated by the much higher (∼1000 times) probability of first-order ET relative to the second-order cooperative ET process. This first-order ET scheme leads to efficient quantum-cutting of one 441 nm blue photon into two 980 nm NIR photons in $SrF_2$:$Pr^{3+}$,$Yb^{3+}$ phosphors.[230] Comparison of emission spectra for $SrF_2$:$Pr^{3+}$ (0.1 mol%) and $SrF_2$:$Pr^{3+}$,$Yb^{3+}$ (0.1/5%) samples (Fig. 16b) revealed an actual conversion efficiency of 140%. Furthermore, the 980 nm photon flux upon excitation of $Pr^{3+}$ to the $^3P_J$,$^1I_6$ ($J$ = 0, 1, and 2) levels is approximately twice that of the absorption strength of the $^3P_J$,$^1I_6$ levels (Fig. 16c), confirming that for every photon absorbed to the $^3P_J$,$^1I_6$ levels, two photons in the NIR were generated. Introduction of $Yb^{3+}$ into $SrF_2$:$Pr^{3+}$ induced faster and nonexponential decay of $^3P_0 \rightarrow {}^3H_4$ emission (Fig. 16d), thus providing additional evidence for the ET from $Pr^{3+}$ to nearby $Yb^{3+}$ ions.

$Er^{3+}$–$Yb^{3+}$ COUPLE. The combination of $Er^{3+}$ and $Yb^{3+}$, well-known for upconversion research, can also give rise to efficient visible-to-NIR quantum-cutting.[232] The $Er^{3+}$ ion has excited states at ∼20 000 $cm^{-1}$ ($^4F_{7/2}$) and 10 000 $cm^{-1}$ ($^4I_{11/2}$) that allow for a two-step ET process, raising two neighboring $Yb^{3+}$ ions to the $^2F_{5/2}$ excited state around 10 000 $cm^{-1}$. Upon 490 nm excitation at the $^4F_{7/2}$ level, the cross-relaxation process of [$Er^{3+}$ ($^4F_{7/2} \rightarrow {}^4I_{11/2}$); $Yb^{3+}$ ($^2F_{7/2} \rightarrow {}^2F_{5/2}$)] can occur, followed by a second ET step of [$Er^{3+}$ ($^4I_{11/2} \rightarrow {}^4I_{15/2}$); $Yb^{3+}$ ($^2F_{7/2} \rightarrow {}^2F_{5/2}$)]. Both $Yb^{3+}$ ions then emit a NIR photon of ∼1000 nm that can be absorbed by a c-Si solar cell (Fig. 17a).

Meijerink *et al.*[232] have demonstrated that the use of the $Er^{3+}$–$Yb^{3+}$ couple in $Cs_3Y_2Br_9$ phosphors can lead to achieving efficient visible-to-NIR quantum-cutting with an internal quantum efficiency of 195%. Despite the relatively narrow energy gap (∼1250 $cm^{-1}$) between the $^4F_{7/2}$ level and the next lower $^2H_{11/2}$ level for $Er^{3+}$, the low phonon energy (∼180 $cm^{-1}$) of the bromide host results in a long-lived $^4F_{7/2}$ state. This is attributed to slow-rate multiphonon relaxation when the energy gap exceeds five phonons. However, visible-to-NIR quantum-cutting from the $^4F_{7/2}$ level for the $Er^{3+}$–$Yb^{3+}$ couple was found to be very inefficient in fluoride ($NaYF_4$, maximum phonon energy ∼400 $cm^{-1}$) and chloride ($KPb_2Cl_5$, maximum phonon energy ∼200 $cm^{-1}$) host materials. A feasible explanation for this optical phenomenon is that multiphonon relaxation from the $^4F_{7/2}$ to $^2H_{11/2}$ and $^4S_{3/2}$ levels is faster than cross-relaxation with a neighboring $Yb^{3+}$.[231,274] Efficient ultraviolet-to-NIR quantum-cutting from the $^4G_{11/2}$ ($Er^{3+}$) level was observed for the $Er^{3+}$–$Yb^{3+}$ couple in $NaYF_4$ and $YF_3$ phosphors, resulting in one NIR photon from the $Yb^{3+}$ ion ($^2F_{5/2} \rightarrow {}^2F_{7/2}$, 980 nm) and one red photon from the $Er^{3+}$ ion ($^4F_{9/2} \rightarrow {}^4I_{15/2}$, 650 nm) after absorption of a single ultraviolet photon with a wavelength less than 380 nm.[231,275]

$Nd^{3+}$–$Yb^{3+}$ COUPLE. Close inspection of the energy levels of the $Nd^{3+}$–$Yb^{3+}$ couple shows that NIR quantum-cutting from the $^2G_{9/2}$ ($Nd^{3+}$) level (∼21 000 $cm^{-1}$ or 470 nm) *via* the cross-relaxation process of [$Nd^{3+}$ ($^2G_{9/2} \rightarrow {}^4F_{3/2}$); $Yb^{3+}$ ($^2F_{7/2} \rightarrow {}^2F_{5/2}$)], followed by a second ET step from the $^4F_{3/2}$ ($Nd^{3+}$) level (∼11 547 $cm^{-1}$ or 866 nm) to the $^2F_{5/2}$ ($Yb^{3+}$) level (∼10 000 $cm^{-1}$ or 1000 nm), could lead to emission of two NIR photons from $Yb^{3+}$ ions (Fig. 17b).[233,276] However, fast multiphonon relaxation from the $^2G_{9/2}$ to lower $^4G_{7/2}$ ($Nd^{3+}$) level was observed in the $YF_3$ host, preventing efficient quantum-cutting from the $^2G_{9/2}$ level.[233]

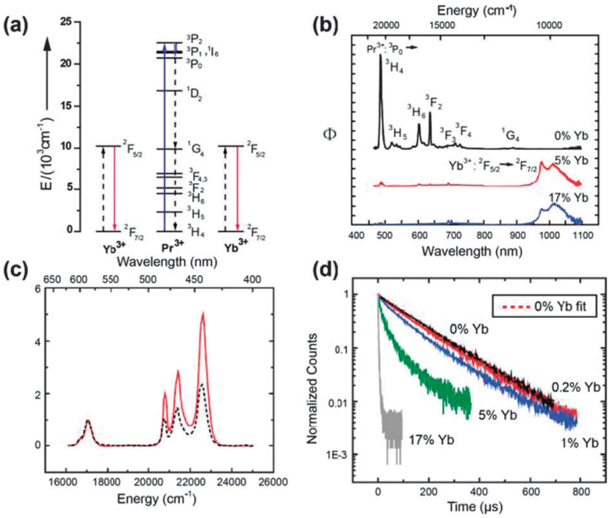

**Fig. 16** (a) NIR quantum-cutting *via* the first-order ET mechanism for the $Pr^{3+}$–$Yb^{3+}$ couple. A two-step ET occurs upon excitation onto the $^3P_J$ ($J$ = 0, 1, 2) and $^1I_6$ levels of $Pr^{3+}$, using the $^1G_4$ level as an intermediate state. A single blue photon absorbed by these levels is converted into two NIR photons of ∼1000 nm. (b) Emission spectra for $SrF_2$:$Pr^{3+}$/$Yb^{3+}$ (0.1/$x$ mol%; $x$ = 0, 5, and 17) under excitation at 441 nm. (c) Diffuse reflectance (dashed line) and excitation spectra (solid line) of the $SrF_2$:Pr/Yb (0.1/5 mol%) sample. (d) Luminescence decay curves of the $^3P_0 \rightarrow {}^3H_4$ emission at 486 nm in $SrF_2$:Pr/Yb (0.1/$x$ mol%; $x$ = 0, 0.2, 1, 5, and 17) under excitation at 441 nm. (Reprinted with permission from ref. 230. Copyright 2009, Wiley-VCH Verlag GmbH & Co. KGaA.)

The energy difference between the $^2G_{9/2}$ and $^4G_{7/2}$ ($Nd^{3+}$) levels is only 1012 $cm^{-1}$ and thus multiphonon relaxation dominates in the $YF_3$ host material where the maximum phonon energy is about 500 $cm^{-1}$. The multiphonon relaxation from the $^2G_{9/2}$ level to lower-energy levels results in population of the $^4F_{3/2}$ ($Nd^{3+}$) level, from which efficient one-step ET to $Yb^{3+}$ occurs through dipole–dipole interaction. This may explain the reason for realizing efficient NIR quantum-cutting for the $Nd^{3+}$–$Yb^{3+}$ couple in a host lattice with much lower phonon energy (*e.g.*, bromides or chlorides) ions. By comparison, ultraviolet-to-NIR quantum-cutting was observed from the higher energy $^4D_{3/2}$ ($Nd^{3+}$) level (∼28 000 $cm^{-1}$ or 360 nm) in $YF_3$:$Nd^{3+}$/$Yb^{3+}$ phosphors with an internal quantum efficiency of 140%.[233]

$Ho^{3+}$–$Yb^{3+}$ COUPLE. The $^5F_3 \rightarrow {}^5I_8$ transition of $Ho^{3+}$ is approximately twice the energy required for the $^2F_{5/2} \rightarrow {}^2F_{7/2}$ transition of $Yb^{3+}$. However, the second-order cooperative quantum-cutting process of [$Ho^{3+}$ ($^5F_3 \rightarrow {}^5I_8$); 2$Yb^{3+}$ ($^2F_{7/2} \rightarrow {}^2F_{5/2}$)] is unlikely because the $^5F_3$ ($Ho^{3+}$) excited state can decay rapidly to the next $^5S_2$,$^5F_4$ states.[277] Lin and co-workers[234] first reported the first-order quantum-cutting luminescence for the $Ho^{3+}$–$Yb^{3+}$ couple in glass ceramics with an internal quantum efficiency of 159%. Under 488 nm blue-light excitation, $Ho^{3+}$ could be excited to the $^5F_3$ state followed by nonradiative relaxation to $^5S_2$,$^5F_4$ states, from which the resonant cross-relaxation ET of [$Ho^{3+}$ ($^5S_2$,$^5F_4 \rightarrow {}^5I_6$); $Yb^{3+}$ ($^2F_{7/2} \rightarrow {}^2F_{5/2}$)] occurs. This leads to

Published on 16 October 2012. Downloaded on 11/09/2014 14:42:06.

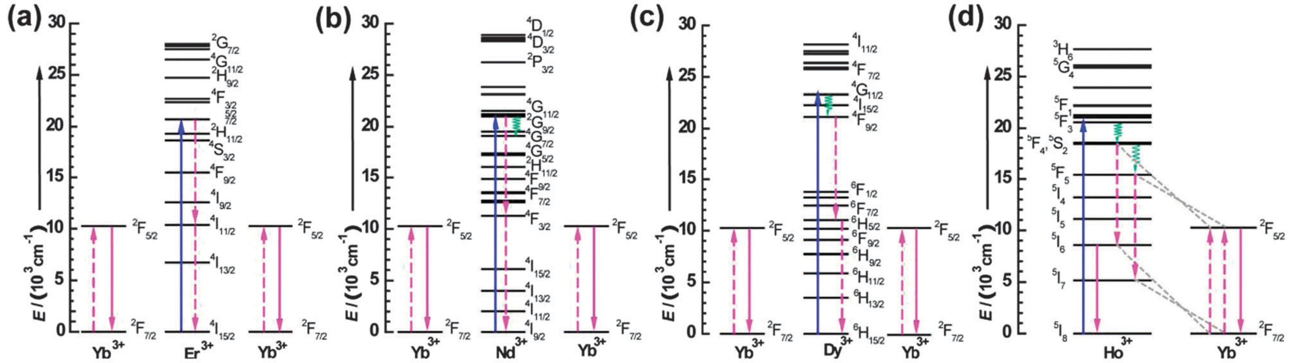

**Fig. 17** (a) Schematic partial energy-level diagrams for the $Er^{3+}$–$Yb^{3+}$ couple showing the quantum-cutting mechanism starting from the $^4F_{7/2}$ level. A single blue photon absorbed by $Er^{3+}$ is converted into two ~1000 nm NIR photons of $Yb^{3+}$ *via* two sequential ET steps: (1) cross-relaxation ET of [$Er^{3+}$ ($^4F_{7/2} \rightarrow {}^4I_{11/2}$); $Yb^{3+}$ ($^2F_{7/2} \rightarrow {}^2F_{5/2}$)]; (2) cross-relaxation ET of [$Er^{3+}$ ($^4I_{11/2} \rightarrow {}^4I_{15/2}$); $Yb^{3+}$ ($^2F_{7/2} \rightarrow {}^2F_{5/2}$)]. (b) Schematic partial energy-level diagrams for the $Nd^{3+}$–$Yb^{3+}$ couple showing the quantum-cutting mechanism starting from the $^2G_{9/2}$ level. A single blue photon absorbed by $Nd^{3+}$ is downconverted into two ~1000 nm NIR photons of $Yb^{3+}$ ions *via* two-step ET mechanisms: (1) cross-relaxation ET of [$Nd^{3+}$ ($^2G_{9/2} \rightarrow {}^4F_{3/2}$); $Yb^{3+}$ ($^2F_{7/2} \rightarrow {}^2F_{5/2}$)]; (2) cross-relaxation ET of [$Nd^{3+}$ ($^4F_{3/2} \rightarrow {}^4I_{9/2}$); $Yb^{3+}$ ($^2F_{7/2} \rightarrow {}^2F_{5/2}$)]. (c) Schematic partial energy-level diagrams for the $Er^{3+}$–$Yb^{3+}$ couple showing the quantum-cutting mechanism starting from the $^4F_{9/2}$ level. One blue photon absorbed by $Dy^{3+}$ is downconverted into two NIR photons from $Yb^{3+}$ through two sequential ET steps: (1) cross-relaxation ET of [$Dy^{3+}$ ($^4F_{9/2} \rightarrow {}^6H_{5/2}$); $Yb^{3+}$ ($^2F_{7/2} \rightarrow {}^2F_{5/2}$)]; (2) cross-relaxation ET of [$Dy^{3+}$ ($^6H_{5/2} \rightarrow {}^6H_{15/2}$); $Yb^{3+}$ ($^2F_{7/2} \rightarrow {}^2F_{5/2}$)]. (d) Schematic partial energy-level diagrams for the $Ho^{3+}$–$Yb^{3+}$ couple showing the quantum-cutting mechanism starting from the $^5S_2$,$^5F_4$ level. Note that the $^5F_3$ level of $Ho^{3+}$ is located at ~20 600 cm$^{-1}$, while the $^5S_2$,$^5F_4$ level is located at ~18 600 cm$^{-1}$.

NIR quantum-cutting involving the emission of one 1180 nm photon ($^5I_6 \rightarrow {}^5I_8$ transition of $Ho^{3+}$) and one 980 nm photon ($^2F_{5/2} \rightarrow {}^2F_{7/2}$ transition of $Yb^{3+}$) (Fig. 17d). In addition, some of the electrons in $^5S_2$,$^5F_4$ states of $Ho^{3+}$ could further relax non-radiatively to the lower $^5F_5$ level, which induces another resonant cross-relaxation process of [$Ho^{3+}$ ($^5F_5 \rightarrow {}^5I_7$); $Yb^{3+}$ ($^2F_{7/2} \rightarrow {}^2F_{5/2}$)], and results in the intensity enhancement of $Yb^{3+}$ emission.[234]

The first-order NIR quantum-cutting for the $Ho^{3+}$–$Yb^{3+}$ couple was later confirmed by Yu and co-workers in $NaYF_4$ phosphors.[235] However, Deng *et al.*[236] proposed a different ET mechanism in these phosphors under ultraviolet (359 nm) excitation. They argued that the NIR quantum-cutting occurs at the $^5G_4$ level, which involves two-step sequential cross-relaxation: [$Ho^{3+}$ ($^5G_4 \rightarrow {}^5F_5$); $Yb^{3+}$ ($^2F_{7/2} \rightarrow {}^2F_{5/2}$)] followed by [$Ho^{3+}$ ($^5F_5 \rightarrow {}^5I_7$); $Yb^{3+}$ ($^2F_{7/2} \rightarrow {}^2F_{5/2}$)]. Thus, one ultraviolet photon absorbed by $Ho^{3+}$ gave rise to two NIR photons of $Yb^{3+}$, with a maximum quantum efficiency of 155.2%.[236]

$Dy^{3+}$–$Yb^{3+}$ COUPLE. NIR quantum-cutting through the $Dy^{3+}$–$Yb^{3+}$ couple has been investigated to a lesser extent. Bai *et al.*[237] in 2011 demonstrated that under 430 nm blue-light excitation, NIR quantum-cutting could be achieved in $Dy^{3+}$/$Yb^{3+}$ co-doped zeolites through a two-step ET process from the $^4F_{9/2}$ ($Dy^{3+}$) level to two neighboring $Yb^{3+}$ ions: cross-relaxation ET of [$Dy^{3+}$ ($^4F_{9/2} \rightarrow {}^6H_{5/2}$); $Yb^{3+}$ ($^2F_{7/2} \rightarrow {}^2F_{5/2}$)] followed by another cross-relaxation ET of [$Dy^{3+}$ ($^6H_{5/2} \rightarrow {}^6H_{15/2}$); $Yb^{3+}$ ($^2F_{7/2} \rightarrow {}^2F_{5/2}$)] (Fig. 17c). Note that the $^4F_{9/2}$ ($Dy^{3+}$) level is located at ~21 000 cm$^{-1}$, while the $^6H_{5/2}$ ($Dy^{3+}$) level is situated at ~10 000 cm$^{-1}$. Therefore, the energy of the $^4F_{9/2} \rightarrow {}^6H_{15/2}$ transition of $Dy^{3+}$ is about twice as much as that of the $^2F_{7/2} \rightarrow {}^2F_{5/2}$ transition of $Yb^{3+}$. The $^6H_{5/2}$ ($Dy^{3+}$) level serves as the intermediate level between $^4F_{9/2}$ and $^6H_{15/2}$. The ET efficiency from the $^4F_{9/2}$ level was estimated to be 42%, and the intrinsic luminescence quantum efficiency of $Yb^{3+}$ emission reached 54%.

$Ho^{3+}$ SINGLE ION. Yu and co-workers in 2011 reported NIR quantum-cutting in $Ho^{3+}$-doped $NaYF_4$ phosphors.[238,239] It is of interest to note that the quantum-cutting through $Ho^{3+}$ depends on the excitation wavelength. Under 300–500 nm excitation, the $NaYF_4$:$Ho^{3+}$ phosphors gave rise to two NIR photons with a sequential two-step process: $^5S_2$,$^5F_4 \rightarrow {}^5I_6$ transition (1015 nm) followed by $^5I_6 \rightarrow {}^5I_8$ transition (1180 nm).[239] The $^5I_6$ acts as an intermediate level. In contrast, upon 287 nm excitation of $Ho^{3+}$ to the $^3G_3$,$^3L_8$ level, cascade emissions of three NIR photons occur: $^3D_3 \rightarrow {}^3K_8$,$^5F_2$, 850 nm; $^5S_2$,$^5F_4 \rightarrow {}^5I_6$, 1015 nm; $^5I_6 \rightarrow {}^5I_8$ transition, 1180 nm.[238] The electronic states of $^3K_8$,$^5F_2$, and $^5I_6$ in $Ho^{3+}$ act as intermediate levels. The occurrence of the NIR quantum-cutting in the $NaYF_4$:$Ho^{3+}$ phosphors was confirmed by time-resolved emission spectra as well as distinct emission spectra recorded at different excitation wavelengths. The quantum efficiency calculated using the Judd–Ofelt theory was about 124%.[238] This low internal quantum efficiency might result from the loss of a substantial amount of light in the ultraviolet/visible spectral region, thereby preventing their practical application in solar cells. Quantum-cutting *via* photon cascade emission was also reported in $YVO_4$:$Ho^{3+}$ phosphors and $LaF_3$:$Ho^{3+}$ nanocrystals.[243,278]

### 4.3 Broadband quantum-cutting for c-Si solar cells

Ideal NIR quantum-cutting materials for c-Si solar cells should be able to downconvert the ultraviolet–green (300–550 nm) part of the solar spectrum to ~1000 nm photons. Despite their usefulness, the quantum-cutting materials based on $Ln^{3+}$–$Yb^{3+}$ (Ln = Tb, Tm, Pr, Er, Nd, Ho, and Dy) couples are still far from practical application because of low excitation efficiency. A main limiting factor for the conversion efficiency is the low absorption cross-section (typically on the order of $10^{-21}$ cm$^2$) of the lanthanide ions arising from the parity-forbidden 4f–4f transitions.[279] In contrast, the dipole-allowed 4f–5d transitions have much higher absorption cross-sections of up to $10^{-18}$ cm$^2$.[279] Recently, much attention has been paid to broadband NIR quantum-cutting through use of $Ce^{3+}$, $Eu^{2+}$ and $Yb^{2+}$ with

Published on 16 October 2012. Downloaded on 11/09/2014 14:42:06.

strong absorption intensity in the ultraviolet–blue spectral region as energy donors for Yb$^{3+}$ (Table 4).[279–293] The Bi$^{3+}$ ion was also shown to be an efficient sensitizer for Yb$^{3+}$.[294–298] A significant parallel development for efficient emission of Yb$^{3+}$ is to utilize host sensitization through direct cooperative ET from the host to Yb$^{3+}$.[299–302]

Ce$^{3+}$–Yb$^{3+}$ couple. The Ce$^{3+}$ ion could serve as an ideal broadband sensitizer for Yb$^{3+}$, because its 4f–5d transition covers a broad spectral range and, more importantly, the energy of its 4f–5d transition can be tuned by changing the crystal field strength as well as the covalency of the host. The NIR quantum-cutting for the Ce$^{3+}$–Yb$^{3+}$ couple has been reported for many host materials, and the cooperative ET [Ce$^{3+}$ (5d → 4f); 2Yb$^{3+}$ ($^2F_{7/2} \rightarrow {}^2F_{5/2}$)] appears to be the dominant relaxation route to achieve the NIR emission of Yb$^{3+}$.[279–284,303,304] When compared to the most common Ln$^{3+}$–Yb$^{3+}$ (Ln = Tb, Tm, and Pr) couples, the Ce$^{3+}$–Yb$^{3+}$ couple could harvest a broad solar spectral range to give rise to intense NIR emissions. This result can be ascribed to the large absorption cross-section of Ce$^{3+}$ acting as the energy donor (Fig. 18). However, some researchers believe that the ET from Ce$^{3+}$ to Yb$^{3+}$ is possibly due to metal-to-metal charge transfer through the facile redox reaction of Ce$^{3+}$+Yb$^{3+}$ → Ce$^{4+}$+Yb$^{2+}$.[305–307] This charge transfer may complicate the quantum-cutting process.

Several groups also used the Ce$^{3+}$ ion to sensitize the Tb$^{3+}$–Yb$^{3+}$ quantum-cutting process.[285–287] A possible indirect ET mechanism was proposed for the Ce$^{3+}$–Tb$^{3+}$–Yb$^{3+}$ quantum-cutting system. First, the Ce$^{3+}$ ion directly absorbs an ultraviolet photon *via* allowed 4f–5d transitions. Subsequently, the excitation energy in the lowest 5d (Ce$^{3+}$) excited level relaxes to the $^5D_3$ and $^5D_4$ (Tb$^{3+}$) levels *via* phonon assistance. From the $^5D_4$ level, the energy of the excited Tb$^{3+}$ ion is simultaneously transferred to two different Yb$^{3+}$ ions. The NIR emission of Yb$^{3+}$ in the Ce$^{3+}$–Tb$^{3+}$–Yb$^{3+}$ system can be enhanced by about 10 times as compared to that obtained with the Tb$^{3+}$–Yb$^{3+}$ couple. Nonetheless, the quantum-cutting mechanism in this triply doped system remains elusive. Further experimentation is clearly needed. Another interesting development of quantum-cutting is the work on sensitization of the Pr$^{3+}$–Yb$^{3+}$ couple using Ce$^{3+}$ ions.[308]

Eu$^{2+}$–Yb$^{3+}$ couple. The first example of NIR quantum-cutting using Eu$^{2+}$ and Yb$^{3+}$ was reported by Qiu *et al.* in glasses and $CaAl_2O_4$ phosphors.[288–290] Eu$^{2+}$ shows a broad excitation spectrum in the 250–400 nm ultraviolet region due to $4f^7 \rightarrow 4f^65d$ transition. The energy of the $4f^65d \rightarrow 4f^7$ (Eu$^{2+}$) transition is approximately twice as much of the $^2F_{5/2} \rightarrow {}^2F_{7/2}$ (Yb$^{3+}$) transition. Therefore, cooperative ET from one Eu$^{2+}$ ion to two Yb$^{3+}$ ions was proposed by these authors to be the dominant relaxation process, and the calculated maximum quantum efficiency approached 200%. Subsequently, several other groups also reported broadband quantum-cutting *via* the Eu$^{2+}$–Yb$^{3+}$ couple in glass ceramics and silicate glasses.[291,292]

Yb$^{2+}$–Yb$^{3+}$ couple. Similar to Eu$^{2+}$ and Ce$^{3+}$, Yb$^{2+}$ commonly exhibits 4f–5d broadband luminescence.[309] The optical feature of Yb$^{2+}$ originates from $4f^{14} \leftrightarrow 4f^{13}5d$ transitions. Teng and co-workers recently reported the efficient broadband quantum-cutting in Yb$^{2+}$–Yb$^{3+}$ co-doped $CaAl_2O_4$ phosphors prepared under a reducing atmosphere.[290] The $CaAl_2O_4$ crystal has tridymite structure, which consists of $AlO_4$-tetrahedra. Both Yb$^{2+}$ and Yb$^{3+}$ ions substitute the Ca$^{2+}$ site in the $CaAl_2O_4$ crystal because of their similar ionic radius (0.099 nm for both Ca$^{2+}$ and Yb$^{3+}$, and 0.102 nm for Yb$^{2+}$, while 0.051 nm for Al$^{3+}$). After a direct ultraviolet excitation (250–400 nm) of Yb$^{2+}$ ions, the authors observed intense Yb$^{3+}$ NIR emission. The

**Table 4** Selected broadband NIR quantum-cutting materials for c-Si solar cells

| Dopant ion | Host lattice | Preparation method | Excitation (nm) | Maximum quantum efficiency (%) | Ref. |
|---|---|---|---|---|---|
| Ce$^{3+}$–Yb$^{3+}$ | Borate glasses | Glass melting | 250–380 | 174 | 279 |
| Ce$^{3+}$–Yb$^{3+}$ | $YBO_3$ | Solid-state reaction | 326–377 | 175 | 280 |
| Ce$^{3+}$–Yb$^{3+}$ | $LuBO_3$ | Hydrothermal method | 325–375 | 181 | 281 |
| Ce$^{3+}$–Yb$^{3+}$ | $Y_3Al_5O_{12}$ | Sol–gel | 400–500 | 153 | 282 |
| Ce$^{3+}$–Yb$^{3+}$ | $Y_3Al_5O_{12}$ transparent ceramics | Solid-state reaction | 400–500 | 175 | 283 |
| Ce$^{3+}$–Yb$^{3+}$ | $Y_2SiO_5$ | Combustion synthesis | 355 | 160 | 284 |
| Ce$^{3+}$–Tb$^{3+}$–Yb$^{3+}$ | $GdBO_3$ | Combustion synthesis | 300–400 | — | 285 |
| Ce$^{3+}$–Tb$^{3+}$–Yb$^{3+}$ | $Ca_2BO_3Cl$ | Solid-state reaction | 300–380 | — | 286 |
| Ce$^{3+}$–Tb$^{3+}$–Yb$^{3+}$ | Borate glasses | Glass melting | 250–350 | — | 287 |
| Eu$^{2+}$–Yb$^{3+}$ | Borate glasses | Glass melting | 250–400 | 164 | 288 |
| Eu$^{2+}$–Yb$^{3+}$ | Aluminosilicate glasses | Glass melting | 250–500 | 127 | 289 |
| Eu$^{2+}$–Yb$^{3+}$ | $CaAl_2O_4$ | Solid-state reaction | 250–450 | 155 | 290 |
| Eu$^{2+}$–Yb$^{3+}$ | Glass ceramics containing $CaF_2$ nanocrystals | Glass melting | 230–390 | 151 | 291 |
| Eu$^{2+}$–Yb$^{3+}$ | Silicate glasses | Glass melting | 250–400 | 134 | 292 |
| Yb$^{2+}$–Yb$^{3+}$ | $CaAl_2O_4$ | Solid-state reaction | 250–400 | — | 293 |
| Bi$^{3+}$–Yb$^{3+}$ | $Gd_2O_3$ | Combustion synthesis | 300–400 | 173 | 294 |
| Bi$^{3+}$–Yb$^{3+}$ | $Y_2O_3$ | Combustion synthesis | 300–400 | 173 | 295 |
| Bi$^{3+}$–Yb$^{3+}$ | $Y_2O_3$ thin-films | Pulsed laser deposition | 300–400 | 152 | 296 |
| Bi$^{3+}$–Yb$^{3+}$ | $YVO_4$ | Solid-state reaction | 250–400 | 187 | 297 |
| Bi$^{3+}$–Yb$^{3+}$ | $YNbO_4$ | Solid-state reaction | 250–350 | 180 | 298 |
| Yb$^{3+}$ | $YVO_4$ | Solid-state reaction | 200–350 | 185 | 299 |
| Yb$^{3+}$ | $SiO_2$–$YVO_4$ thin-films | Sol–gel | 200–350 | — | 300 |
| Yb$^{3+}$ | $YVO_4$ thin-films | Pulsed laser deposition | 200–350 | 128 | 301 |
| Li$^{+}$–Yb$^{3+}$ | ZnO | Thermal growth | 300–420 | — | 302 |

Published on 16 October 2012. Downloaded on 11/09/2014 14:42:06.

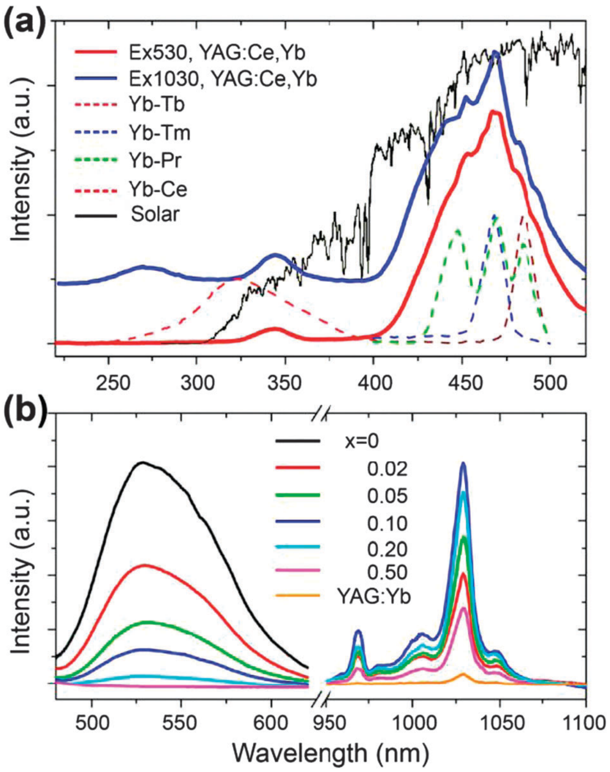

**Fig. 18** (a) Representative excitation spectra for YAG:$Ce^{3+}$,$Yb^{3+}$ ($Y_{2.91-3x}Ce_{0.09}Yb_{3x}Al_5O_{12}$, $x = 0.1$) monitoring the emission of $Ce^{3+}$ at 530 nm, and the emission of $Yb^{3+}$ at 1030 nm, respectively. For comparison, the excitation spectra of $Yb^{3+}$ of quantum-cutting materials activated with ion pairs of $Yb^{3+}$–$Ln^{3+}$ (Ln = Tb, Tm, and Pr; the host is a borogermanate glass) and $Yb^{3+}$–$Ce^{3+}$ (the host is a borate glass) are also given. The AM 1.5G solar spectrum in this spectral region is shown in the background as a reference. (b) Concentration-dependent emission spectra of YAG:$Ce^{3+}$,$Yb^{3+}$ ($x$ = 0–0.5) and YAG:$Yb^{3+}$ ($Y_{2.7}Yb_{0.3}Al_5O_{12}$) under the excitation at 470 nm. (Reprinted with permission from ref. 282. Copyright 2009, Optical Society of America.)

dependence of $Yb^{3+}$ luminescence intensity on the excitation power exhibited a sublinear relationship with a slope of 0.43. On the basis of these results, a three-photon or phonon-assisted two-photon quantum-cutting process involving cooperative ET from $Yb^{2+}$ to $Yb^{3+}$ ions was proposed to be the main mechanism.

$Bi^{3+}$–$Yb^{3+}$ COUPLE. $Bi^{3+}$ with the $6s^2$ electronic configuration has been extensively investigated as both the activator and sensitizer for luminescent materials.[310,311] The $^3P_1$ and $^1P_1$ levels of $Bi^{3+}$ are mixed by spin–orbit coupling, and as a consequence, $^1S_0 \rightarrow {}^3P_1$ and $^1S_0 \rightarrow {}^1P_1$ transitions have reasonable absorption strength. Two research groups recently demonstrated efficient NIR quantum-cutting in $Bi^{3+}$–$Yb^{3+}$ co-doped $Ln_2O_3$ (Ln = Gd, Y) phosphors and thin-films.[294–296,312] $Ln_2O_3$ (Ln = Gd, Y) host lattices have excellent chemical durability and thermal stability, as well as low phonon energy (maximum phonon energy, ~600 $cm^{-1}$).[313–315] In these hosts, $Bi^{3+}$ exhibits strong absorption in the ultraviolet region of 300–400 nm through the allowed $^1S_0 \rightarrow {}^3P_1$ transition. After a direct excitation of $Bi^{3+}$, an intense NIR emission band centered at 977 nm from $Yb^{3+}$ was recorded. It was also demonstrated that the charge-transfer between $O^{2-}$ and $Yb^{3+}$ did not have any influence on $Bi^{3+}$ and $Yb^{3+}$ emission. Decay lifetime measurements for $Bi^{3+}$ emission further evidenced the occurrence of cooperative ET from $Bi^{3+}$ to $Yb^{3+}$ ions, and a maximum quantum efficiency close to 200% was calculated. The NIR quantum-cutting of the $Bi^{3+}$–$Yb^{3+}$ couple was also recently reported in $YVO_4$ and $YNbO_4$ phosphors.[297,298]

HOST–$YB^{3+}$ COMBINATION. Broadband quantum-cutting luminescence was also realized using the combination of host and $Yb^{3+}$ ions.[299–301] Wei and co-workers recently reported NIR quantum-cutting in $YVO_4$:$Yb^{3+}$ phosphors.[299] Cooperative ET from the excited $VO_4^{3-}$ group to two neighboring $Yb^{3+}$ ions resulted in the conversion of 250–350 nm light into NIR emission around 980 nm. The calculated maximum quantum efficiency reached as high as 185.7%.[299] However, this estimated value must be interpreted in the context of the following considerations: (i) concentration quenching effect of $Yb^{3+}$; (ii) direct ET from the excited $VO_4^{3-}$ group to the charge transfer state of $O^{2-}$–$Yb^{3+}$; and (iii) the quenching effect caused by the direct ET from $VO_4^{3-}$ group to quenching centers. For practical applications in c-Si solar cells, these effects have to be significantly minimized to ensure enhanced emission of $Yb^{3+}$.

In a following paper by Shestakov *et al.*, $Li^+$–$Yb^{3+}$ co-doped ZnO nanocrystals were tested for NIR quantum-cutting.[302] ZnO is a direct wide gap semiconductor with large absorption cross-section in the 250–400 nm ultraviolet wavelength range and high transparency in the visible and NIR ranges. Upon ultraviolet excitation, the authors observed two broadband emissions centered at 770 and 1000 nm, which can be ascribed to $Li^+$–$Li^+$ and $Yb^{3+}$–$Li^+$ dimer dopants, respectively. Pump power dependence and temperature dependence of these emission bands indicated that the ET from the ZnO host to $Li^+$–$Li^+$ and $Yb^{3+}$–$Li^+$ dimers was responsible for the quantum-cutting mechanism.

### 4.4 Quantum-cutting for germanium solar cells

The energy of the $^4I_{13/2} \rightarrow {}^4I_{15/2}$ transition of $Er^{3+}$ around 1540 nm is slightly larger than the bandgap of germanium (0.67 eV; 1850 nm). To this end, the NIR quantum-cutting of $Er^{3+}$ has potential to improve the efficiency of germanium-based solar cells. Chen *et al.* in 2009 reported three-photon NIR quantum-cutting of $Er^{3+}$ in the $GdVO_4$ crystal.[240] Upon 523 nm excitation of $Er^{3+}$ to the $^2H_{11/2}$ level, they observed a characteristic NIR emission at 1532 nm due to $^4I_{13/2} \rightarrow {}^4I_{15/2}$ transition, with a quantum efficiency of about 178%. The principal drawback of this system is the low effective absorption cross-section of $Er^{3+}$ at 300–550 nm. To solve this problem, Zhou *et al.*[316,317] in 2010 demonstrated that the incorporation of $Ce^{3+}$ and $Eu^{2+}$ in YAG:$Ce^{3+}$/$Er^{3+}$ and $Ca_8Mg(SiO_4)_4Cl_2$:$Eu^{2+}$/$Er^{3+}$ phosphors results in strong erbium sensitization, leading to significantly increased NIR emission intensity of $Er^{3+}$.

Subsequently, two research groups independently reported a novel quantum-cutting mechanism based on resonant ET from $Er^{3+}$ to $Yb^{3+}$ in $Er^{3+}$/$Yb^{3+}$ co-doped glass ceramics and $NaYF_4$ nanocrystals, respectively.[318,319] In these systems, a photon, absorbed by $Er^{3+}$ in the wavelength range of 350–550 nm, was converted into two photons of 650–1550 nm that can be

Published on 16 October 2012. Downloaded on 11/09/2014 14:42:06.

subsequently emitted by $Er^{3+}$ and $Yb^{3+}$, with the maximum quantum efficiency approaching 200%.

### 4.5 Multiple exciton generation in quantum dots

Different from the above-mentioned quantum-cutting in lanthanide ions, another viable approach to significantly enhance solar energy conversion is to utilize multiple exciton generation (MEG, also termed carrier multiplication) in QDs, whereby the absorption of one photon bearing at least twice the bandgap energy can produce two or more electron–hole pairs (Fig. 19a).[320–322] This approach enables effective harvesting of high-energy photons in the violet and ultraviolet parts of the solar spectrum that are normally lost as waste heat.[323] Thus, the application of MEG in third-generation PV cells has the potential to achieve maximum efficiency as high as 44%, well exceeding the Shockley–Queisser limit of 31% for single-junction solar cells.[324] Since its first discovery in PbSe nanocrystals by Schaller and Klimov in 2004,[325] the MEG effect has been experimentally observed in many QD systems, such as PbS, PbTe, CdSe, and Si,[326] as well as recently in single-walled carbon nanotubes.[327,328] Several recent reviews have discussed the mechanisms, characterization techniques, and application prospects of the MEG effect, but problems and disagreements have arisen over the measurement of MEG quantum efficiency in colloidal QDs and its impact on solar energy conversion.[329–334] Most of the previous studies have used ultrafast transient absorption techniques, as proposed by Schaller and Klimov,[325] to measure the MEG efficiency, which is defined as the number of electron–hole pairs produced per absorbed photon. The indirect nature of this method, however, has contributed to the diversity in the reported experimental data resulting from experimental artefacts, material degradation and surface effects of carrier trapping and photocharging.[335]

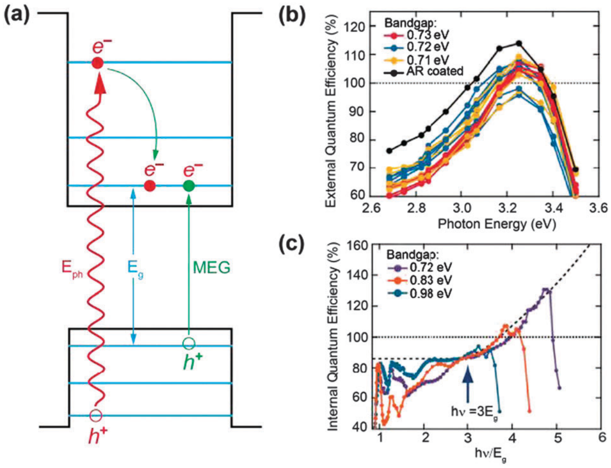

**Fig. 19** (a) A schematic drawing showing multiple exciton generation, whereby excited carriers generated in a quantum dot can channel excess photon energy to promote another electron across the bandgap rather than undergo thermalization. (b) External quantum efficiency measurements for 18 independent devices made with QD bandgaps of 0.71 eV (yellow), 0.72 eV (blue), and 0.73 eV (red), as well as a device with an antireflective coating (black). A maximum external quantum efficiency of up to 114% is achieved, confirming the generation of multiple excitons in QDs. (c) Collected internal quantum efficiency curves *versus* the ratio of photon energy to bandgap, $h\nu/E_g$, for three QD sizes. (Reprinted with permission from (a) ref. 320, (b) ref. 336, and (c) ref. 336. Copyright 2009 and 2011, respectively, Nature Publishing Group and American Association for the Advancement of Science.)

In 2011, Semonin and colleagues demonstrated direct proof of carrier multiplication in QDs.[336] They found that about 4% of total photocurrent in PbSe-based solar cells arises from the MEG effect. In such solar cells, the MEG was measured by determining the cell's external and internal quantum efficiencies at zero applied bias. In their work, a peak external quantum efficiency of 114% and a peak internal quantum efficiency of 130% were obtained (Fig. 19b and c). These findings are important because they not only provide direct evidence for MEG in QDs, but also show that MEG charge carriers can be collected with reasonable efficiency in suitably designed QD solar cells. Nevertheless, the impact of MEG on the power conversion efficiency of QD solar cells is limited, largely due to the high energy threshold of $\sim 3.0\ E_g$ required for MEG in PbSe QDs (as shown in Fig. 19b, only ultraviolet photons can result in efficient MEG). To make MEG have a substantial impact on PV devices, QD-based solar cells that can generate multiple excitons per visible photon at wavelength near the solar peak need to be developed in the future.

## 5. Down-shifting materials for PV applications

### 5.1 Concepts of luminescent down-shifting

Luminescent down-shifting can be utilized in many PV devices that exhibit poor spectral response to short-wavelength light. The down-shifting materials absorb the short-wavelength light, typically in the 300–500 nm range, and re-emit it at a longer wavelength where the external quantum efficiency of the PV device is high. While luminescent down-shifting could potentially enhance the solar cell efficiency, it is important to note that the design will not be able to overcome the Shockley–Queisser efficiency limit, as the absorption of a high energy photon by the down-shifting materials can only result in the generation of one electron–hole pair in the solar cell. To date, two main classes of down-shifting-based PV devices have been investigated: luminescent solar concentrators and planar down-shifting layers.[337] A luminescent solar concentrator is used to concentrate sunlight onto PV cells as a simple means to reduce the amount of expensive PV materials required.[338,339] The concentrator, typically composed of polymer sheets doped with luminescent species, converts a fraction of the incident sunlight into longer wavelength light that is subsequently guided towards a PV cell (Fig. 20a).[340,341] On the other hand, a planar down-shifting layer is generally placed directly onto the front surface of a solar cell to improve the device performance by overcoming the poor spectral response of the solar cell to short-wavelength light (Fig. 20b).[342]

The ideal materials for luminescent down-shifting should possess the following characteristics: (i) broadband absorption, particularly in the region where the spectral response of the

Published on 16 October 2012. Downloaded on 11/09/2014 14:42:06.

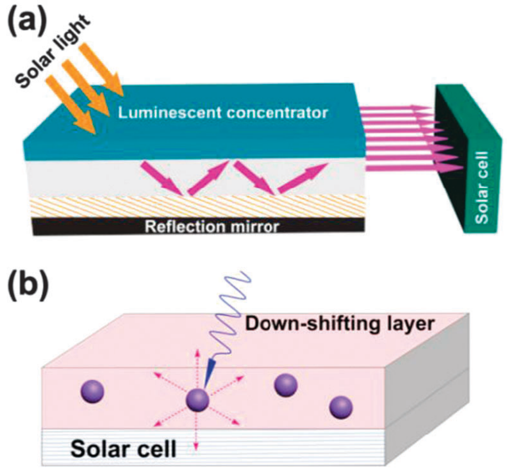

**Fig. 20** (a) Schematic design of a solar cell device equipped with a luminescent solar concentrator. The solar concentrator consists of a flat transparent slab with embedded luminescent down-shifting materials. The luminescent material absorbs incoming solar light and re-emits it at a longer wavelength isotropically. The emitted light, trapped in the slab *via* total internal reflection, is then guided to solar cells placed next to the edge of the slab. (b) Schematic design of a solar cell device with a luminescent down-shifting layer directly placed onto the surface of the solar cell. The down-shifting layer absorbs short wavelength photons and then re-emits them at a longer wavelength where the device exhibits a better spectral response.

solar cell is low; (ii) high absorption coefficient and high luminescence quantum efficiency so that all incident light results in emission; (iii) high transmittance and narrowband emission, particularly in the region where the device response is high; (iv) large Stokes shift to minimize the self-absorption energy losses due to the spectral overlap between the absorption and emission bands; and (v) long-term stability.[343] Up to now, inorganic phosphors and glasses, colloidal QDs and organolanthanide complexes have been widely investigated as potential candidates, as will be discussed below.

### 5.2 Phosphors and glasses

Table 5 summarizes the recent development of phosphors and glasses as down-shifting layers for a variety of PV devices (*e.g.*, c-Si, DSSCs, organic, and GaSb solar cells).[297,344–371] In these studies, the principal strategy has been to convert the ultraviolet–blue radiation into red–NIR emission by utilizing Stokes-shifted photoluminescence.

CRYSTALLINE SILICON SOLAR CELLS. The c-Si solar cells show significant differences in spectral response for short wavelength (ultraviolet–blue) and long wavelength (red–NIR) sunlight as discussed in Section 2.1, making them ideal systems for exploring down-shifting processes. Among various $Ln^{3+}$ ions, NIR-emitting $Nd^{3+}$ and $Yb^{3+}$ ions have attracted significant attention.[372–375] Their typical NIR emission around 1000 nm is just above the band edge of c-Si where the solar cell exhibits the greatest spectral response.[376–378] However, the luminescence of $Nd^{3+}$ and $Yb^{3+}$ is relatively weak due to parity-forbidden 4f–4f transitions.[379] To solve this problem, several research groups used other luminescent species (*e.g.*, $Ce^{3+}$, $Bi^{3+}$, $Pb^{2+}$, and $Cr^{3+}$) with higher absorption coefficients to sensitize the $Nd^{3+}$ or $Yb^{3+}$ ions.[349–351,356–360,380] In addition, host sensitization *via* ET from an excited host (such as ZnO and $TiO_2$) to $Ln^{3+}$ (Ln = Nd and Yb) ions also offers an effective way to boost the luminescence signal.[352–354,381–383]

**Table 5** Selected phosphors and glasses used as down-shifting layers for PV applications

| Materials | Preparation method | Excitation (nm) | Emission (nm) | Solar cell type | Ref. |
|---|---|---|---|---|---|
| $Y_2O_3:Eu^{3+}$ | — | 250 | 570–700 | c-Si | 344 |
| $La_2O_3:Eu^{3+}$ | Sol-gel Pechini method | 285 | 570–700 | c-Si | 345 |
| $YVO_4:Bi^{3+},Eu^{3+}$ thin films | Aqueous precipitation | 250–400 | 570–700 | c-Si | 346 |
| $YAG:Ce^{3+},Cr^{3+}$ | Solid-state reaction | 400–500 | 688 | c-Si | 347 |
| $MgSrAl_{10}O_{17}:Eu^{2+},Cr^{3+}$ | Solid-state reaction | 250–450 | 693 | c-Si | 348 |
| $SrB_4O_7:5\%Sm^{2+},5\%Eu^{2+}$ | Solid-state reaction | 300–600 | 685 | c-Si | 371 |
| $YAG:Ce^{3+},Nd^{3+}$ | Co-precipitation | 400–500 | 888, 1064 | c-Si | 349 |
| $YAG:Ce^{3+},Nd^{3+}$ | Sol–gel | 400–500 | 850–950, 1062 | c-Si | 350 |
| $Cr^{3+}$–$Yb^{3+}$ co-doped fluorosilicate glass | Glass melting | 300–700 | 950–1100 | c-Si | 351 |
| ZnO–$LiYbO_2$ hybrid phosphors | Solid-state reaction | 200–400 | 950–1100 | c-Si | 352, 353 |
| $Yb^{3+}$-doped glass ceramics containing ZnO nanocrystals | Glass melting | 200–400 | 950–1100 | c-Si | 354 |
| $LiYbMo_2O_8:Pb^{2+}$ | Solid-state reaction | 300–450 | 950–1100 | c-Si | 355 |
| $CaLaGa_3S_6O:Yb^{3+}$ | Solid-state reaction | 250–500 | 950–1100 | c-Si | 356 |
| $Yb^{3+}$ doped $LaSi_3N_5$ | Solid-state reaction | 300–400 | 950–1100 | c-Si | 357 |
| Ag nanoclusters and $Yb^{3+}$ ions co-doped oxyfluoride glasses | Glass melting | 300–500 | 950–1100 | c-Si | 358 |
| $Yb^{3+}$-doped glass ceramics containing $Ba_2TiSi_2O_8$ nanocrystals | Glass melting | 250–350 | 950–1100 | c-Si | 359 |
| $Yb^{3+}$-doped SrO–$TiO_2$–$SiO_2$ glasses | Glass melting | 250–350 | 950–1100 | c-Si | 360 |
| $Dy^{3+}$–$Tb^{3+}$ co-doped glass ceramics containing $YF_3$ nanocrystals | Glass melting | 300–500 | 450–650 | c-Si | 361 |
| $Cu^{+}$ doped glasses | Glass melting | 250–320 | 495 | c-Si | 362 |
| $Tb^{3+}$ doped glasses | Glass melting | 300–400 | 520–700 | Thin film | 363 |
| $LaVO_4:Dy^{3+}$ | Hydrothermal method | 250–320 | 450–600 | DSSCs | 364 |
| $Y_2O_3:Eu^{3+}$ | Co-precipitation | 230–320 | 570–700 | DSSCs | 365 |
| $TiO_2:Ln^{3+}$ (Ln = Eu, Sm) | Sol–gel | 200–400 | 570–700 | DSSCs | 366, 367 |
| $YVO_4:Bi^{3+},Ln^{3+}$ (Ln = Eu, Sm) | Solid-state reaction | 250–400 | 570–700 | DSSCs | 297 |
| $LaOF:Eu^{3+}$ | Hydrothermal method | 325–550 | 570–700 | Organic | 368 |
| $YVO_4:Bi^{3+},Eu^{3+}$ thin films | Solid-state reaction | 250–400 | 570–700 | Organic | 369 |
| Bismuth-doped oxide glasses | Glass melting | 300–800 | 1000–1600 | GaSb | 370 |

This journal is © The Royal Society of Chemistry 2013

Published on 16 October 2012. Downloaded on 11/09/2014 14:42:06.

Dye-sensitized solar cells. DSSCs based on the association of light-absorbing materials with wide bandgap semiconductor nanocrystals can work well in the visible range,[384] but they suffer from degradation when exposed to ultraviolet radiation.[385] Liu *et al.* in 2006 reported enhanced lifetime for DSSCs using $LaVO_4:Dy^{3+}$ film as an ultraviolet filter.[364] The $LaVO_4:Dy^{3+}$ transparent film was coated onto the back surface of an indium tin oxide (ITO) glass substrate modified with $TiO_2$ (Fig. 21a). The film converts the ultraviolet light (250–320 nm) into visible emission (450–700 nm), which is subsequently absorbed by the N3 ($[Ru(dcbpyH_2)_2(NCS)_2]$, $dcbpyH_2$: 2,2′-bipyridyl-4,4′-dicarboxylic acid) dye (Fig. 21b and c). It was found that a thin layer of $LaVO_4:Dy^{3+}$ results in an energy conversion efficiency enhanced by 23.3% as compared to the $LaVO_4$ film without the $Dy^{3+}$ dopant. A major limitation of using $Dy^{3+}$-doped $LaVO_4$ nanocrystals is that only a small portion of the deep ultraviolet sunlight (250–320 nm) is harvested. An ideal ultraviolet-absorbing luminescent converter for DSSCs should effectively capture the whole ultraviolet part of the solar spectrum ($\lambda \leq 400$ nm) and then convert these ultraviolet photons into narrowband emission exactly matching the absorption of the dye.

In 2011, Hafez *et al.*[366] reported the fabrication of lanthanide-doped $TiO_2$ photoelectrodes that are used to boost the conversion efficiency of DSSCs. Efficiency as high as 5.81% and 5.16% was reported for $Sm^{3+}$ and $Eu^{3+}$, respectively. In contrast, the undoped titania photoelectrodes only yielded 4.23% efficiency. The higher improvement with the $Sm^{3+}$ dopant in the overall efficiency of the solar cells was attributed to the smaller lifetime values of $Sm^{3+}$ than that of $Eu^{3+}$. Due to efficient host-to-$Sm^{3+}$ ET, the $Sm^{3+}$-doped $TiO_2$ thin films exhibited a characteristic orange-red emission upon excitation in the range of 250–400 nm. The orange-red emission was then absorbed by a sensitizing ruthenium dye N719 [$RuL_2(NCS)_2$, L = 4,4-dicarboxylate-2,2-bipyridine]. With further device optimization and new dyes (*e.g.*, N749), much higher efficiencies are likely.

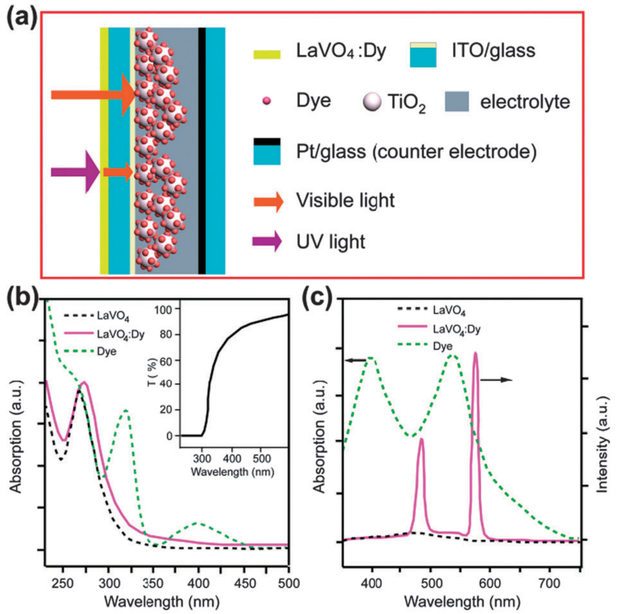

**Fig. 21** (a) Structure of a DSSC coupled with the $LaVO_4:Dy^{3+}$ ultraviolet-filtering thin-film. Note that ultraviolet light could be absorbed and converted to visible light *via* the thin-film. (b) The absorption spectrum of $LaVO_4:Dy^{3+}$ nanocrystals compared with the absorption spectrum of N3 dye. Inset: the transmittance spectrum of the $LaVO_4:Dy^{3+}$ thin-film. (c) The emission spectrum of $LaVO_4:Dy^{3+}$ nanocrystals compared with the absorption spectrum of N3 dye. (Reprinted with permission from ref. 364. Copyright 2006, American Institute of Physics.)

Organic solar cells. Organic solar cells are promising low-cost alternatives to conventional solid-state solar cells, but their rather low photostability under prolonged ultraviolet irradiation has kept them from widespread commercial use. If the harmful ultraviolet photons could be converted into visible light, both the lifetime and the power conversion efficiency will be enhanced.[368,369] Xu *et al.* in 2011 used the $YVO_4:Eu^{3+}/Bi^{3+}$ luminescent nano-film converter as an ultraviolet-filter to improve the photostability of poly(3-hexylthiophene) (P3HT).[369] The $YVO_4:Eu^{3+}/Bi^{3+}$ nano-film efficiently converts broadband ultraviolet light of 220–400 nm into red emission around 621 nm with a quantum efficiency of up to 69%. The authors observed that the photostability of the P3HT polymer increased by 3 times with the $YVO_4:Eu^{3+}/Bi^{3+}$ nano-film, as opposed to that measured without the nano-film.[369]

GaSb solar cells. Owing to their excellent quantum efficiency at longer infrared wavelengths, gallium antimonide solar cells have emerged as the dominant cell technology for constructing high performance thermophotovoltaic generators. Peng and Wondraczek in 2009 demonstrated the use of bismuth-doped glasses as plain-shifting layers to improve the efficiency of GaSb solar cells ($E_g$ = 0.70 eV; 1771 nm).[370] Such glasses exhibit strong absorption in the ultraviolet–green spectral range but high transmission at wavelengths larger than ~800 nm, while showing broad NIR luminescence (1000–1500 nm) possibly due to $Bi^+$ emission. At an optimum molar concentration of 1% Bi, the cell exhibits an increase by a factor of ~1.5 in the overall external quantum efficiency.

### 5.3 Semiconductor quantum dots

Semiconductor QDs are a different class of luminescent down-shifting materials that have been recently reported for solar cell applications. In particular, CdSe, CdSe–ZnS, CdS, and CdSe–CdTe have generated great excitement because they feature broadband absorbance, high quantum yield, and tunable emission characteristics in the visible region.[386–401] However, the overall efficiencies of these solar cells need to be improved due to large overlap between the emission and absorption spectra of the QDs.[402,403] In contrast, the use of NIR-emitting QDs (*e.g.*, $Ag_2S$,[404] PbS,[405] ZnTe–CdSe,[406] CdSe–ZnTe,[407] and CdTe–CdSe[408]) can greatly reduce re-absorption. As an added benefit, the NIR emission of QDs can be tuned to match the bandgap of c-Si solar cells, thereby opening the possibility of developing luminescent solar concentrators with much higher conversion efficiency.

In 2010, Shcherbatyuk *et al.* investigated the viability of using PbS NIR-emitting QDs as down-shifting materials in luminescent solar concentrators.[402] When compared with CdSe–ZnS, the PbS QDs exhibited a broad spectral response

Published on 16 October 2012. Downloaded on 11/09/2014 14:42:06.

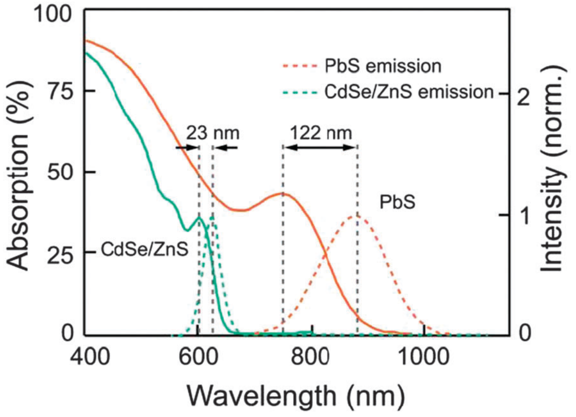

**Fig. 22** Comparison of absorption and emission spectra of CdSe–ZnS and PbS QDs. The Stokes shifts for CdSe–ZnS and PbS QDs are 23 and 122 nm, respectively. (Reprinted with permission from ref. 402. Copyright 2009, American Institute of Physics.)

extending from the visible to the NIR region of the solar spectrum (Fig. 22). Furthermore, the PbS QDs showed a large Stokes shift of 122 nm (*versus* 23 nm for CdSe–ZnS QDs) due to a strong quantum confinement effect. More importantly, the authors found that the NIR emission wavelength of the QDs is slightly larger than the bandgap of c-Si (1.1 eV), achieving calculated optical and power conversion efficiency in the luminescent solar concentrator as high as 12.6% and 3.2%, respectively.

### 5.4 Rare-earth organic complexes

Rare-earth organic complexes, composed of a ligand acting as an antenna (or sensitizer) and an emitting lanthanide ion, are an important class of down-shifting materials for PV modules. Unlike conventional organic dyes and QDs, these organolanthanide complexes feature large Stokes shift and completely avoid self-absorption losses (Fig. 23a).[409–411] In principle, the luminescence process in organolanthanide complexes occurs in three steps: (i) light absorption by a properly selected ligand; (ii) highly efficient intra-energy conversion from the singlet ($S_1$) to the triplet ($T_1$) states of the ligand by inter-system crossing; and (iii) resonant ET from the T1 state of the ligand to the excited state of the $Ln^{3+}$ ion (Fig. 23b). Europium complexes that feature a main emission at 612 nm have been investigated for c-Si and DSSCs.[412–420] In contrast, $Tb^{3+}$-based organic complexes are more suitable for amorphous Si solar cells with a wavelength of maximum efficiency at about 500 nm.[421,422] In particular, NIR-emitting metal–organic frameworks that contain $Yb^{3+}$ or $Nd^{3+}$ are promising candidates for c-Si solar cells.[423–426] It is important to note that the organolanthanide complexes with high luminescence quantum efficiency and a broad absorption plateau in the visible region are preferred for PV applications.

## 6. Conclusions and outlook

In this *review*, fundamentals for luminescent materials as spectral converters are presented in the context of enhancing solar cell efficiency. One of the major challenges in designing solar cell devices is how to minimize energy losses due to the spectral mismatch between the solar cell and incident solar spectrum. To make full use of the solar spectrum, innovative approaches through use of upconversion, quantum-cutting, and down-shifting luminescent materials, albeit still very much in its infancy stage, have shown promise for the development of these materials as spectral converters to effectively reduce the spectral mismatch losses and, as a consequence, boost the efficiency of solar cells.

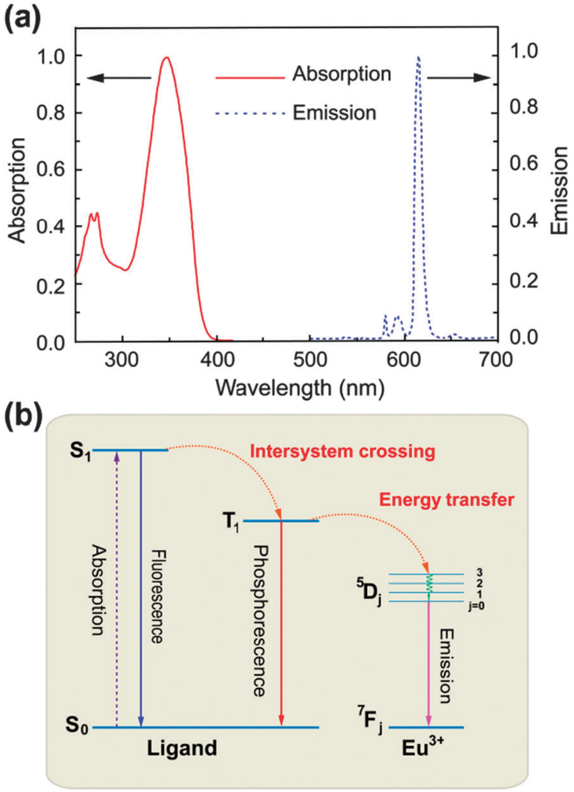

**Fig. 23** (a) Normalized absorption (solid line) and emission spectra (dashed line) of $Eu(TTA)_3(TTPO)_2$ where TTA and TTPO stand for thenoyl trifluoroacetone and triphenyl phosphine oxide, respectively. (b) Schematic diagram showing the ET process from the organic ligand to $Eu^{3+}$ in organometallic compounds of europium. (Reprinted with permission from ref. 410. Copyright 2011, Elsevier Ltd.)

Upconversion is able to harvest the sub-bandgap sunlight. Proof-of-concept experiments have been widely performed for $Er^{3+}$-doped upconverters (for c-Si solar cells) and $Ln^{3+}$–$Yb^{3+}$ (Ln = Er, Tm, and Ho) co-doped upconverters (for wide bandgap solar cells). However, two major drawbacks associated with this approach currently limit the practical application of upconverters for solar cells. First, the efficiency of current $Ln^{3+}$-doped upconverters investigated for solar cells is generally low (less than 3%).[194] The upconversion efficiency may be enhanced by using plasmonic resonance[427] or photonic crystals.[428] High excitation density, which can be easily realized using lasers, also can lead to high upconversion efficiency, but it will require concentrated sunlight. In this respect, low-power TTA-based upconversion in organic molecules is particularly promising for wide bandgap solar cells, provided that efficient NIR-to-visible

This journal is © The Royal Society of Chemistry 2013

Published on 16 October 2012. Downloaded on 11/09/2014 14:42:06.

upconversion can be achieved.[197,198] Second, only a small fraction of sub-bandgap sunlight can be upconverted due to the small absorption cross-sections of $Ln^{3+}$ ions. Transition metal ions,[429] quantum dots,[430] and organic dyes[431] with large absorption cross-sections might be exploited as sensitizers to enable broadband absorption of $Ln^{3+}$ ions.

Quantum-cutting allows the efficient use of the high-energy above-bandgap sunlight, which provides potential for efficiency enhancement of narrow bandgap solar cells (c-Si solar cells and germanium solar cells). Efficient narrow-band NIR quantum-cutting with internal quantum efficiency close to 200% has been extensively demonstrated in the $Ln^{3+}$–$Yb^{3+}$ (Ln = Tb, Tm, Pr, Er, Nd, Ho, and Dy) couples for c-Si solar cells. In these couples, $Yb^{3+}$ ions function as ideal acceptors with a single NIR emission band around 1000 nm, just above the bandgap of c-Si. To solve the absorption problem inherent in $Ln^{3+}$ donors, other species (*e.g.*, $Ce^{3+}$, $Eu^{2+}$, $Yb^{2+}$, and $Bi^{3+}$ ions) or hosts have been explored for sensitization. NIR quantum-cutting with $Ce^{3+}$–$Er^{3+}$ and $Eu^{2+}$–$Er^{3+}$ couples, which can give rise to NIR emission around 1500 nm from $Er^{3+}$ donors, has been reported for germanium solar cells. Quantum-cutting has been proven to be a linear process independent of the incident power. This allows for the use of non-concentrated sunlight. However, quantum-cutting with external quantum efficiency larger than 100% has been rarely reported.[432] Thus far, no proof-of-concept experiment has been reported for quantum-cutting in PV applications. Urgent tasks for the distant future in this area are: (i) developing novel characterization techniques to provide direct evidence of the existence of NIR quantum-cutting; and (ii) investigating the effect of quantum-cutting materials on the performance of solar cells.

Down-shifting offers the ability to improve the spectral response of solar cells to short-wavelength sunlight. Lanthanide-doped phosphors and glasses, QDs, and organolanthanide complexes can be used in luminescent solar concentrators and planar down-shifting layers for enhancing power-conversion efficiency in solar cells. However, the fabrication of a highly efficient luminescent solar concentrator remains difficult,[433] and the optimal configuration may involve a combination or design layout of different luminescent materials.[434,435]

In conclusion, the application of luminescent materials as spectral converters to PV applications could not come at a more opportune time given the significant increase in the global demand for energy in recent years. Despite the daunting challenges of realizing low-cost and highly efficient solar cells, further exploration and attempts to use these spectral converting materials for PV devices and systems will certainly be exciting.

## Acknowledgements

X.L. acknowledges the National Research Foundation and the Economic Development Board (Singapore-Peking-Oxford Research Enterprise, COY-15-EWI-RCFSA/N197-1), the Singapore-MIT Alliance, the Ministry of Education (MOE2010-t2-1-083), and the Agency for Science, Technology and Research (A*STAR) for supporting this work. W.H. acknowledges financial support from National Basic Research Program of China (973 Program, 2009CB930601), National Natural Science Foundation of China (BZ2010043, 20974046, 20774043, 51173081, 50428303, 61136003) and Natural Science Foundation of Jiangsu Province (BK2008053, BK2009025, 10KJB510013).

## References

1 G. D. Scholes, G. R. Fleming, A. Olaya-Castro and R. van Grondelle, *Nat. Chem.*, 2011, **3**, 763–774.
2 N. S. Lewis, *Science*, 2007, **315**, 798–801.
3 H. Aguas, S. K. Ram, A. Araujo, D. Gaspar, A. Vicente, S. A. Filonovich, E. Fortunato, R. Martins and I. Ferreira, *Energy Environ. Sci.*, 2011, **4**, 4620–4632.
4 H. A. Atwater and A. Polman, *Nat. Mater.*, 2010, **9**, 205–213.
5 A. J. Nozik and J. Miller, *Chem. Rev.*, 2010, **110**, 6443–6445.
6 P. K. Nayak, G. Garcia-Belmonte, A. Kahn, J. Bisquert and D. Cahen, *Energy Environ. Sci.*, 2012, **5**, 6022–6039.
7 W. Y. Wong and C. L. Ho, *Acc. Chem. Res.*, 2010, **43**, 1246–1256.
8 J. D. Servaites, M. A. Ratner and T. J. Marks, *Energy Environ. Sci.*, 2011, **4**, 4410–4422.
9 A. Yella, H. W. Lee, H. N. Tsao, C. Y. Yi, A. K. Chandiran, M. K. Nazeeruddin, E. W. G. Diau, C. Y. Yeh, S. M. Zakeeruddin and M. Gratzel, *Science*, 2011, **334**, 629–634.
10 M. D. Kelzenberg, S. W. Boettcher, J. A. Petykiewicz, D. B. Turner-Evans, M. C. Putnam, E. L. Warren, J. M. Spurgeon, R. M. Briggs, N. S. Lewis and H. A. Atwater, *Nat. Mater.*, 2010, **9**, 239–244.
11 X. H. Wang, G. I. Koleilat, J. Tang, H. Liu, I. J. Kramer, R. Debnath, L. Brzozowski, D. A. R. Barkhouse, L. Levina, S. Hoogland and E. H. Sargent, *Nat. Photonics*, 2011, **5**, 480–484.
12 K. Q. Peng and S. T. Lee, *Adv. Mater.*, 2011, **23**, 198–215.
13 A. I. Hochbaum and P. D. Yang, *Chem. Rev.*, 2010, **110**, 527–546.
14 D. Timmerman, I. Izeddin, P. Stallinga, I. N. Yassievich and T. Gregorkiewicz, *Nat. Photonics*, 2008, **2**, 105–109.
15 B. E. Hardin, H. J. Snaith and M. D. McGehee, *Nat. Photonics*, 2012, **6**, 162–169.
16 J. W. Schwede, I. Bargatin, D. C. Riley, B. E. Hardin, S. J. Rosenthal, Y. Sun, F. Schmitt, P. Pianetta, R. T. Howe, Z. X. Shen and N. A. Melosh, *Nat. Mater.*, 2010, **9**, 762–767.
17 N. C. Giebink, G. P. Wiederrecht and M. R. Wasielewski, *Nat. Photonics*, 2011, **5**, 695–702.
18 P. V. Kamat, K. Tvrdy, D. R. Baker and J. G. Radich, *Chem. Rev.*, 2010, **110**, 6664–6688.
19 S. Chu and A. Majumdar, *Nature*, 2012, **488**, 294–303.
20 M. Graetzel, R. A. J. Janssen, D. B. Mitzi and E. H. Sargent, *Nature*, 2012, **488**, 304–312.
21 B. S. Richards, *Sol. Energy Mater. Sol. Cells*, 2006, **90**, 2329–2337.
22 W. Shockley and H. J. Queisser, *J. Appl. Phys.*, 1961, **32**, 510–519.
23 C. Strumpel, M. McCann, G. Beaucarne, V. Arkhipov, A. Slaoui, V. Svrcek, C. del Canizo and I. Tobias, *Sol. Energy Mater. Sol. Cells*, 2007, **91**, 238–249.
24 B. S. Richards, *Sol. Energy Mater. Sol. Cells*, 2006, **90**, 1189–1207.
25 A. Shalav, B. S. Richards and M. A. Green, *Sol. Energy Mater. Sol. Cells*, 2007, **91**, 829–842.
26 T. Trupke, A. Shalav, B. S. Richards, P. Wurfel and M. A. Green, *Sol. Energy Mater. Sol. Cells*, 2006, **90**, 3327–3338.
27 G. Conibeer, *Mater. Today*, 2007, **10**, 42–50.
28 G. F. Brown and J. Q. Wu, *Laser Photonics Rev.*, 2009, **3**, 394–405.
29 S. V. Eliseeva and J. C. G. Bunzli, *Chem. Soc. Rev.*, 2010, **39**, 189–227.
30 D. Chen, Y. Wang and M. Hong, *Nano Energy*, 2012, **1**, 73–90.
31 B. M. van der Ende, L. Aarts and A. Meijerink, *Phys. Chem. Chem. Phys.*, 2009, **11**, 11081–11095.
32 T. Trupke, M. A. Green and P. Wurfel, *J. Appl. Phys.*, 2002, **92**, 4117–4122.
33 Q. Y. Zhang and X. Y. Huang, *Prog. Mater. Sci.*, 2010, **55**, 353–427.
34 T. Trupke, M. A. Green and P. Wurfel, *J. Appl. Phys.*, 2002, **92**, 1668–1674.
35 J. Nelson, *The Physics of Solar Cells*, Imperial College Press, 2002.
36 D. M. Powell, M. T. Winkler, H. J. Choi, C. B. Simmons, D. B. Needleman and T. Buonassisi, *Energy Environ. Sci.*, 2012, **5**, 5874–5883.

Published on 16 October 2012. Downloaded on 11/09/2014 14:42:06.

37 M. A. Green, K. Emery, Y. Hishikawa and W. Warta, *Prog. Photovoltaics*, 2011, **19**, 84–92.
38 M. A. Green, K. Emery, Y. Hishikawa and W. Warta, *Prog. Photovoltaics*, 2010, **18**, 346–352.
39 C. Feldmann, T. Justel, C. R. Ronda and P. J. Schmidt, *Adv. Funct. Mater.*, 2003, **13**, 511–516.
40 B. Valeur and M. N. Berberan-Santos, *J. Chem. Educ.*, 2011, **88**, 731–738.
41 G. Blasse and B. C. Grabmaier, *Luminescent Materials*, Springer, Berlin, 1994.
42 C. R. Ronda, in *Luminescence From Theory to Applications*, ed. C. R. Ronda, Wiley-VCH Verlag GmbH & Co. KGaA, Weinheim, 2008, pp. 1–34.
43 S. Kuck, I. Sokolska, M. Henke, T. Scheffler and E. Osiac, *Phys. Rev. B: Condens. Matter.*, 2005, **71**, 165112.
44 L. S. Rohwer and J. E. Martin, *J. Lumin.*, 2005, **115**, 77–90.
45 M. H. V. Werts, R. T. F. Jukes and J. W. Verhoeven, *Phys. Chem. Chem. Phys.*, 2002, **4**, 1542–1548.
46 K. Binnemans, *Chem. Rev.*, 2009, **109**, 4283–4374.
47 J. C. G. Bunzli, *Acc. Chem. Res.*, 2006, **39**, 53–61.
48 J. C. G. Bunzli and C. Piguet, *Chem. Soc. Rev.*, 2005, **34**, 1048–1077.
49 J. C. G. Bunzli, *Chem. Rev.*, 2010, **110**, 2729–2755.
50 S. Ye, F. Xiao, Y. X. Pan, Y. Y. Ma and Q. Y. Zhang, *Mater. Sci. Eng., R*, 2010, **71**, 1–34.
51 T. Justel, H. Nikol and C. Ronda, *Angew. Chem., Int. Ed.*, 1998, **37**, 3085–3103.
52 H. A. Hoppe, *Angew. Chem., Int. Ed.*, 2009, **48**, 3572–3582.
53 L. D. Carlos, R. A. S. Ferreira, V. D. Bermudez, B. Julian-Lopez and P. Escribano, *Chem. Soc. Rev.*, 2011, **40**, 536–549.
54 A. Kar and A. Patra, *Nanoscale*, 2012, **4**, 3608–3619.
55 H. Goesmann and C. Feldmann, *Angew. Chem., Int. Ed.*, 2010, **49**, 1362–1395.
56 G. H. Dieke, *Spectra and Energy Levels of Rare Earth Ions in Crystals*, Wiley, New York, 1968.
57 G. K. Liu, in *Spectroscopic Properties of Rare Earths in Optical Materials*, ed. G. K. Liu and B. Jacquier, Springer Verlag, Berlin, 2005, pp. 1–94.
58 M. F. H. Schuurmans and J. M. F. Vandijk, *Physica B+C (Amsterdam)*, 1984, **123**, 131–155.
59 J. M. F. Vandijk and M. F. H. Schuurmans, *J. Chem. Phys.*, 1983, **78**, 5317–5323.
60 F. Vetrone and J. A. Capobianco, *Int. J. Nanotechnol.*, 2008, **5**, 1306–1339.
61 P. P. Fedorov, A. A. Luginina, S. V. Kuznetsov and V. V. Osiko, *J. Fluorine Chem.*, 2011, **132**, 1012–1039.
62 R. T. Wegh, H. Donker, K. D. Oskam and A. Meijerink, *Science*, 1999, **283**, 663–666.
63 R. T. Wegh, H. Donker, K. D. Oskam and A. Meijerink, *J. Lumin.*, 1999, **82**, 93–104.
64 W. W. Piper and F. S. Ham, *J. Lumin.*, 1974, **8**, 344–348.
65 J. L. Sommerdijk, A. A. Bril and A. W. de Jager, *J. Lumin.*, 1974, **8**, 341–343.
66 J. L. Sommerdijk, A. Bril and A. W. de Jager, *J. Lumin.*, 1974, **9**, 288–296.
67 A. M. Srivastava and W. W. Beers, *J. Lumin.*, 1997, **71**, 285–290.
68 F. Auzel, in *Spectroscopic Properties of Rare Earths in Optical Materials*, ed. G. K. Liu and B. Jacquier, Springer Verlag, Berlin, 2005, pp. 266–319.
69 D. L. Dexter, *J. Chem. Phys.*, 1953, **21**, 836–850.
70 T. Miyakawa and D. L. Dexter, *Phys. Rev. B: Solid State*, 1970, **1**, 2961–2969.
71 N. Yamada, S. Shionoya and T. Kushida, *J. Phys. Soc. Jpn.*, 1972, **32**, 1577–1586.
72 F. Wang, D. Banerjee, Y. S. Liu, X. Y. Chen and X. G. Liu, *Analyst*, 2010, **135**, 1839–1854.
73 F. Wang and X. G. Liu, *Chem. Soc. Rev.*, 2009, **38**, 976–989.
74 F. Auzel, *Chem. Rev.*, 2004, **104**, 139–173.
75 F. Wang, R. R. Deng, J. Wang, Q. X. Wang, Y. Han, H. M. Zhu, X. Y. Chen and X. G. Liu, *Nat. Mater.*, 2011, **10**, 968–973.
76 F. Wang, Y. Han, C. S. Lim, Y. H. Lu, J. Wang, J. Xu, H. Y. Chen, C. Zhang, M. H. Hong and X. G. Liu, *Nature*, 2010, **463**, 1061–1065.
77 F. Wang and X. G. Liu, *J. Am. Chem. Soc.*, 2008, **130**, 5642–5643.
78 F. Wang, J. Wang and X. G. Liu, *Angew. Chem., Int. Ed.*, 2010, **49**, 7456–7460.
79 Y. M. Yang, Q. Shao, R. R. Deng, C. Wang, X. Teng, K. Cheng, Z. Cheng, L. Huang, Z. Liu, X. G. Liu and B. G. Xing, *Angew. Chem., Int. Ed.*, 2012, **51**, 3125–3129.
80 R. R. Deng, X. J. Xie, M. Vendrell, Y. T. Chang and X. G. Liu, *J. Am. Chem. Soc.*, 2011, **133**, 20168–20171.
81 J. Wang, F. Wang, C. Wang, Z. Liu and X. G. Liu, *Angew. Chem., Int. Ed.*, 2011, **50**, 10369–10372.
82 X. J. Xue, F. Wang and X. G. Liu, *J. Mater. Chem.*, 2011, **21**, 13107–13127.
83 S. Ye, Y. J. Li, D. C. Yu, G. P. Dong and Q. Y. Zhang, *J. Mater. Chem.*, 2011, **21**, 3735–3739.
84 E. Downing, L. Hesselink, J. Ralston and R. Macfarlane, *Science*, 1996, **273**, 1185–1189.
85 G. F. Wang, Q. Peng and Y. D. Li, *Acc. Chem. Res.*, 2011, **44**, 322–332.
86 L. H. Fischer, G. S. Harms and O. S. Wolfbeis, *Angew. Chem., Int. Ed.*, 2011, **50**, 4546–4551.
87 J. Zhou, Z. Liu and F. Y. Li, *Chem. Soc. Rev.*, 2012, **41**, 1323–1349.
88 C. X. Li and J. Lin, *J. Mater. Chem.*, 2010, **20**, 6831–6847.
89 M. Haase and H. Schafer, *Angew. Chem., Int. Ed.*, 2011, **50**, 5808–5829.
90 Q. Ju, D. T. Tu, Y. S. Liu, R. F. Li, H. M. Zhu, J. C. Chen, Z. Chen, M. D. Huang and X. Y. Chen, *J. Am. Chem. Soc.*, 2012, **134**, 1323–1330.
91 D. T. Tu, L. Q. Liu, Q. Ju, Y. S. Liu, H. M. Zhu, R. F. Li and X. Y. Chen, *Angew. Chem., Int. Ed.*, 2011, **50**, 6306–6310.
92 H. S. Mader, P. Kele, S. M. Saleh and O. S. Wolfbeis, *Curr. Opin. Chem. Biol.*, 2010, **14**, 582–596.
93 C. Yan, A. Dadvand, F. Rosei and D. F. Perepichka, *J. Am. Chem. Soc.*, 2010, **132**, 8868–8869.
94 N. Bogdan, F. Vetrone, G. A. Ozin and J. A. Capobianco, *Nano Lett.*, 2011, **11**, 835–840.
95 X. C. Ye, J. E. Collins, Y. J. Kang, J. Chen, D. T. N. Chen, A. G. Yodh and C. B. Murray, *Proc. Natl. Acad. Sci. U. S. A.*, 2010, **107**, 22430–22435.
96 O. Ehlert, R. Thomann, M. Darbandi and T. Nann, *ACS Nano*, 2008, **2**, 120–124.
97 F. Chen, W. B. Bu, S. J. Zhang, X. H. Liu, J. N. Liu, H. Y. Xing, Q. F. Xiao, L. P. Zhou, W. J. Peng, L. Z. Wang and J. L. Shi, *Adv. Funct. Mater.*, 2011, **21**, 4285–4294.
98 G. S. Yi and G. M. Chow, *Chem. Mater.*, 2007, **19**, 341–343.
99 F. Zhang, G. B. Braun, A. Pallaoro, Y. Zhang, Y. Shi, D. Cui, M. Moskovits, D. Zhao and G. D. Stucky, *Nano Lett.*, 2012, **12**, 61–67.
100 L. Cheng, K. Yang, Y. G. Li, X. Zeng, M. W. Shao, S. T. Lee and Z. Liu, *Biomaterials*, 2012, **33**, 2215–2222.
101 C. Bouzigues, T. Gacoin and A. Alexandrou, *ACS Nano*, 2011, **5**, 8488–8505.
102 M. K. G. Jayakumar, N. M. Idris and Y. Zhang, *Proc. Natl. Acad. Sci. U. S. A.*, 2012, **109**, 8483–8488.
103 G. Lu, S. Z. Li, Z. Guo, O. K. Farha, B. G. Hauser, X. Y. Qi, Y. Wang, X. Wang, S. Y. Han, X. G. Liu, J. S. DuChene, H. Zhang, Q. C. Zhang, X. D. Chen, J. Ma, S. C. J. Loo, W. D. Wei, Y. H. Yang, J. T. Hupp and F. W. Huo, *Nat. Chem.*, 2012, **4**, 310–316.
104 J. C. Zhou, Z. L. Yang, W. Dong, R. J. Tang, L. D. Sun and C. H. Yan, *Biomaterials*, 2011, **32**, 9059–9067.
105 H. Schafer, P. Ptacek, H. Eickmeier and M. Haase, *Adv. Funct. Mater.*, 2009, **19**, 3091–3097.
106 H. Schafer, P. Ptacek, O. Zerzouf and M. Haase, *Adv. Funct. Mater.*, 2008, **18**, 2913–2918.
107 H. Schaefer, P. Ptacek, K. Koempe and M. Haase, *Chem. Mater.*, 2007, **19**, 1396–1400.
108 G. Tian, Z. J. Gu, L. J. Zhou, W. Y. Yin, X. X. Liu, L. Yan, S. Jin, W. L. Ren, G. M. Xing, S. J. Li and Y. L. Zhao, *Adv. Mater.*, 2012, **24**, 1226–1231.
109 C. H. Dong, A. Korinek, B. Blasiak, B. Tomanek and F. C. J. M. van Veggel, *Chem. Mater.*, 2012, **24**, 1297–1305.
110 N. J. J. Johnson, A. Korinek, C. Dong and F. C. J. M. van Veggel, *J. Am. Chem. Soc.*, 2012, **134**, 11068–11071.
111 G. Y. Chen, H. L. Qiu, R. W. Fan, S. W. Hao, S. Tan, C. H. Yang and G. Han, *J. Mater. Chem.*, 2012, **22**, 20190–20196.
112 G. Y. Chen, T. Y. Ohulchanskyy, A. Kachynski, H. Agren and P. N. Prasad, *ACS Nano*, 2011, **5**, 4981–4986.
113 S. J. Zeng, J. J. Xiao, Q. B. Yang and J. H. Hao, *J. Mater. Chem.*, 2012, **22**, 9870–9874.

This journal is © The Royal Society of Chemistry 2013

Published on 16 October 2012. Downloaded on 11/09/2014 14:42:06.

114 W. L. Ren, G. Tian, L. J. Zhou, W. Y. Yin, L. Yan, S. Jin, Y. Zu, S. J. Li, Z. J. Gu and Y. L. Zhao, *Nanoscale*, 2012, **4**, 3754–3760.

115 E. M. Chan, G. Han, J. D. Goldberg, D. J. Gargas, A. D. Ostrowski, P. J. Schuck, B. E. Cohen and D. J. Milliron, *Nano Lett.*, 2012, 3839–3845.

116 F. Chen, S. J. Zhang, W. B. Bu, Y. Chen, Q. F. Xiao, J. A. Liu, H. Y. Xing, L. P. Zhou, W. J. Peng and J. L. Shi, *Chem.–Eur. J.*, 2012, **18**, 7082–7090.

117 Y. Wei, Q. Chen, B. Wu, A. Zhou and D. Xing, *Nanoscale*, 2012, **4**, 3901–3909.

118 S. J. Wu, N. Duan, X. Y. Ma, Y. Xia, Y. Yu, Z. P. Wang and H. X. Wang, *Chem. Commun.*, 2012, **48**, 4866–4868.

119 T. He, W. Wei, L. Ma, R. Chen, S. Wu, H. Zhang, Y. Yang, J. Ma, L. Huang, G. G. Gurzadyan and H. Sun, *Small*, 2012, **8**, 2163–2168.

120 L. L. Li, R. B. Zhang, L. L. Yin, K. Z. Zheng, W. P. Qin, P. R. Selvin and Y. Lu, *Angew. Chem., Int. Ed.*, 2012, **51**, 6121–6125.

121 X. Teng, Y. Zhu, W. Wei, S. Wang, J. Huang, R. Naccache, W. Hu, A. I. Y. Tok, Y. Han, Q. Zhang, Q. Fan, W. Huang, J. A. Capobianco and L. Huang, *J. Am. Chem. Soc.*, 2012, **134**, 8340–8343.

122 W. Wei, T. He, X. Teng, S. Wu, L. Ma, H. Zhang, J. Ma, Y. Yang, H. Chen, Y. Han, H. Sun and L. Huang, *Small*, 2012, **8**, 2271–2276.

123 G. Dong, B. Chen, X. Xiao, G. Chai, Q. Liang, M. Peng and J. Qiu, *Nanoscale*, 2012, **4**, 4658–4666.

124 Q. Liu, Y. Sun, T. S. Yang, W. Feng, C. G. Li and F. Y. Li, *J. Am. Chem. Soc.*, 2011, **133**, 17122–17125.

125 D. Chen, Y. Yu, F. Huang, H. Lin, P. Huang, A. Yang, Z. Wang and Y. Wang, *J. Mater. Chem.*, 2012, **22**, 2632–2640.

126 D. Chen, Y. Yu, F. Huang, P. Huang, A. Yang and Y. Wang, *J. Am. Chem. Soc.*, 2010, **132**, 9976–9978.

127 X. J. Zhu, J. Zhou, M. Chen, M. Shi, W. Feng and F. Y. Li, *Biomaterials*, 2012, **33**, 4618–4627.

128 Y. F. Wang, L. D. Sun, J. W. Xiao, W. Feng, J. C. Zhou, J. Shen and C. H. Yan, *Chem.–Eur. J.*, 2012, **18**, 5558–5564.

129 F. Ferraro and C. Z. Hadad, *J. Phys. Chem. C*, 2012, **116**, 7134–7143.

130 F. Wang, J. Wang, J. Xu, X. J. Xue, H. Y. Chen and X. G. Liu, *Spectrosc. Lett.*, 2010, **43**, 400–405.

131 J. Wang, F. Wang, J. Xu, Y. Wang, Y. S. Liu, X. Y. Chen, H. Y. Chen and X. G. Liu, *C. R. Chim.*, 2010, **13**, 731–736.

132 S. Schietinger, T. Aichele, H. Q. Wang, T. Nann and O. Benson, *Nano Lett.*, 2010, **10**, 134–138.

133 J. H. Hao, Y. Zhang and X. H. Wei, *Angew. Chem., Int. Ed.*, 2011, **50**, 6876–6880.

134 A. X. Yin, Y. W. Zhang, L. D. Sun and C. H. Yan, *Nanoscale*, 2010, **2**, 953–959.

135 C. Zhang, H. P. Zhou, L. Y. Liao, W. Feng, W. Sun, Z. X. Li, C. H. Xu, C. J. Fang, L. D. Sun, Y. W. Zhang and C. H. Yan, *Adv. Mater.*, 2010, **22**, 633–637.

136 G. A. Jia, H. P. You, Y. H. Song, Y. J. Huang, M. Yang and H. J. Zhang, *Inorg. Chem.*, 2010, **49**, 7721–7725.

137 S. Wang, S. Q. Su, S. Y. Song, R. P. Deng and H. J. Zhang, *CrystEngComm*, 2012, **14**, 4266–4269.

138 M. F. Joubert, *Opt. Mater. (Amsterdam)*, 1999, **11**, 181–203.

139 J. S. Chivian, W. E. Case and D. D. Eden, *Appl. Phys. Lett.*, 1979, **35**, 124–125.

140 P. Gibart, F. Auzel, J. C. Guillaume and K. Zahraman, *Jpn. J. Appl. Phys., Part 1*, 1996, **35**, 4401–4402.

141 A. Shalav, B. S. Richards, T. Trupke, K. W. Kramer and H. U. Gudel, *Appl. Phys. Lett.*, 2005, **86**, 013505.

142 S. Fischer, J. C. Goldschmidt, P. Loper, G. H. Bauer, R. Bruggemann, K. Kramer, D. Biner, M. Hermle and S. W. Glunz, *J. Appl. Phys.*, 2010, **108**, 044912.

143 S. Ivanova, F. Pelle, A. Tkachuk, M. F. Joubert, Y. Guyot and V. P. Gapontzev, *J. Lumin.*, 2008, **128**, 914–917.

144 X. F. Liang, X. Y. Huang and Q. Y. Zhang, *J. Fluoresc.*, 2009, **19**, 285–289.

145 X. F. Wang, X. H. Yan and C. X. Kan, *J. Mater. Chem.*, 2011, **21**, 4251–4256.

146 S. Ivanova and F. Pelle, *J. Opt. Soc. Am. B*, 2009, **26**, 1930–1938.

147 F. Lahoz, *Opt. Lett.*, 2008, **33**, 2982–2984.

148 F. Lahoz, C. Perez-Rodriguez, S. E. Hernandez, I. R. Martin, V. Lavin and U. R. Rodriguez-Mendoza, *Sol. Energy Mater. Sol. Cells*, 2011, **95**, 1671–1677.

149 H.-Y. Lin, H.-N. Chen, T.-H. Wu, C.-S. Wu, Y.-K. Su and S.-Y. Chu, *J. Am. Ceram. Soc.*, 2012, **95**, 3172–3179.

150 X. D. Zhang, X. Jin, D. F. Wang, S. Z. Xiong, X. H. Geng and Y. Zhao, *Phys. Status Solidi C*, 2010, **7**, 1128–1131.

151 J. de Wild, A. Meijerink, J. K. Rath, W. G. J. H. M. van Sark and R. E. I. Schropp, *Sol. Energy Mater. Sol. Cells*, 2010, **94**, 1919–1922.

152 J. de Wild, J. K. Rath, A. Meijerink, W. G. J. H. M. van Sark and R. E. I. Schropp, *Sol. Energy Mater. Sol. Cells*, 2010, **94**, 2395–2398.

153 Z. Q. Li, X. D. Li, Q. Q. Liu, X. H. Chen, Z. Sun, C. Liu, X. J. Ye and S. M. Huang, *Nanotechnology*, 2012, **23**, 025402.

154 S. L. Zhao, S. Q. Xu, G. H. Jia, D. G. Deng, L. H. Huang and H. P. Wang, *Mater. Lett.*, 2011, **65**, 2407–2409.

155 J. Wang, J. Wu, J. Lin, M. Huang, Y. Huang, Z. Lan, Y. Xiao, G. Yue, S. Yin and T. Sato, *ChemSusChem*, 2012, **5**, 1307–1312.

156 G. B. Shan and G. P. Demopoulos, *Adv. Mater.*, 2010, **22**, 4373–4377.

157 G. B. Shan, H. Assaaoudi and G. P. Demopoulos, *ACS Appl. Mater. Interfaces*, 2011, **3**, 3239–3243.

158 A. F. Khan, R. Yadav, P. K. Mukhopadhya, S. Singh, C. Dwivedi, V. Dutta and S. Chawla, *J. Nanopart. Res.*, 2011, **13**, 6837–6846.

159 J. H. Wu, J. L. Wang, J. M. Lin, Z. Lan, Q. W. Tang, M. L. Huang, Y. F. Huang, L. Q. Fan, Q. B. Li and Z. Y. Tang, *Adv. Energy Mater.*, 2012, **2**, 78–81.

160 M. Liu, Y. Lu, Z. B. Xie and G. M. Chow, *Sol. Energy Mater. Sol. Cells*, 2011, **95**, 800–803.

161 Q. Li, J. Lin, J. Wu, Z. Lan, Y. Wang, F. Peng and M. Huang, *Electrochim. Acta*, 2011, **56**, 4980–4984.

162 V. D. Rodriguez, J. Mendez-Ramos, V. K. Tikhomirov, J. del-Castillo, A. C. Yanes and V. V. Moshchalkov, *Opt. Mater. (Amsterdam)*, 2011, **34**, 179–182.

163 H. Q. Wang, M. Batentschuk, A. Osvet, L. Pinna and C. J. Brabec, *Adv. Mater.*, 2011, **23**, 2675–2680.

164 A. A. D. Adikaari, I. Etchart, P. H. Guering, M. Berard, S. R. P. Silva, A. K. Cheetham and R. J. Curry, *J. Appl. Phys.*, 2012, **111**, 094502.

165 B. G. Streetman and S. Banerjee, *Solid State electronic Devices*, Prentice Hall, New Jersey, 5th edn, 2000.

166 E. Bundgaard and F. C. Krebs, *Sol. Energy Mater. Sol. Cells*, 2007, **91**, 954–985.

167 D. Q. Chen, L. Lei, A. P. Yang, Z. X. Wang and Y. S. Wang, *Chem. Commun.*, 2012, **48**, 5898–5900.

168 M. Nyk, R. Kumar, T. Y. Ohulchanskyy, E. J. Bergey and P. N. Prasad, *Nano Lett.*, 2008, **8**, 3834–3838.

169 J. Zhou, Y. Sun, X. Du, L. Xiong, H. Hu and F. Li, *Biomaterials*, 2010, **31**, 3287–3295.

170 G. Chen, T. Y. Ohulchanskyy, R. Kumar, H. Agren and P. N. Prasad, *ACS Nano*, 2010, **4**, 3163–3168.

171 G. Chen, T. Y. Ohulchanskyy, W. C. Law, H. Agren and P. N. Prasad, *Nanoscale*, 2011, **3**, 2003–2008.

172 H.-T. Wong, H. L. W. Chan and J. Hao, *Opt. Express*, 2010, **18**, 6123–6130.

173 H.-T. Wong, F. Vetrone, R. Naccache, H. L. W. Chan, J. Hao and J. A. Capobianco, *J. Mater. Chem.*, 2011, **21**, 16589–16596.

174 N. N. Dong, M. Pedroni, F. Piccinelli, G. Conti, A. Sbarbati, J. E. Ramirez-Hernandez, L. M. Maestro, M. C. Iglesias-de la Cruz, F. Sanz-Rodriguez, A. Juarranz, F. Chen, F. Vetrone, J. A. Capobianco, J. G. Sole, M. Bettinelli, D. Jaque and A. Speghini, *ACS Nano*, 2011, **5**, 8665–8671.

175 J. C. Boyer, M. P. Manseau, J. I. Murray and F. C. J. M. van veggel, *Langmuir*, 2010, **26**, 1157–1164.

176 Q. Zhang, C. S. Dandeneau, X. Zhou and G. Cao, *Adv. Mater.*, 2009, **21**, 4087–4108.

177 M. Gratzel, *Acc. Chem. Res.*, 2009, **42**, 1788–1798.

178 A. Hagfeldt, G. Boschloo, L. C. Sun, L. Kloo and H. Pettersson, *Chem. Rev.*, 2010, **110**, 6595–6663.

179 F. Odobel, L. Le Pleux, Y. Pellegrin and E. Blart, *Acc. Chem. Res.*, 2010, **43**, 1063–1071.

180 J. Bisquert, *ChemPhysChem*, 2011, **12**, 1633–1636.

181 J. I. Basham, G. K. Mor and C. A. Grimes, *ACS Nano*, 2010, **4**, 1253–1258.

182 C.-Y. Chen, M. Wang, J.-Y. Li, N. Pootrakulchote, L. Alibabaei, C.-h. Ngoc-le, J.-D. Decoppet, J.-H. Tsai, C. Graetzel, C.-G. Wu, S. M. Zakeeruddin and M. Graetzel, *ACS Nano*, 2009, **3**, 3103–3109.

183 P. L. T. Boudreault, A. Najari and M. Leclerc, *Chem. Mater.*, 2011, **23**, 456–469.

Published on 16 October 2012. Downloaded on 11/09/2014 14:42:06.

184 H. Y. Chen, J. H. Hou, S. Q. Zhang, Y. Y. Liang, G. W. Yang, Y. Yang, L. P. Yu, Y. Wu and G. Li, *Nat. Photonics*, 2009, **3**, 649–653.
185 A. W. Hains, Z. Q. Liang, M. A. Woodhouse and B. A. Gregg, *Chem. Rev.*, 2010, **110**, 6689–6735.
186 J. W. Chen and Y. Cao, *Acc. Chem. Res.*, 2009, **42**, 1709–1718.
187 Z. He, C. Zhong, S. Su, M. Xu, H. Wu and Y. Cao, *Nat. Photonics*, 2012, **6**, 593–597.
188 W. Cai, X. Gong and Y. Cao, *Sol. Energy Mater. Sol. Cells*, 2010, **94**, 114–127.
189 S. H. Park, A. Roy, S. Beaupre, S. Cho, N. Coates, J. S. Moon, D. Moses, M. Leclerc, K. Lee and A. J. Heeger, *Nat. Photonics*, 2009, **3**, 297–302.
190 B. C. Thompson and J. M. J. Frechet, *Angew. Chem., Int. Ed.*, 2008, **47**, 58–77.
191 P. Kumar and S. Chand, *Prog. Photovoltaics*, 2012, **20**, 377–415.
192 H.-Q. Wang, T. Stubhan, A. Osvet, I. Litzov and C. J. Brabec, *Sol. Energy Mater. Sol. Cells*, 2012, **105**, 196–201.
193 J.-L. Wu, F.-C. Chen, S.-H. Chang, K.-S. Tan and H.-Y. Tuan, *Org. Electron.*, 2012, **13**, 2104–2108.
194 J. C. Boyer and F. C. J. M. van veggel, *Nanoscale*, 2010, **2**, 1417–1419.
195 Q. Liu, T. S. Yang, W. Feng and F. Y. Li, *J. Am. Chem. Soc.*, 2012, **134**, 5390–5397.
196 J. Z. Zhao, S. M. Ji and H. M. Guo, *RSC Adv.*, 2011, **1**, 937–950.
197 Y. Y. Cheng, B. Fuckel, R. W. MacQueen, T. Khoury, R. Clady, T. F. Schulze, N. J. Ekins-Daukes, M. J. Crossley, B. Stannowski, K. Lips and T. W. Schmidt, *Energy Environ. Sci.*, 2012, **5**, 6953–6959.
198 Y. C. Simon and C. Weder, *J. Mater. Chem.*, 2012, **22**, 20817–20830.
199 T. N. Singh-Rachford and F. N. Castellano, *Coord. Chem. Rev.*, 2010, **254**, 2560–2573.
200 T. N. Singh-Rachford, A. Nayak, M. L. Muro-Small, S. Goeb, M. J. Therien and F. N. Castellano, *J. Am. Chem. Soc.*, 2010, **132**, 14203–14211.
201 B. Fuckel, D. A. Roberts, Y. Y. Cheng, R. Clady, R. B. Piper, N. J. Ekins-Daukes, M. J. Crossley and T. W. Schmidt, *J. Phys. Chem. Lett.*, 2011, **2**, 966–971.
202 T. N. Singh-Rachford and F. N. Castellano, *J. Phys. Chem. A*, 2009, **113**, 9266–9269.
203 S. P. Feofilov, Y. Zhou, H. J. Seo, J. Y. Jeong, D. A. Keszler and R. S. Meltzer, *Phys. Rev. B: Condens. Matter*, 2006, **74**, 085101.
204 R. T. Wegh, E. V. D. van Loef and A. Meijerink, *J. Lumin.*, 2000, **90**, 111–122.
205 B. Han, H. B. Liang, Y. Huang, Y. Tao and Q. Su, *J. Phys. Chem. C*, 2010, **114**, 6770–6777.
206 D. Hou, H. Liang, M. Xie, X. Ding, J. Zhong, Q. Su, Y. Tao, Y. Huang and Z. Gao, *Opt. Express*, 2011, **19**, 11071–11083.
207 M. B. Xie, Y. Tao, Y. Huang, H. B. Liang and Q. Su, *Inorg. Chem.*, 2010, **49**, 11317–11324.
208 W. Liang and Y. Wang, *Mater. Chem. Phys.*, 2011, **127**, 170–173.
209 W. Liang and Y. H. Wang, *Mater. Chem. Phys.*, 2010, **119**, 214–217.
210 D. Wang and N. Kodama, *J. Solid State Chem.*, 2009, **182**, 2219–2224.
211 H. J. Zhang, Y. H. Wang, Y. Tao, W. H. Li, D. K. Hu, E. X. Feng and X. F. Nie, *J. Electrochem. Soc.*, 2010, **157**, J293–J296.
212 L. Zhao, Y. Wang and Y. Tao, *Electrochem. Solid-State Lett.*, 2012, **15**, B13–B16.
213 L. Beauzamy, B. Moine, R. S. Meltzer, Y. Zhou, P. Gredin, A. Jouini and K. J. Kim, *Phys. Rev. B: Condens. Matter*, 2008, **78**, 184302.
214 P. Ghosh, S. Tang and A.-V. Mudring, *J. Mater. Chem.*, 2011, **21**, 8640–8644.
215 C. Lorbeer, J. Cybinska and A. V. Mudring, *Chem. Commun.*, 2010, **46**, 571–573.
216 M. A. Gusowski, H. C. Swart, L. S. Karlsson and M. Trzebiatowska-Gusowska, *Nanoscale*, 2012, **4**, 541–546.
217 S. Hachani, B. Moine, A. El-akrmi and M. Ferid, *Opt. Mater. (Amsterdam)*, 2009, **31**, 678–684.
218 S. Hachani, B. Moine, A. El-akrmi and M. Ferid, *J. Lumin.*, 2010, **130**, 1774–1783.
219 B. Moine, S. Hachani and M. Ferid, *J. Lumin.*, 2011, **131**, 2110–2115.
220 J. Zhong, H. Liang, Q. Su, J. Zhou, Y. Huang, Z. Gao, Y. Tao and J. Wang, *Appl. Phys. B: Lasers Opt.*, 2010, **98**, 139–147.
221 B. Tian, B. Chen, Y. Tian, J. Sun, X. Li, J. Zhang, H. Zhong, L. Cheng, Z. Wu and R. Hua, *Ceram. Int.*, 2012, **38**, 3537–3540.
222 Z. R. Abrams, A. Niv and X. Zhang, *J. Appl. Phys.*, 2011, **109**, 114905.
223 P. Vergeer, T. J. H. Vlugt, M. H. F. Kox, M. I. den Hertog, J. van der Eerden and A. Meijerink, *Phys. Rev. B: Condens. Matter*, 2005, **71**, 014119.
224 Q. Y. Zhang, C. H. Yang, Z. H. Jiang and X. H. Ji, *Appl. Phys. Lett.*, 2007, **90**, 061914.
225 X. Y. Huang and Q. Y. Zhang, *J. Appl. Phys.*, 2009, **105**, 053521.
226 Q. Y. Zhang, G. F. Yang and Z. H. Jiang, *Appl. Phys. Lett.*, 2007, **91**, 051903.
227 S. Ye, B. Zhu, J. Luo, J. Chen, G. Lakshminarayana and J. Qiu, *Opt. Express*, 2008, **16**, 8989–8994.
228 W. Zheng, H. Zhu, R. Li, D. Tu, Y. Liu, W. Luo and X. Chen, *Phys. Chem. Chem. Phys.*, 2012, **14**, 6974–6980.
229 X. P. Chen, X. Y. Huang and Q. Y. Zhang, *J. Appl. Phys.*, 2009, **106**, 063518.
230 B. M. van der Ende, L. Aarts and A. Meijerink, *Adv. Mater.*, 2009, **21**, 3073–3077.
231 L. Aarts, B. M. van der Ende and A. Meijerink, *J. Appl. Phys.*, 2009, **106**, 023522.
232 J. J. Eilers, D. Biner, J. T. van Wijngaarden, K. Kraemer, H. U. Guedel and A. Meijerink, *Appl. Phys. Lett.*, 2010, **96**, 151106.
233 J.-M. Meijer, L. Aarts, B. M. van der Ende, T. J. H. Vlugt and A. Meijerink, *Phys. Rev. B: Condens. Matter*, 2010, **81**, 035107.
234 H. Lin, D. Chen, Y. Yu, A. Yang and Y. Wang, *Opt. Lett.*, 2011, **36**, 876–878.
235 D. C. Yu, X. Y. Huang, S. Ye and Q. Y. Zhang, *J. Alloys Compd.*, 2011, **509**, 9919–9923.
236 K. Deng, T. Gong, L. Hu, X. Wei, Y. Chen and M. Yin, *Opt. Express*, 2011, **19**, 1749–1754.
237 Z. Bai, M. Fujii, T. Hasegawa, K. Imakita, M. Mizuhata and S. Hayashi, *J. Phys. D: Appl. Phys.*, 2011, **44**, 455301.
238 D. C. Yu, X. Y. Huang, S. Ye, M. Y. Peng, Q. Y. Zhang and L. Wondraczek, *Appl. Phys. Lett.*, 2011, **99**, 161904.
239 D. C. Yu, X. Y. Huang, S. Ye, Q. Y. Zhang and J. Wang, *AIP Adv.*, 2011, **1**, 042161.
240 X. B. Chen, J. G. Wu, X. L. Xu, Y. Z. Zhang, N. Sawanobori, C. L. Zhang, Q. H. Pan and G. J. Salamo, *Opt. Lett.*, 2009, **34**, 887–889.
241 M. Miritello, R. Lo Savio, P. Cardile and F. Priolo, *Phys. Rev. B: Condens. Matter*, 2010, **81**, 041411.
242 D. C. Yu, S. Ye, M. Y. Peng, Q. Y. Zhang and L. Wondraczek, *Appl. Phys. Lett.*, 2012, **100**, 191911.
243 W. J. Zhang, D. C. Yu, J. P. Zhang, Q. Qian, S. H. Xu, Z. M. Yang and Q. Y. Zhang, *Opt. Mater. Express*, 2012, **2**, 636–643.
244 W. Strek, A. Bednarkiewicz and P. J. Deren, *J. Lumin.*, 2001, **92**, 229–235.
245 D. Chen, Y. Yu, Y. Wang, P. Huang and F. Weng, *J. Phys. Chem. C*, 2009, **113**, 6406–6410.
246 I. A. A. Terra, L. J. Borrero-Gonzalez, T. R. Figueredo, J. M. P. Almeida, A. C. Hernandes, L. A. O. Nunes and O. L. Malta, *J. Lumin.*, 2012, **132**, 1678–1682.
247 S. Ye, Y. Katayama and S. Tanabe, *J. Non-Cryst. Solids*, 2011, **357**, 2268–2271.
248 Q. Duan, F. Qin, D. Wang, W. Xu, J. Cheng, Z. Zhang and W. Cao, *J. Appl. Phys.*, 2011, **110**, 113503.
249 Q. Q. Duan, F. Qin, Z. G. Zhang and W. W. Cao, *Opt. Lett.*, 2012, **37**, 521–523.
250 L. C. Xie, Y. H. Wang and H. J. Zhang, *Appl. Phys. Lett.*, 2009, **94**, 061905.
251 Q. Zhang, B. Zhu, Y. Zhuang, G. Chen, X. Liu, G. Zhang, J. Qiu and D. Chen, *J. Am. Ceram. Soc.*, 2010, **93**, 654–657.
252 G. Lakshminarayana, H. Yang, S. Ye, Y. Liu and J. Qiu, *J. Phys. D: Appl. Phys.*, 2008, **41**, 175111.
253 G. Lakshminarayana and J. R. Qiu, *J. Alloys Compd.*, 2009, **481**, 582–589.
254 X. Liu, Y. Qiao, G. Dong, S. Ye, B. Zhu, G. Lakshminarayana, D. Chen and J. Qiu, *Opt. Lett.*, 2008, **33**, 2858–2860.
255 S. Ye, B. Zhu, Y. X. Zhuang, X. F. Liu, J. Luo, L. Wang and J. R. Qiu, *IOP Conf. Ser.: Mater. Sci. Eng.*, 2009, **1**, 012008.
256 H. Lin, S. M. Zhou, X. R. Hou, W. J. Li, Y. K. Li, H. Teng and T. T. Jia, *IEEE Photonics Technol. Lett.*, 2010, **22**, 866–868.
257 A. Jaffres, B. Viana and E. van der Kolk, *Chem. Phys. Lett.*, 2012, **527**, 42–46.
258 G. Lakshminarayana, H. Yang, S. Ye, Y. Liu and J. Qiu, *J. Mater. Res.*, 2008, **23**, 3090–3095.

This journal is © The Royal Society of Chemistry 2013

Published on 16 October 2012. Downloaded on 11/09/2014 14:42:06.

259 D. Chen, Y. Wang, Y. Yu, P. Huang and F. Weng, *Opt. Lett.*, 2008, **33**, 1884–1886.
260 H. Lin, X. H. Yan and X. F. Wang, *Mater. Sci. Eng., B*, 2011, **176**, 1537–1540.
261 J. J. Zhou, Y. Teng, S. Ye, G. Lin and J. R. Qiu, *Opt. Mater. (Amsterdam)*, 2012, **34**, 901–905.
262 Q. J. Chen, W. J. Zhang, X. Y. Huang, G. P. Dong, M. Y. Peng and Q. Y. Zhang, *J. Alloys Compd.*, 2012, **513**, 139–144.
263 J. T. van Wijngaarden, S. Scheidelaar, T. J. H. Vlugt, M. F. Reid and A. Meijerink, *Phys. Rev. B: Condens. Matter*, 2010, **81**, 155112.
264 L. Aarts, B. van der Ende, M. F. Reid and A. Meijerink, *Spectrosc. Lett.*, 2010, **43**, 373–381.
265 K. Deng, X. Wei, X. Wang, Y. Chen and M. Yin, *Appl. Phys. B: Lasers Opt.*, 2011, **102**, 555–558.
266 Y. Xu, X. Zhang, S. Dai, B. Fan, H. Ma, J.-l. Adam, J. Ren and G. Chen, *J. Phys. Chem. C*, 2011, **115**, 13056–13062.
267 D. Serrano, A. Braud, J. L. Doualan, P. Camy, A. Benayad, V. Menard and R. Moncorge, *Opt. Mater.*, 2011, **33**, 1028–1031.
268 D. Serrano, A. Braud, J.-L. Doualan, P. Camy and R. Moncorge, *J. Opt. Soc. Am. B*, 2011, **28**, 1760–1765.
269 G. M. Yang, S. M. Zhou, H. Lin and H. Teng, *Physica B (Amsterdam)*, 2011, **406**, 3588–3591.
270 H. Wen and P. A. Tanner, *Opt. Mater.*, 2011, **33**, 1602–1606.
271 Y. Katayama and S. Tanabe, *Opt. Mater.*, 2010, **33**, 176–179.
272 Y. Katayama and S. Tanabe, *Materials*, 2010, **3**, 2405–2411.
273 A. Guille, A. Pereira, C. Martinet and B. Moine, *Opt. Lett.*, 2012, **37**, 2280–2282.
274 L. Aarts, S. Jaeqx, B. M. van der Ende and A. Meijerink, *J. Lumin.*, 2011, **131**, 608–613.
275 S. Xiao, X. Yang and J. W. Ding, *Appl. Phys. B: Lasers Opt.*, 2010, **99**, 769–773.
276 D. Chen, Y. Yu, H. Lin, P. Huang, Z. Shan and Y. Wang, *Opt. Lett.*, 2010, **35**, 220–222.
277 X. P. Chen, W. J. Zhang and Q. Y. Zhang, *Physica B (Amsterdam)*, 2011, **406**, 1248–1252.
278 D. C. Yu, X. Y. Huang, S. Ye, M. Y. Peng and Q. Y. Zhang, *Sol. Energy Mater. Sol. Cells*, 2012, **101**, 303–307.
279 D. Chen, Y. Wang, Y. Yu, P. Huang and F. Weng, *J. Appl. Phys.*, 2008, **104**, 116105.
280 J. Chen, H. Guo, Z. Li, H. Zhang and Y. Zhuang, *Opt. Mater.*, 2010, **32**, 998–1001.
281 J. Chen, H. Zhang, F. Li and H. Guo, *Mater. Chem. Phys.*, 2011, **128**, 191–194.
282 X. Liu, Y. Teng, Y. Zhuang, J. Xie, Y. Qiao, G. Dong, D. Chen and J. Qiu, *Opt. Lett.*, 2009, **34**, 3565–3567.
283 H. Lin, S. M. Zhou, H. Teng, Y. K. Li, W. J. Li, X. R. Hou and T. T. Jia, *J. Appl. Phys.*, 2010, **107**, 043107.
284 N. Rakov and G. S. Maciel, *J. Appl. Phys.*, 2011, **110**, 083519.
285 X. Y. Huang, D. C. Yu and Q. Y. Zhang, *J. Appl. Phys.*, 2009, **106**, 113521.
286 Q. Zhang, J. Wang, G. Zhang and Q. Su, *J. Mater. Chem.*, 2009, **19**, 7088–7092.
287 J. Zhou, Y. Teng, S. Ye, Y. Zhuang and J. Qiu, *Chem. Phys. Lett.*, 2010, **486**, 116–118.
288 J. Zhou, Y. Zhuang, S. Ye, Y. Teng, G. Lin, B. Zhu, J. Xie and J. Qiu, *Appl. Phys. Lett.*, 2009, **95**, 141101.
289 J. Zhou, Y. Teng, G. Lin, X. Xu, Z. Ma and J. Qiu, *J. Electrochem. Soc.*, 2010, **157**, B1146–B1148.
290 Y. Teng, J. Zhou, S. Ye and J. Qiu, *J. Electrochem. Soc.*, 2010, **157**, A1073–A1075.
291 H. Lin, D. Chen, Y. Yu, Z. Shan, P. Huang, A. Yang and Y. Wang, *J. Alloys Compd.*, 2011, **509**, 3363–3366.
292 M. M. Smedskjaer, J. Qiu, J. Wang and Y. Yue, *Appl. Phys. Lett.*, 2011, **98**, 071911.
293 Y. Teng, J. Zhou, X. Liu, S. Ye and J. Qiu, *Opt. Express*, 2010, **18**, 9671–9676.
294 X. Y. Huang and Q. Y. Zhang, *J. Appl. Phys.*, 2010, **107**, 063505.
295 X. Y. Huang, X. H. Ji and Q. Y. Zhang, *J. Am. Ceram. Soc.*, 2011, **94**, 833–837.
296 M. Qu, R. Wang, Y. Chen, Y. Zhang, K. Li and H. Yan, *J. Lumin.*, 2012, **132**, 1285–1289.
297 X. Y. Huang, J. X. Wang, D. C. Yu, S. Ye, Q. Y. Zhang and X. W. Sun, *J. Appl. Phys.*, 2011, **109**, 113526.
298 R. Zhou, Y. Kou, X. Wei, C. Duan, Y. Chen and M. Yin, *Appl. Phys. B*, 2012, **107**, 483–487.
299 X. Wei, S. Huang, Y. Chen, C. Guo, M. Yin and W. Xu, *J. Appl. Phys.*, 2010, **107**, 103107.
300 Y. Peng, J. Liu, K. Zhang, H. Luo, J. Li, B. Xu, L. Han, X. Li and X. Yu, *Appl. Phys. Lett.*, 2011, **99**, 121110.
301 X. Cheng, L. Su, Y. Wang, X. Zhu, X. Wei and Y. Wang, *Opt. Mater.*, 2012, **34**, 1102–1106.
302 M. V. Shestakov, V. K. Tikhomirov, D. Kirilenko, A. S. Kuznetsov, L. F. Chibotaru, A. N. Baranov, G. Van Tendeloo and V. V. Moshchalkov, *Opt. Express*, 2011, **19**, 15955–15964.
303 J. Zhou, Y. Teng, G. Lin and J. Qiu, *J. Non-Cryst. Solids*, 2011, **357**, 2336–2339.
304 W. Zhou, J. Yang, J. Wang, Y. Li, X. Kuang, J. Tang and H. Liang, *Opt. Express*, 2012, **20**, A510–A518.
305 J. Ueda and S. Tanabe, *J. Appl. Phys.*, 2009, **106**, 043101.
306 H. Zhang, X. Liu, F. Zhao, L. Zhang, Y. Zhang and H. Guo, *Opt. Mater.*, 2012, **34**, 1034–1036.
307 E. van der Kolk, O. M. Ten Kate, J. W. Wiegman, D. Biner and K. W. Kramer, *Opt. Mater.*, 2011, **33**, 1024–1027.
308 A. Guille, A. Pereira, G. Breton, A. Bensalah-Ledoux and B. Moine, *J. Appl. Phys.*, 2012, **111**, 043104.
309 R. J. Xie, N. Hirosaki, M. Mitomo, K. Uheda, T. Suehiro, X. Xu, Y. Yamamoto and T. Sekiguchi, *J. Phys. Chem. B*, 2005, **109**, 9490–9494.
310 G. Blasse and A. Bril, *J. Chem. Phys.*, 1968, **48**, 217–222.
311 S. Yan, J. Zhang, X. Zhang, S. Lu, X. Ren, Z. Nie and X. Wang, *J. Phys. Chem. C*, 2007, **111**, 13256–13260.
312 M. H. Qu, R. Z. Wang, Y. Zhang, K. Y. Li and H. Yan, *J. Appl. Phys.*, 2012, **111**, 093108.
313 H. Guo, N. Dong, M. Yin, W. P. Zhang, L. R. Lou and S. D. Xia, *J. Phys. Chem. B*, 2004, **108**, 19205–19209.
314 Y. Lu and X. Chen, *Appl. Phys. Lett.*, 2009, **94**, 193110.
315 G. Chen, H. Liu, H. Liang, G. Somesfalean and Z. Zhang, *J. Phys. Chem. C*, 2008, **112**, 12030–12036.
316 J. Zhou, Y. Teng, X. Liu, S. Ye, Z. Ma and J. Qiu, *Phys. Chem. Chem. Phys.*, 2010, **12**, 13759–13762.
317 J. Zhou, Y. Teng, X. Liu, S. Ye, X. Xu, Z. Ma and J. Qiu, *Opt. Express*, 2010, **18**, 21663–21668.
318 V. D. Rodriguez, V. K. Tikhomirov, J. Mendez-Ramos, A. C. Yanes and V. V. Moshchalkov, *Sol. Energy Mater. Sol. Cells*, 2010, **94**, 1612–1617.
319 S. Xu, W. Xu, B. A. Dong, X. Bai and H. W. Song, *J. Appl. Phys.*, 2011, **110**, 113113.
320 A. J. Nozik, *Nat. Nanotechnol.*, 2009, **4**, 548–549.
321 M. C. Beard, K. P. Knutsen, P. Yu, J. M. Luther, Q. Song, W. K. Metzger, R. J. Ellingson and A. J. Nozik, *Nano Lett.*, 2007, **7**, 2506–2512.
322 R. D. Schaller, V. M. Agranovich and V. I. Klimov, *Nat. Phys.*, 2005, **1**, 189–194.
323 W.-L. Chan, M. Ligges, A. Jailaubekov, L. Kaake, L. Miaja-Avila and X.-Y. Zhu, *Science*, 2011, **334**, 1541–1545.
324 M. C. Beard, A. G. Midgett, M. C. Hanna, J. M. Luther, B. K. Hughes and A. J. Nozik, *Nano Lett.*, 2010, **10**, 3019–3027.
325 R. D. Schaller and V. I. Klimov, *Phys. Rev. Lett.*, 2004, **92**, 186601.
326 V. Sukhovatkin, S. Hinds, L. Brzozowski and E. H. Sargent, *Science*, 2009, **324**, 1542–1544.
327 N. M. Gabor, Z. Zhong, K. Bosnick, J. Park and P. L. McEuen, *Science*, 2009, **325**, 1367–1371.
328 S. Konabe and S. Okada, *Phys. Rev. Lett.*, 2012, **108**, 227401.
329 J. A. McGuire, J. Joo, J. M. Pietryga, R. D. Schaller and V. I. Klimov, *Acc. Chem. Res.*, 2008, **41**, 1810–1819.
330 D. J. Binks, *Phys. Chem. Chem. Phys.*, 2011, **13**, 12693–12704.
331 M. C. Beard, *J. Phys. Chem. Lett.*, 2011, **2**, 1282–1288.
332 A. J. Nozik, M. C. Beard, J. M. Luther, M. Law, R. J. Ellingson and J. C. Johnson, *Chem. Rev.*, 2010, **110**, 6873–6890.
333 G. Konstantatos and E. H. Sargent, *Nat. Nanotechnol.*, 2010, **5**, 391–400.
334 G. Nair, L.-Y. Chang, S. M. Geyer and M. G. Bawendi, *Nano Lett.*, 2011, **11**, 2145–2151.
335 M. T. Trinh, R. Limpens, W. D. A. M. de Boer, J. M. Schins, L. D. A. Siebbeles and T. Gregorkiewicz, *Nat. Photonics*, 2012, **6**, 316–321.

Published on 16 October 2012. Downloaded on 11/09/2014 14:42:06.

336 O. E. Semonin, J. M. Luther, S. Choi, H. Y. Chen, J. B. Gao, A. J. Nozik and M. C. Beard, *Science*, 2011, **334**, 1530–1533.
337 N. Yamada, L. N. Anh and T. Kambayashi, *Sol. Energy Mater. Sol. Cells*, 2010, **94**, 413–419.
338 M. J. Currie, J. K. Mapel, T. D. Heidel, S. Goffri and M. A. Baldo, *Science*, 2008, **321**, 226–228.
339 R. Reisfeld, *Opt. Mater. (Amsterdam)*, 2010, **32**, 850–856.
340 M. G. Debije and P. P. C. Verbunt, *Adv. Energy Mater.*, 2012, **2**, 12–35.
341 D. K. G. de Boer, D. J. Broer, M. G. Debije, W. Keur, A. Meijerink, C. R. Ronda and P. P. C. Verbunt, *Opt. Express*, 2012, **20**, A395–A405.
342 E. Klampaftis, D. Ross, K. R. McIntosh and B. S. Richards, *Sol. Energy Mater. Sol. Cells*, 2009, **93**, 1182–1194.
343 B. C. Rowan, L. R. Wilson and B. S. Richards, *IEEE J. Sel. Top. Quantum Electron.*, 2008, **14**, 1312–1322.
344 P. Chung, H. H. Chung and P. H. Holloway, *J. Vac. Sci. Technol., A*, 2007, **25**, 61–66.
345 M. Mendez, Y. Cesteros, L. F. Marsal, E. Martinez-Ferrero, P. Salagre, P. Formentin, J. Pallares, M. Aguilo, F. Diaz and J. J. Carvajal, *Opt. Mater.*, 2011, **33**, 1120–1123.
346 S. Takeshita, K. Nakayama, T. Isobe, T. Sawayama and S. Niikura, *J. Electrochem. Soc.*, 2009, **156**, J273–J277.
347 L. M. Shao and X. P. Jing, *J. Lumin.*, 2011, **131**, 1216–1221.
348 L. M. Shao, J. Q. Zhao, Z. G. Xia and X. P. Jing, *J. Electrochem. Soc.*, 2011, **158**, J300–J304.
349 J. X. Meng, J. Q. Li, Z. P. Shi and K. W. Cheah, *Appl. Phys. Lett.*, 2008, **93**, 221908.
350 J. Zhou, Y. Teng, X. Liu, Z. Ma and J. Qiu, *J. Mater. Res.*, 2011, **26**, 689–692.
351 H. Fu, S. Cui, Q. Luo, X. Qiao, X. Fan and X. Zhang, *J. Non-Cryst. Solids*, 2012, **358**, 1217–1220.
352 S. Ye, N. Jiang, F. He, X. Liu, B. Zhu, Y. Teng and J. R. Qiu, *Opt. Express*, 2010, **18**, 639–644.
353 S. Ye, N. Jiang, J. Zhou, D. Wang and J. Qiu, *J. Electrochem. Soc.*, 2012, **159**, H11–H15.
354 Q. Luo, X. S. Qiao, X. P. Fan and X. H. Zhang, *Opt. Lett.*, 2011, **36**, 2767–2769.
355 S. Ye, D. C. Yu, X. Y. Huang, Z. M. Yang and Q. Y. Zhang, *J. Appl. Phys.*, 2010, **108**, 083528.
356 G. G. Zhang, C. M. Liu, J. Wang, X. J. Kuang and Q. Su, *Opt. Express*, 2011, **19**, 24314–24319.
357 O. M. ten Kate, H. T. Hintzen, P. Dorenbos and E. van der Kolk, *J. Mater. Chem.*, 2011, **21**, 18289–18294.
358 V. K. Tikhomirov, T. Vosch, E. Fron, V. D. Rodriguez, J. J. Velazquez, D. Kirilenko, G. van Tendeloo, J. Hofkens, M. van der Auweraer and V. V. Moshchalkov, *RSC Adv.*, 2012, **2**, 1496–1501.
359 S. Ye, B. Zhu, J. Luo, Y. Teng, J. Chen, G. Lakshminarayana, G. Qian and J. Qiu, *Appl. Phys. Lett.*, 2008, **93**, 181110.
360 S. Ye, B. Zhu, Y. Liu, Y. Teng, G. Lin, G. Lakshminarayana, X. P. Fan and J. R. Qiu, *J. Appl. Phys.*, 2009, **105**, 063508.
361 A. Santana-Alonso, A. C. Yanes, J. Mendez-Ramos, J. del-Castillo and V. D. Rodriguez, *Opt. Mater.*, 2011, **33**, 587–591.
362 S. Gomez, I. Urra, R. Valiente and F. Rodriguez, *Sol. Energy Mater. Sol. Cells*, 2011, **95**, 2018–2022.
363 M. Sendova-Vassileva, *J. Mater. Sci.*, 2011, **46**, 7184–7190.
364 J. F. Liu, Q. H. Yao and Y. D. Li, *Appl. Phys. Lett.*, 2006, **88**, 173119.
365 J. H. Wu, G. X. Xie, J. M. Lin, Z. Lan, M. L. Huang and Y. F. Huang, *J. Power Sources*, 2010, **195**, 6937–6940.
366 H. Hafez, M. Saif and M. S. A. Abdel-Mottaleb, *J. Power Sources*, 2011, **196**, 5792–5796.
367 H. Hafez, J. H. Wu, Z. Lan, Q. H. Li, G. X. Xie, J. M. Lin, M. L. Huang, Y. F. Huang and M. S. Abdel-Mottaleb, *Nanotechnology*, 2010, **21**, 415201.
368 D. L. Gao, H. R. Zheng, X. Y. Zhang, Z. X. Fu, Z. L. Zhang, Y. Tian and M. Cui, *Appl. Phys. Lett.*, 2011, **98**, 011907.
369 W. Xu, H. W. Song, D. T. Yan, H. C. Zhu, Y. Wang, S. Xu, X. Bai, B. A. Dong and Y. X. Liu, *J. Mater. Chem.*, 2011, **21**, 12331–12336.
370 M. Y. Peng and L. Wondraczek, *J. Mater. Chem.*, 2009, **19**, 627–630.
371 D. K. G. de Boer, D. J. Broer, M. G. Debije, W. Keur, A. Meijerink, C. R. Ronda and P. P. C. Verbunt, *Opt. Express*, 2012, **20**, A395–A405.
372 G. A. Hebbink, J. W. Stouwdam, D. N. Reinhoudt and F. C. J. M. van Veggel, *Adv. Mater.*, 2002, **14**, 1147–1150.
373 J. W. Stouwdam and F. C. J. M. van Veggel, *Nano Lett.*, 2002, **2**, 733–737.
374 L. N. Sun, H. J. Zhang, Q. G. Meng, F. Y. Liu, L. S. Fu, C. Y. Peng, J. B. Yu, G. L. Zheng and S. B. Wang, *J. Phys. Chem. B*, 2005, **109**, 6174–6182.
375 M. F. Zhang, S. G. Shi, J. X. Meng, X. Q. Wang, H. Fan, Y. C. Zhu, X. Y. Wang and Y. T. Qian, *J. Phys. Chem. C*, 2008, **112**, 2825–2830.
376 H. J. Zhang, Y. H. Wang and L. L. Han, *J. Appl. Phys.*, 2011, **109**, 053109.
377 D. B. He, C. L. Yu, J. M. Cheng, S. G. Li and L. L. Hu, *Solid State Commun.*, 2010, **150**, 2354–2356.
378 T. Fix, H. Rinnert, M. G. Blamire, A. Slaoui and J. L. MacManus-Driscoll, *Sol. Energy Mater. Sol. Cells*, 2012, **102**, 71–74.
379 L. N. Sun, W. P. Mai, S. Dang, Y. N. Qiu, W. Deng, L. Y. Shi, W. Yan and H. J. Zhang, *J. Mater. Chem.*, 2012, **22**, 5121–5127.
380 G. X. Liu, R. Zhang, Q. L. Xiao, S. Y. Zou, W. F. Peng, L. W. Cao and J. X. Meng, *Opt. Mater.*, 2011, **34**, 313–316.
381 Y. S. Liu, W. Q. Luo, R. F. Li and X. Y. Chen, *J. Nanosci. Nanotechnol.*, 2010, **10**, 1871–1876.
382 J. W. Stouwdam and F. C. J. M. van Veggel, *ChemPhysChem*, 2004, **5**, 743–746.
383 W. Q. Luo, R. F. Li and X. Y. Chen, *J. Phys. Chem. C*, 2009, **113**, 8772–8777.
384 Z. S. Wang, Y. Cui, K. Hara, Y. Dan-Oh, C. Kasada and A. Shinpo, *Adv. Mater.*, 2007, **19**, 1138–1141.
385 A. Kay and M. Gratzel, *Chem. Mater.*, 2002, **14**, 2930–2935.
386 W. G. J. H. M. van Sark, K. W. J. Barnham, L. H. Slooff, A. J. Chatten, A. Buchtemann, A. Meyer, S. J. McCormack, R. Koole, D. J. Farrell, R. Bose, E. E. Bende, A. R. Burgers, T. Budel, J. Quilitz, M. Kennedy, T. Meyer, C. D. M. Donega, A. Meijerink and D. Vanmaekelbergh, *Opt. Express*, 2008, **16**, 21773–21792.
387 W. van Sark, *Appl. Phys. Lett.*, 2005, **87**, 151117.
388 W. van Sark, A. Meijerink, R. E. I. Schropp, J. A. M. van Roosmalen and E. H. Lysen, *Semiconductors*, 2004, **38**, 962–969.
389 W. van Sark, A. Meijerink, R. E. I. Schropp, J. A. M. van Roosmalen and E. H. Lysen, *Sol. Energy Mater. Sol. Cells*, 2005, **87**, 395–409.
390 W. G. J. H. M. van Sark, *Thin Solid Films*, 2008, **516**, 6808–6812.
391 J. Bomm, A. Buechtemann, A. J. Chatten, R. Bose, D. J. Farrell, N. L. A. Chan, Y. Xiao, L. H. Slooff, T. Meyer, A. Meyer, W. G. J. H. M. van Sark and R. Koole, *Sol. Energy Mater. Sol. Cells*, 2011, **95**, 2087–2094.
392 A. J. Chatten, K. W. J. Barnham, B. F. Buxton, N. J. Ekins-Daukes and M. A. Malik, *Sol. Energy Mater. Sol. Cells*, 2003, **75**, 363–371.
393 A. J. Chatten, K. W. J. Barnham, B. F. Buxton, N. J. Ekins-Daukes and M. A. Malik, *Semiconductors*, 2004, **38**, 909–917.
394 A. Schueler, M. Python, M. V. del Olmo and E. de Chambrier, *Sol. Energy*, 2007, **81**, 1159–1165.
395 S. J. Gallagher, B. C. Rowan, J. Doran and B. Norton, *Sol. Energy*, 2007, **81**, 540–547.
396 S. M. Reda, *Acta Mater.*, 2008, **56**, 259–264.
397 M. G. Hyldahl, S. T. Bailey and B. P. Wittmershaus, *Sol. Energy*, 2009, **83**, 566–573.
398 Z. Cheng, F. Su, L. Pan, M. Cao and Z. Sun, *J. Alloys Compd.*, 2010, **494**, L7–L10.
399 D. Sahin, B. Ilan and D. F. Kelley, *J. Appl. Phys.*, 2011, **110**, 033108.
400 M. Kennedy, S. J. McCormack, J. Doran and B. Norton, *Sol. Energy*, 2009, **83**, 978–981.
401 F. Purcell-Milton and Y. K. Gun'ko, *J. Mater. Chem.*, 2012, **22**, 16687–16697.
402 G. V. Shcherbatyuk, R. H. Inman, C. Wang, R. Winston and S. Ghosh, *Appl. Phys. Lett.*, 2010, **96**, 191901.
403 S. Chandra, J. Doran, S. J. McCormack, M. Kennedy and A. J. Chatten, *Sol. Energy Mater. Sol. Cells*, 2012, **98**, 385–390.
404 Y. Du, B. Xu, T. Fu, M. Cai, F. Li, Y. Zhang and Q. Wang, *J. Am. Chem. Soc.*, 2010, **132**, 1470–1471.
405 G. I. Koleilat, L. Levina, H. Shukla, S. H. Myrskog, S. Hinds, A. G. Pattantyus-Abraham and E. H. Sargent, *ACS Nano*, 2008, **2**, 833–840.
406 R. G. Xie, X. H. Zhong and T. Basche, *Adv. Mater.*, 2005, **17**, 2741–2745.
407 S. Kim, B. Fisher, H. J. Eisler and M. Bawendi, *J. Am. Chem. Soc.*, 2003, **125**, 11466–11467.
408 S. Kim, Y. T. Lim, E. G. Soltesz, A. M. De Grand, J. Lee, A. Nakayama, J. A. Parker, T. Mihaljevic, R. G. Laurence,

This journal is © The Royal Society of Chemistry 2013

View Article Online

Published on 16 October 2012. Downloaded on 11/09/2014 14:42:06.

D. M. Dor, L. H. Cohn, M. G. Bawendi and J. V. Frangioni, *Nat. Biotechnol.*, 2004, **22**, 93–97.

409 W. Wu, T. Wang, X. Wang, S. Wu, Y. Luo, X. Tian and Q. Zhang, *Sol. Energy*, 2010, **84**, 2140–2145.

410 T. Wang, J. Zhang, W. Ma, Y. Luo, L. Wang, Z. Hu, W. Wu, X. Wang, G. Zou and Q. Zhang, *Sol. Energy*, 2011, **85**, 2571–2579.

411 J. Graffion, X. Cattoen, M. W. C. Man, V. R. Fernandes, P. S. Andre, R. A. S. Ferreira and L. D. Carlos, *Chem. Mater.*, 2011, **23**, 4773–4782.

412 A. Le Donne, M. Acciarri, D. Narducci, S. Marchionna and S. Binetti, *Prog. Photovoltaics*, 2009, **17**, 519–525.

413 O. Moudam, B. C. Rowan, M. Alamiry, P. Richardson, B. S. Richards, A. C. Jones and N. Robertson, *Chem. Commun.*, 2009, 6649–6651.

414 S. Marchionna, F. Meinardi, A. Acciarri, S. Binetti, A. Papagni, S. Pizzini, V. Malatesta and R. Tubino, *J. Lumin.*, 2006, **118**, 325–329.

415 G. Katsagounos, E. Stathatos, N. B. Arabatzis, A. D. Keramidas and P. Lianos, *J. Lumin.*, 2011, **131**, 1776–1781.

416 T. Fukuda, S. Kato, E. Kin, K. Okaniwa, H. Morikawa, Z. Honda and N. Kamata, *Opt. Mater.*, 2009, **32**, 22–25.

417 T. Fukuda, S. Yamauchi, Z. Honda, N. Kijima and N. Kamata, *Opt. Mater.*, 2009, **32**, 207–211.

418 K. Machida, H. Li, D. Ueda, S. Inoue and G. Adachi, *J. Lumin.*, 2000, **87–9**, 1257–1259.

419 J. H. Oh, H. M. Song, Y. K. Eom, J. H. Ryu, M. J. Ju and H. K. Kim, *Bull. Korean Chem. Soc.*, 2011, **32**, 2743–2750.

420 J. Liu, K. Wang, W. Zheng, W. Huang, C.-H. Li and X.-Z. You, *Prog. Photovoltaics*, 2012, DOI: 10.1002/pip.1251.

421 T. Jin, S. Inoue, K. Machida and G. Adachi, *J. Electrochem. Soc.*, 1997, **144**, 4054–4058.

422 T. Jin, S. Inoue, S. Tsutsumi, K. Machida and G. Adachi, *Chem. Lett.*, 1997, 171–172.

423 L.-N. Sun, J.-B. Yu, H.-J. Zhang, Q.-G. Meng, E. Ma, C.-Y. Peng and K.-Y. Yang, *Microporous Mesoporous Mater.*, 2007, **98**, 156–165.

424 K. A. White, D. A. Chengelis, K. A. Gogick, J. Stehman, N. L. Rosi and S. Petoud, *J. Am. Chem. Soc.*, 2009, **131**, 18069–18071.

425 J. Zhang, P. D. Badger, S. J. Geib and S. Petoud, *Angew. Chem., Int. Ed.*, 2005, **44**, 2508–2512.

426 A. Sanguineti, A. Monguzzi, G. Vaccaro, F. Meinardi, E. Ronchi, M. Moret, U. Cosentino, G. Moro, R. Simonutti, M. Mauri, R. Tubino and L. Beverina, *Phys. Chem. Chem. Phys.*, 2012, **14**, 6452–6455.

427 W. Zhang, F. Ding and S. Y. Chou, *Adv. Mater.*, 2012, **24**, OP236–OP241.

428 C. M. Johnson, P. J. Reece and G. J. Conibeer, *Opt. Lett.*, 2011, **36**, 3990–3992.

429 J. F. Suyver, A. Aebischer, D. Biner, P. Gerner, J. Grimm, S. Heer, K. W. Kramer, C. Reinhard and H. U. Gudel, *Opt. Mater.*, 2005, **27**, 1111–1130.

430 A. C. Pan, C. del Canizo, E. Canovas, N. M. Santos, J. P. Leitao and A. Luque, *Sol. Energy Mater. Sol. Cells*, 2010, **94**, 1923–1926.

431 W. Zou, C. Visser, J. A. Maduro, M. S. Pshenichnikov and J. C. Hummelen, *Nat. Photonics*, 2012, **6**, 560–564.

432 B. Fan, C. Chlique, O. Merdrignac-Conanec, X. Zhang and X. Fan, *J. Phys. Chem. C*, 2012, **116**, 11652–11657.

433 J. W. E. Wiegman and E. van der Kolk, *Sol. Energy Mater. Sol. Cells*, 2012, **103**, 41–47.

434 Y. F. Xiao, C. L. Zou, Y. W. Hu, Y. Li, L. X. Xiao, F. W. Sun and Q. H. Gong, *IEEE J. Quantum Electron.*, 2011, **47**, 1171–1176.

435 H. Hernandez-Noyola, D. H. Potterveld, R. J. Holt and S. B. Darling, *Energy Environ. Sci.*, 2012, **5**, 5798–5802.